

**DESIGNED-IN MOLECULAR INTERACTIONS AND CROSS-LINKING  
INTERFACE FOR SUPERIOR NANOCOMPOSITES:  
A MULTI-SCALE INSIGHT**

**by**

**ELİF ÖZDEN YENİGÜN**

**Submitted to the Graduate School of Engineering and Natural Sciences  
in partial fulfillment of  
the requirements for the degree of  
Doctor of Philosophy**

**Sabancı University  
Spring 2013**

DESIGNED-IN MOLECULAR INTERACTIONS AND CROSS-LINKING

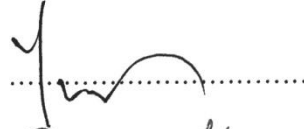
INTERFACE FOR SUPERIOR NANOCOMPOSITES: A MULTI-SCALE INSIGHT

APPROVED BY

Assoc. Prof Dr Melih Papila  
(Thesis advisor)



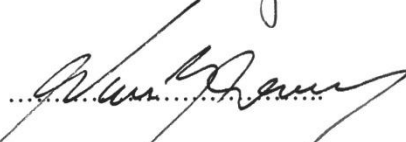
Prof Dr Yusuf Z. Menceloğlu



Prof Dr Canan Atılgan



Assoc. Prof Dr Nuri Ersoy



Prof Dr Ali Rana Atılgan



DATE OF APPROVAL: ...03/06/2013.....

© Elif Özden Yenigün 2013

All Rights Reserved

DESIGNED-IN MOLECULAR INTERACTIONS AND CROSS-LINKING  
INTERFACE FOR SUPERIOR NANOCOMPOSITES: A MULTI-SCALE INSIGHT

Elif ÖZDEN YENİGÜN

MAT, Doctor of Philosophy Thesis, 2013

Thesis Advisor: Assoc. Prof Melih Papila

Keywords: Electro-spinning, Nanofiber, Carbon Nanotubes, Epoxy Composite,  
Molecular Dynamics, Dissipative Particle Dynamics

**Abstract**

A defining feature of polymer nanocomposites is the nano-scale of fillers leading to dramatic increase in interfacial area and associated sensitivity of properties to the filler-matrix interface. Stronger/attractive interfacial region helps to prevent early failure and facilitates enhanced mechanical behavior of nanocomposites. This thesis is an effort to address how interface characteristic can impact dominated physical mechanisms and under which circumstances improve particularly mechanical and thermo-mechanical properties of nanofiber reinforced nanocomposite.

The hypothesis is that incorporation of electrospun surface modified/reactive polystyrene-co-glycidyl methacrylate P(St-co-GMA) nanofibers with epoxide functional groups into the epoxy resin results in significant improvements in the mechanical properties. Several mechanical and thermo-mechanical tests demonstrate significant increase in the mechanical response. Given the choices of the fiber material

under consideration, the enhancement is attributed to the combined effect of the two factors: the inherent cross-linked fiber structure and the surface chemistry of the electrospun fibers leading to cross-linked polymer matrix-nanofiber interfacial bonding. Multi walled carbon nanotubes (MWCNTs) can also be embedded into entangled nanofiber network during the electro-spinning process to improve composite strength, durability, and impact resistance. The enhancement by the nano-scale fibrous reinforcement with designed interface can be further propagated into structural composites. It was shown that structural integrity of the electrospun P(St-co-GMA) based nanofibers with/without MWCNTs as interlayers in conventional carbon fiber/epoxy prepreg result in increased resistance to transverse matrix cracking and delamination at macro scale without weight penalty.

Consecutively, this thesis traces the effect of the nanofiller chemistry and cross-linking on mechanical behavior of thermoset polymer matrix nanocomposites via numerical simulations. Multi-scale simulations including molecular dynamics and dissipative particle dynamics are employed to address the reinforcing function in nanocomposites at nanoscale. Coupled with focused experimental study on the interface, our novel modeling efforts are helping to elucidate the physical mechanisms that underlie nanocomposite bulk performance and ultimately enable efficient design of nanocomposites.

Overall, the idea of chemistry specific design of interface in nanofibrous matrix composites is significantly effective. The experimental results show that the given the knowledge of the matrix system, smart choice of fiber polymer provides stronger interfacial bonding and improved mechanical properties. Simulation tools, on the other hand can trace the signatures of these improvements, and promise an efficient assessment methodology for interface design which can be help to optimize also the experimental efforts.

MOLEKÜLER ETKİLEŞİMLERİN VE ÇAPRAZ BAĞLANMIŞ ARAYÜZÜN  
ÜSTÜN NANOKOMPOZİT MALZEMELER İÇİN TASARIMI:  
BİR ÇOK-BOYUTLU ANLAYIŞ

Elif ÖZDEN YENİGÜN

MAT, Doktora Tezi, 2013

Tez Danışmanı: Doç. Dr. Melih Papıla

Anahtar Kelimeler: Elektro-üretim, Nanolifler, Karbon Nanotüpler , Epoksi  
Kompozitler, Moleküler Dinamik, Dağınık Partikül Dinamiği

**Özet**

Nanoparçacık takviyeli polimer kompozit malzemeler, geleneksel kompozit malzemelere kıyasla olağanüstü performans artışları gösterebilmektedir. Polimer kompozit malzemelerde dikkat edilmesi gereken hususların başında, nano boyutta olan takviye elemanlarının oluşturduğu ve kompozitin genel özelliklerini de belirleyen, geniş arayüz alanları gelir. Kuvvetli bir arayüz oluşumu kompozitin mekanik performansını arttırmasının yanı sıra olası erken hasar mekanizmalarını da engeller. Bu tez kapsamında özellikle arayüz karakteristiğinin kompozit malzemelerde etkin kuvvetlendirme mekanizmalarını nasıl etkilediği ve hangi koşulların mekanik ve termomekanik özelliklerde artışa sebep olduğu sistematik olarak incelenmiştir.

Bu çalışmada, öncelikle yüzeyi modifiye edilmiş ve epoksi reçine ile etkileşime girebilen reaktif polistiren-ko-glisidilmetakrilat (PSt-ko-GMA) nanoliflerin epoksi reçinede takviye elemanı olarak kullanılması araştırılmıştır. Buradaki hipotezimiz,

arayüzde polimer matris ile kimyasal bağ yapabilen nanoliflerin oluşturacağı kuvvetli arayüzün, kompozit malzemenin mekanik ve termo-mekanik özelliklerini önemli ölçüde iyileştirecek olmasıdır. Elde ettiğimiz mekanik ve termo-mekanik test sonuçları göstermektedir ki mekanik artışa sebep olan temel iki faktör bulunmaktadır: çapraz bağlanabilen nanolif yapısı ve nanolifin yüzey polimer matris ile etkileşime girebilen yüzey kimyası. Bu çalışmanın devamında, çoklu duvarlı karbon nanotüpler, rasgele dağılmış nanolif ağına yine elektro-üretim tekniğiyle kompozitin mukavemetini arttırmak için entegre edilmiş ve yine epoksi reçinenin kuvvetlendirilmesi amaçlanmıştır. Ek olarak, P(St-*ko*-GMA) /karbon nanotüp içeren ve içermeyen nanoliflerden oluşan dokumasız yüzey ara faz olarak geleneksel karbon lif/ epoksi reçine prepreglerinde delaminasyon direncini ve yanal matris çatlamasını geciktirmek için kullanılmıştır.

Bu tez çalışması, deneysel yöntemlerin yanısıra, nanolif kimyası ve çapraz bağlanma mekanizmasının termoset polimer kompozitlerde mekanik davranış üzerindeki etkisini hesaplamalı yöntemlerle araştırılmasını da içermektedir. Moleküler dinamik ve dağılık partikül dinamiği metodlarını da içeren çok-boyutlu modelleme yöntemi kullanılarak nano düzeyde baskın olan kuvvetlendirme mekanizmaları araştırılmıştır. Arayüzde deneysel olarak gözlemlediğimiz sonuçlarımızın ışığında, çok boyutlu modelleme esaslı arayüz tasarımı kabiliyeti geliştirilerek nanokompozit malzemelerin performansına etki eden mekanizmaların incelenmesi amaçlanmıştır.

*“To my beloved grandmother”*



## ACKNOWLEDGEMENTS

First, I am truly thankful to my supervisor, Assoc. Prof Dr Melih Papila for the guidance, advice and support from the initial to the final level. I learned a lot from him and I truly appreciate his efforts to make me a “scientist”. I would also like to thank my co-advisor, Prof Dr Yusuf Z. Mencelođlu, for his input and constructive criticism that helped my research. I would also like to direct a special thanks to my other mentor Prof Dr Canan Atılgan which has been really helpful and supporting during the years, especially concerning the computational works performed in this thesis.

I would like to acknowledge Dr James Elliott for the guidance, advice and support during my time in University of Cambridge.

I also must give special thanks to Dr Ali Rana Atılgan, Dr Mehmet Ali Gölđün and Dr Cleva Ow-Yang who have presented creative environment for scientific discussion and have given invaluable advice for my research.

I want to also express my appreciation towards all my present and former colleagues at the division of Material Science&Engineering for the nice working environment, which has made my time at the division most pleasant. A huge thank you goes to my dearest colleagues Kaan Bilge and Dr Eren ŐimŐek for their input and friendship throughout my PhD years. I would like to thank friends Firuze Okyay, Lale IŐikel Őanlı, Sinem TaŐ, Yeliz Ekinci Unutulmazsoy and Burcu Őzel for supporting me and being with me through all the good time and bad times at SU. Though I cannot possibly list them all, special thanks to all SU members, Dr Őınar Őncel, Őzlem KocabaŐ Ataklı, Tuđçe AkkaŐ, Őzge Heinz, Őzlem Aykut, Erim Őlkümen, Kinyas Aydın, Gökçe Güven and all AC2PL members.

I am thankful to TUBITAK BİDEB 2211/2214 for providing me scholarship throughout my PhD thesis and funding to pursue my research in University of Cambridge.

My dear husband, Serdar Yenigün, deserves special thanks for providing me all the love, motivation and encouragement and about everything else I needed throughout these years. I certainly could not do this without him.

My deepest thank you goes to my parents, Sacide and Aydın Özden and my sister Elçin Özden, who have always supported me and provided me with everything I needed in life. I cannot thank them enough for everything they've have done for me.

## TABLE OF CONTENTS

ABSTRACT .....	iv
ACKNOWLEDGEMENTS .....	ix
TABLE OF CONTENTS .....	xi
LIST OF FIGURES .....	xiv
LIST OF TABLES .....	xiv
LIST OF SYMBOLS.....	xiv
LIST OF ABBREVIATIONS .....	xivx
CHAPTER 1. INTRODUCTION.....	20
CHAPTER 2. ENGINEERING CHEMISTRY OF ELECTROSPUN NANOFIBERS AND INTERFACES IN NANOCOMPOSITES FOR SUPERIOR MECHANICAL PROPERTIES .....	24
2.1. Background.....	24
2.2. Experimental Procedure .....	25
2.2.1. Copolymer Synthesis .....	25
2.2.2. Electro-spinning of PSt and P(St-co-GMA) nanofibers.....	26
2.2.3. Cross-linking of P(St-co-GMA) nanofibers.....	27
2.2.4. Fabrication of Nanofiber Reinforced Composites for DMA Testing	28
2.2.5. Characterization of the Electrospun Fibers and Composites .....	29
2.3. Results and Discussion.....	29
2.3. Concluding Remarks .....	37
CHAPTER 3. MWCNTs/P(St-co-GMA) COMPOSITE NANOFIBERS OF ENGINEERED INTERFACE CHEMISTRY FOR EPOXY MATRIX NANOCOMPOSITES.....	38
3.1. Background.....	38
3.2. Experimental Procedure .....	39
3.2.1. Material Processing and Sample Production.....	39
a. Electro-spinning of P(St-co-GMA)/MWCNTs nanofibers .....	39
b. Preparation of Nanofiber Reinforced Composites for DMA Testing .....	40

3.2.2.	Material Characterization.....	41
3.3.	Results and Discussion.....	42
3.3.1.	Polymer Solution Characteristics.....	43
a.	The stability of polymer solution containing MWCNTs.....	43
b.	Suspension Viscosity Characteristics by MWCNTs .....	44
3.3.2.	Process Optimization for Composite Electrospun Nanofibers.....	45
a.	Designing Experiments .....	45
b.	Morphology of Electrospun Fibers and Mats .....	47
3.3.3.	Detection of MWCNTs by TEM and Raman Spectroscopy.....	50
3.3.4.	Surface Wettability of Nanofibrous Webs .....	52
3.3.5.	Mechanical Characterization of Composite Nanofiber-Reinforced Hybrid Materials.....	52
3.4.	Concluding Remarks .....	56
<b>CHAPTER 4. STRUCTURAL COMPOSITES HYBRIDIZED WITH EPOXY</b>		
	<b>COMPATIBLE COMPOSITE NANOFIBROUS INTERLAYERS .....</b>	<b>57</b>
4.1.	Background .....	57
4.2.	Experimental Procedure .....	58
4.2.1.	Electro-spinning Process and Laminate Manufacturing .....	58
4.2.2.	Mechanical Testing .....	59
4.2.3.	Surface and Cross-sectional Analysis .....	60
4.3.	Results and Discussion.....	60
4.3.1.	Structural Compatibility of P(St-co-GMA)/MWCNTs Interlayer .....	60
4.3.2.	Flexural Performance by Three-Point Bending Tests.....	64
4.3.3.	Mode II Strain Energy Release Rate by ENF Tests.....	67
4.3.4.	Un-notched Charpy Impact Test Results .....	69
4.3.5.	Transverse Tensile Test Results.....	70
4.4.	Concluding Remarks .....	72
<b>CHAPTER 5. TRACING THE SUPERIOR THERMO-MECHANICAL PROPERTIES</b>		
<b>IN NANOCOMPOSITES OF CROSS-LINKED FILLERS AND INTERFACES:</b>		
<b>MOLECULAR POINT OF VIEW .....</b>		
		<b>73</b>
5.1.	Background .....	73

5.2.	Nanoscale Fingerprints of Superior Thermo-mechanical Properties in Nanocomposites .....	76
5.2.1.	Molecular Dynamics Simulations via Representative Cross-linked Unit Method.....	76
a.	Methods and Systems Studied .....	76
i.	Molecular Dynamics Methodology .....	76
ii.	Material constants for mechanical behavior .....	77
iii.	Designing representative crosslinked systems using MD simulations.....	78
b.	Results and Discussion .....	81
i.	Temperature effect on neat and reinforced cross-linked epoxy.....	81
ii.	Glass Transition Temperature Determination .....	84
c.	Concluding Remarks-I .....	85
5.2.2.	Mapping and Reverse-Mapping of Epoxy Matrix System for a Molecular Understanding of Mechanical Response.....	87
a.	Methods and Systems Studied .....	87
i.	Molecular Dynamics Methodology .....	87
ii.	Coarse-Graining of Uncross-linked Epoxy System .....	87
iii.	Calculation of Mechanical Properties via Stress-Strain Relationship.....	90
b.	Results and Discussion .....	91
i.	The Accuracy of Parameterization in Coarse-Graining.....	91
ii.	Reverse-Mapping Methodology .....	93
iii.	Preliminary Mechanical Properties of Uncross-linked Epoxy .....	97
d.	Concluding Remarks-II .....	101
	CHAPTER 6. CONCLUSION AND FUTURE WORK.....	102
6.1.	Ongoing Studies: Cross-linking Reaction at the Atomistic Scale and Reinforced Epoxy Matrices .....	102
6.2.	Conclusion .....	105
	APPENDICES .....	108
	REFERENCES .....	113
	LIST OF PUBLICATIONS.....	120

## LIST OF FIGURES

**Figure 2.1.** Chemical Structure of P(St-*co*-GMA).

**Figure 2.2.** Illustration of electro-spinning set-up.

**Figure 2.3.** Chemical Structure of (a) Epoxy resin (b) Hardener (c) Cross-linking agent ethylene diamine and (d) Cross-linked network of epoxy.

**Figure 2.4.** SEM micrographs of fibers within the fiber diameter range (a) PSt nanofibers in 300nm- 1  $\mu$ m, (b) P(St-*co*-GMA) nanofibers in 200nm - 1  $\mu$ m and (c) P(St-*co*-GMA)/EDA nanofibers in 400 nm- 2  $\mu$ m.

**Figure 2.5.** The damping ratio,  $\tan \delta$ , vs. temperature of reinforced and unreinforced epoxy specimens.

**Figure 2.6.** Storage modulus vs. temperature, reinforcement with P(St-*co*-GMA) with/without amine-sprayed nanofiber and PSt nanofiber reinforced composites compared to neat epoxy.

**Figure 2.7.** SEM micrographs of fracture surfaces: (a) neat epoxy (b) and (c) P(St-*co*-GMA)/EDA nanofiber reinforced composites.

**Figure 3.1.** Hydrodynamic radii of the polymer solution at initial stage and after MWCNTs added. The times correspond to the delay after mixing: 1, 2, 4, and 24 h; the z-average of electro-spinning solutions at initial stage, 1, 2, 4, and 24h were 410, 505, 510, 520 and 580 nm, respectively.

**Figure 3.2.** Suspension shear viscosity versus shear rate of neat polymer solutions and polymer solutions with 1% and 2% MWCNTs.

**Figure 3.3.** Experimental design. Red colored and blue colored values show the average fiber diameters (nm) and the standard deviation of fiber diameter of about 25 measurements.

**Figure 3.4.** The morphology of fibers and average diameter with standard deviations at applied voltage 15kV by varying polymer and MWCNTs concentration. The scale bars for fibers are 2  $\mu$ m.

**Figure 3.5.** Morphology of nanofibers (a) at 25 wt % polymer and 2% MWCNT concentrations, partially sprayed inhomogeneous webs (b) branched nanofibers at 27.5 wt % (c) Magnified views of bead-like structures at 25 wt % polymer and 1 % MWCNTs concentration.

**Figure 3.6.** Raman Spectra of final nonwoven webs from red laser 830 nm (300 mW).

**Figure 3.7.** HRTEM of 1.0 wt% multiwalled carbon nanotubes in P(St-*co*-GMA).

**Figure 3.9.** Frames taken during DSA measurements. Average contact angle is  $26.5 \pm 6.10^\circ$  for distilled epoxy droplet.

**Figure 3.10.** (a) Storage modulus vs temperature measurements on nanofiber-reinforced materials (reinforcement with *ten layers* of 1% MWCNTs/P(St-co-GMA) and P(St-co-GMA)) webs and neat epoxy (b) Storage modulus vs temperature measurements on nanofiber reinforced hybrid materials (reinforcement with a *single layer* of MWCNTs/P(St-co-GMA) webs with 1, 1.5, and 2% MWCNTs weight fractions) and neat epoxy.

**Figure 4.1.** Nanofiber morphologies on the prepreg surfaces: (a) and (b) at room temperature and (c) and (d) at  $100^\circ\text{C}$ .

**Figure 4.2.** Nanofibrous mat over the prepreg layers (a) Just after electro-spinning (b) 30 minutes after at  $100^\circ\text{C}$  (c) and (d) Zoomed in view for fiber/epoxy interaction at  $100^\circ\text{C}$ .

**Figure 4.3.** Cross-sectional view of fractured three point specimens. (a) (0/0/0) and (b) (90/0/90).

**Figure 4.4.** Representative force-displacement test curves for (90/0/90) laminates.

**Figure 4.5.** Fracture surfaces of (a) neat epoxy ply-to-ply interface and (b) P(St-co-GMA)/MWCNT interlayered interface (c) Zoomed in view for encircled area in 4.5b Arrows indicate the distinguishable damage marks (d) Zoomed in view for encircled area in 4.5c, arrows indicate two distinct failure regions (carbon fiber interface and through interlayer/epoxy complex) (e) Zoomed in view for encircled area in 4.5d Damage marks on interlayer/epoxy complex.

**Figure 4.6.** Cross-sectional view of a fractured transverse tensile UD test specimen (a) neat epoxy ply-to-ply interface and (b) P(St-co-GMA)/MWCNTs interlayered (c) Zoomed in view of encircled area in 4.6.

**Figure 5.1.** Five different representative cross linked units containing EPON 862 and TETA hardener (red for oxygen, gray for carbon, white for hydrogen, blue for nitrogen).

**Figure 5.2.** (a) Representative cross-linked unit bonded-III bonded to P(St-co-GMA) molecule: (b) Molecular model neat epoxy systems generated: ball-stick representation (red for oxygen, gray for carbon, white for hydrogen, blue for nitrogen).

**Figure 5.3.** (a) Bulk modulus (b) shear modulus (c) Young's modulus vs temperature results of neat (black dotted), noncross-linked (red dotted) and cross-linked (blue dotted) reinforced epoxy system.

**Figure 5.4.** The mean density values versus temperature (a) neat epoxy (b) noncross-linked reinforced epoxy and (c) cross-linked reinforced epoxy.

**Figure 5.5.** Partitioning of the beads (A, B<sub>1</sub>, B<sub>2</sub> and C) for coarse-grained simulations (red for oxygen, gray for carbon, white for hydrogen, blue for nitrogen).

**Figure 5.6.** Atomistic ball-stick representation and coarse-grained model representations of epoxy (EPON 862) and hardener (TETA) molecules, individual motion groups are represented in yellow shading.

**Figure 5.7.** Effective potential,  $V(r)$ , of (a) hardener-hardener ( $2\mathbf{xC}$  corresponds to TETA coarse-grained model) (b) epoxy-epoxy ( $\mathbf{B}_2$  beads and representative atomistic set was selected for calculation) (c) hardener-epoxy in atomistic direct MD model (black dotted) and in coarse-grained model (red dotted).

**Figure 5.8.** Reconstruction of atomic details in 100 Å simulation box, (a) Coarse-Grained representative model of uncross-linked epoxy (b) Reverse-mapped model of uncross-linked epoxy, motion groups of each atomic group was displayed.

**Figure 5.9.** Cohesive energy densities of (a) pure EPON 862 and (b) pure TETA hardener systems, from reverse-mapped (RM) (solid red line) and direct molecular dynamics (solid black line) trajectories.

**Figure 5.10.** (a) EPON862-EPON862 radial distribution functions of reverse-mapped (solid red line) and direct MD (solid black line) structures. (b) TETA-TETA radial distribution functions of reverse-mapped (solid red line) and direct MD structures (solid black line).

**Figure 5.11.** (a)  $R_g$  of EPON862 in reverse-mapped (solid red line) and direct MD (solid black line) structures. (b)  $R_g$  of TETA in reverse-mapped (solid red line) and direct MD (solid black line) structures.

**Figure 5.12.** Average transverse normal stresses in  $x$  and  $z$  directions ( $\sigma_{xx}$  (solid black line) and  $\sigma_{zz}$  (solid red line)) obtained from (a) direct MD structures and (b) reverse-mapped atomistic structures.

**Figure 5.13.** (a) Average uniaxial normal stresses in  $y$  direction ( $\sigma_{yy}$ ) obtained from direct MD (solid black line) and reverse-mapped (solid blue line) atomistic structures (b) average transverse stress differences ( $(\sigma_{xx} - \sigma_{zz})/2$ ) of direct MD (solid green line) and RM (solid blue line) structures.

**Figure 6.1.** (a) Meso-scale system built of Layer 1 and Layer 2, each layer represents different meso-molecules (b) Coarse-grained meso-system assigned by DPD force-field (c) Reverse-mapped SWNT(10,10) (space-filled) reinforced epoxy system (ball-stick model).



## LIST OF TABLES

**Table 2.1.** Glass transition temperatures and  $E'$  storage modulus of composites incorporating electrospun fibers of P(St-co-GMA) with/without ethylenediamine spraying and PSt compared to neat epoxy in 30°C and 80°C.

**Table 3.1.** Electrospun composite nanofibers by P(St-co-GMA) and MWCNTs and their assignment for nanocomposites.

**Table 3.2.** Design of experiment (factors and levels).

**Table 3.3.** The conductivity ( $\mu\text{S}/\text{cm}$ ) of MWCNTs/ 30 wt % P(St-co-GMA) solutions at different MWCNTs concentrations.

**Table 4.1.** Mechanical Test Results.

**Table 5.1.**  $T_g$  determination of neat, noncross-linked and cross-linked epoxy systems using the fitting method of the mechanical response and density average.

**Table 5.2** Properties of beads as defined in Figure 5.5. Solubility parameters,  $\delta$ , molar volume  $V_m$ , and DPD interaction parameters,  $a_{ij}$ .

## LIST OF SYMBOLS

$a_{ij}$	DPD interaction parameter
$E$	Young's Modulus
$E'$	Storage Modulus
$E_y$	Flexural Modulus
$G$	Shear Modulus
$G_{IIc}$	Mode II critical strain energy release rate
$K$	Bulk Modulus
$k_B$	Boltzmann constant
$R_g$	Radius of gyration
$S_F$	Flexural strength
$T$	Temperature
$T_g$	Glass transition temperature
$\tan\delta$	Damping ratio
$V_m$	Molar volume
$\kappa_T$	Isothermal compressibility
$\delta$	Hildebrand solubility parameter
$\chi$	Flory-Huggins interaction parameter
$\sigma_{xx}$	Normal stresses in $x$ direction

## LIST OF ABBREVIATIONS

CED	Cohesive Energy Density
CNTs	Carbon Nanotubes
DLS	Dynamic Light Scattering
DMA	Dynamic Mechanical Analyzer
DMF	<i>N,N</i> Dimethyl formamide
DPD	Dissipative Particle Dynamics
EDA	Ethylene diamine
ENF	End Notched Flexure
HRTEM	High-Resolution Transmission Electron Microscopy
GPC	Gel Permeation Chromatography
MD	Molecular Dynamics
MS	Materials Studio
NMR	Nuclear Magnetic Resonance
NPT	Isothermal-Isobaric Ensemble
NVT	Canonical Ensemble
PDI	Poly dispersity Index
PSt	Polystyrene
RDFs	Radial Distribution Function
RM	Reverse-Mapping
SEM	Scanning Electron Microscopy
UTM	Universal Testing Machine

## CHAPTER 1

### INTRODUCTION

Polymer nanocomposites have exhibited extra-ordinarily interesting properties typically attributed to the large specific surface area of the nano-scale fillers. Compared to traditional composites of micron-filled polymers, nano-size fillers such as CNTs and nanofibers lead to a dramatic increase in interfacial area [1]. Higher interfacial region in nanocomposites means higher volume fraction of interfacial polymer with properties different from bulk polymer properties even at low loadings (less than 5 vol. %) [1]. Almost the entire matrix can be interfacial polymer[1]. Thus, structure and properties of the interfacial region are not only different from the bulk, but also critical to controlling properties of overall nanocomposite. In cross-linked matrices, for instance changes in the crosslink density due to molecule migration to or from the interface plays role on the ultimate mechanical behavior. An interface of attractive potential decreases the mobility of polymer chains, and produce stiffer composites.[1] Predicting the mechanical properties of nanocomposites while tuning interfacial region is quite challenging. Therefore, multi-scale insight and approach are required to understand interfacial polymer behavior and to generate models for appropriate materials design.

*Problem Statement:* Nanocomposites are materials where the interface is of extreme importance due to the high interfacial surface area. Therefore, a major issue to address for widespread and more effective use of nanocomposites has been the compatibility of the fillers, CNTs and nanofibers, at their interface with polymeric matrices. The choice of nanofiber material and chemical composition need to promote stronger interface with

the polymeric matrix so that superior mechanical properties and performance of the nano-scale interface can propagate into macro-scale performance.

Considering the multi-scale nature of the nanocomposites, the objectives of this dissertation are set as twofold: 1) experimentally to demonstrate the smart choice of materials to promote the signature of the nano-scale phenomenon, nanofiller-polymer interface onto the macro world of the nanocomposites; 2) to explore an efficient computational tool that can correlate well with the experimental findings facilitating the smart choices for building-up the interface design signature into the macro-properties.

*Hypothesis:* Stronger/attractive potential interfacial region prevent early failure, leading to nanocomposites with enhanced mechanical behavior. Therefore, our hypothesis is that incorporation of electrospun surface modified/reactive nanofibers with epoxide functional groups into the epoxy resin results in significant improvements in the mechanical properties. Additional ultrastrong nanoreinforcement such as multi walled carbon nanotubes can also be embedded into entangled nanofiber network. The polymer nano-fibrous mat based reinforcements should improve composite strength, durability, and impact resistance when their chemistry is tuned-in for stronger interface with the epoxy matrix.

*Approach and Research Plan:* The two objectives of this thesis describe the methodologies as well. First, knowledge of the epoxy matrix chemistry and the motivation for the tuned-in and compatible interface suggests the candidate reinforcing nanofiber material as styrene based, but co-polymerized with the GMA nanofibers. Thermo-mechanical tests are carried out for the demonstration of the effect of nano-scale phenomenon through cross-linked interface onto the macro properties. Numerical simulations are then employed to address the atomistic scale signature of the compatibility of the constituents for a stronger nanofiber-matrix interface. Molecular dynamics simulations and their hybrid use with the coarse-grain models- so called DPD and reverse mapping methodology are implemented.

*Output:* Coupled with focused experimental study on the interface providing the proof-of-concept, present modeling efforts are helping to elucidate the physical mechanisms that underlie nanocomposite bulk performance and ultimately aimed to enable efficient design of nanocomposites. As a result of these efforts three articles in

international prestigious journals and three proceedings in international conferences have been published (See Appendix A).

*Outline:* The novelty of the work in *Chapter 2* is based on designing the chemistry of the electrospun nanofibers, so that the resultant composites substantially benefit from cross-linking between the nanofibers and the polymer matrix. Cross-linked fiber structure and surface chemistry of the electrospun fibers leading to cross-linked polymer matrix-nanofiber interfacial bonding result in increased mechanical response and are discussed in detail. This work is also available in *ACS Applied Materials and Interface Journal*. [2]

*In Chapter 3;* strengthened nanofiber-reinforced epoxy matrix composites are then also demonstrated by engineering composite electrospun fibers of multi-walled carbon nanotubes (MWCNTs) and reactive P(St-co-GMA). MWCNTs are incorporated into surface modified, reactive P(St-co-GMA) nanofibers by electro-spinning. Functionalization of these MWCNT/P(St-co-GMA) composite nanofibers with epoxide moieties facilitates bonding at the interface of the cross-linked fibers and the epoxy matrix, effectively reinforcing and toughening the epoxy resin. The effect of MWCNTs is investigated beginning with the polymer concentration during the electro-spinning process until the mechanical response. This part of study has been published in *ACS Applied Materials and Interface Journal*. [3]

*In Chapter 4,* the focus is on the structural integrity of the electrospun P(St-co-GMA) based nanofibers as interlayers in conventional carbon fiber/epoxy prepreg to enhance transverse matrix cracking and delamination in macro scale. The overall mechanical performance increase through the incorporation of nanofibrous interlayers is reported via different test methods. This research was performed in collaboration with Kaan Bilge, and was published in *Composite Science and Technology Journal* [4] reveals the applicability of the nanofibrous webs on the macro-scale.

*Chapter 5* traces the effect of nanofiller chemistry and cross-linking on mechanical behavior of thermoset polymer matrix nanocomposites via numerical simulations. We probe the mechanism of reinforcing at the interface where molecular interactions can be monitored. Molecular dynamics (MD) simulations are employed to address the differences in the temperature dependence of the bulk, shear and Young's modulus when the characteristics of fiber-epoxy interface in the nanocomposites are modified [5,

6]. In addition, an efficient multi-scale model is proposed to build cross-linked epoxy matrix by tuning cross-linking degree and nanofiller chemistry. The computationally trackable multi-scale approach opens a new window into understanding and manipulating the reinforcing function in cross-linked matrices.

*Chapter 6* summarizes major conclusions and followed by our ongoing and future works on engineered interface. Multi-scale experimental and analytical research efforts offer new insights to reinforcing function at the interface while monitoring mechanical response on all scales.

## **CHAPTER 2**

### **ENGINEERING CHEMISTRY OF ELECTROSPUN NANOFIBERS AND INTERFACES IN NANOCOMPOSITES FOR SUPERIOR MECHANICAL PROPERTIES**

#### **2.1. Background**

Nano-scaled constituents in composites are of interest due to their potential for significantly improving the composite material properties [7-13]. Nano- to submicron-scale polymeric fibers formed by electro-spinning, for instance, are recently being explored for their reinforcing ability in composites [14-25]. By forming a network of the fibers, electro-spinning secures the uniform planar dispersion of the fibers that can be preserved, when used in polymeric matrix composite materials [26]. The process also results in a large draw ratio, causing extended chain conformations and highly crystalline regions of polymer structure in favor of fiber mechanical properties [27]. The electrospun polymeric fibers were utilized as reinforcement to enhance particularly the matrix-dominated flexural properties of cross-linked polymer matrix composites [14, 16, 26-28]. Recently, cellulose, nylon 4,6, carbon nanofiber, polyvinyl alcohol (PVOH), poly(l-lactide) (PLLA), polyacrylonitrile (PAN), polymethyl-methacrylate (PMMA) polymeric and nanoscaled glass electrospun fibers were successfully employed to reinforce a polymer matrix [14, 15, 17-25]. It was demonstrated [29] that strong interfacial bonding has been crucial to benefit from the unique properties of



nanofibers for composite reinforcement. Since nano-scaled materials have enormous surface area, interfacial sliding of the nanoscale fillers in the polymeric matrices may result in an extremely efficient mechanism for damping enhancement [29]. Additionally, strong surface interactions enable good mechanical interlocking with surrounding polymer chains [30], thereby strengthening the nanocomposites. Hence, several researchers [20, 23, 25, 31] have studied the importance of interfacial bonding to obtain better mechanical performance, due to nano-structures as composite reinforcements. However, the investigations specific to the cross-linked nanofiller-matrix interface for better interfacial bonding are still needed.

In this chapter, we claim that incorporation of electrospun surface modified/reactive nanofibers with epoxide functional groups into the epoxy resin would result in significant improvements in the mechanical properties. To investigate this claim, along with polystyrene (PSt) nanofibers, surface-activation capable polystyrene-co-glycidyl methacrylate P(St-co-GMA) nanofibers were also produced by electrospinning. The surface chemistry of these fibers is expected to improve interfacial bonding with the epoxy based polymer matrix, as the glycidylmethacrylate (GMA) structure contains epoxide ring-promoting cross-linking across the interface. An experimental procedure was designed to explore the effects of the presence of nanofibrous layers, the GMA composition in the fiber chemical structure and supplement by a cross-linking agent (ethylenediamine, EDA) that was applied onto the fibers by spraying, prior to embedding the fibrous mats into epoxy matrix. These parameters namely, the chemistry or the functional groups of the nanofibers and cross-linking agent, were investigated primarily for the mechanical response and thermal stability of the polymer nanofiber reinforced epoxy matrix composites.

## **2.2. Experimental Procedure**

### **2.2.1. Copolymer Synthesis**

The monomers styrene (purified) and glycidylmethacrylate (GMA) were supplied by Aldrich Chemical Co, while the solvents, N, N dimethylformamide and methanol, were purchased from Merck Chemicals Co. Copolymer P(St-co-GMA) (See Figure 2.1)

were synthesized by solution polymerization technique as well as polystyrene. Purified styrene and GMA (by weight fractions: 90% St and 10% GMA) were put into a test tube in an ice bath. Dimethylformamide (DMF) was then added into St-GMA monomer mix such that volume proportions were 3 to 2, respectively. The initiator azobisisobutyronitrile (AIBN) was added into the test tube flushed with nitrogen. The tube containing the dissolved monomers was then kept for 24 hours in the constant temperature bath at 65°C for the polymerization reaction. Finally, the polymer solution was poured out into a beaker containing methanol and the methanol/polymer mixture was filtered and dried in an oven at 60°C for 2 hours. The synthesized P(St-co-GMA) copolymer structure was determined by proton magnetic resonance spectroscopy (<sup>1</sup>H-NMR). Molecular weights and polydispersities (PDI) were measured by a gel permeation chromatography (GPC) system and the range was recorded as 110,000 and 160,000 g/mol. (1.35-1.45 PDI).

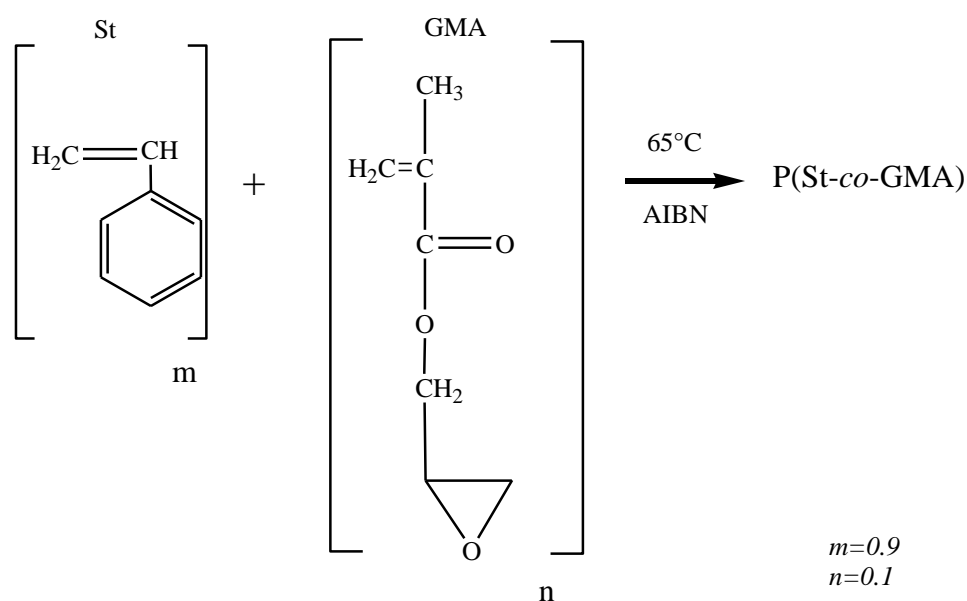


**Figure 2.1** Chemical Structure of P(St-co-GMA).

### 2.2.2. Electro-spinning of PSt and P(St-co-GMA) Nanofibers

Polymer solutions PSt/DMF and P(St-co-GMA)/DMF, at 30 wt% polymer concentration, were prepared at room temperature. The solutions were stirred magnetically for 24 hour to obtain homogeneity and then electrospun to produce the non-woven fiber mats. The schematic of the electro-spinning setup is shown in Figure 2.2. An electrical bias potential (via Gamma High Voltage ES 30P-20W) was applied to



$$\% \text{ gel fraction} = 100 - \% \text{ sol fraction} \quad (2.2)$$

where  $m_f$  is the dry mass of the extracted sample and  $m_i$  is the initial mass of the sample [32]. The analyses showed that gel fraction of cross-linked fibers was between 68%-71% whereas P(St-co-GMA) fibers were completely soluble in DMF before the EDA spraying. It should also be noted that addition of cross-linking agent directly to the polymer solution prior to electro-spinning was also done. However, immediate changes in the solution characteristics due to triggered cross-linking prevented the production of fibers of the desired characteristics.

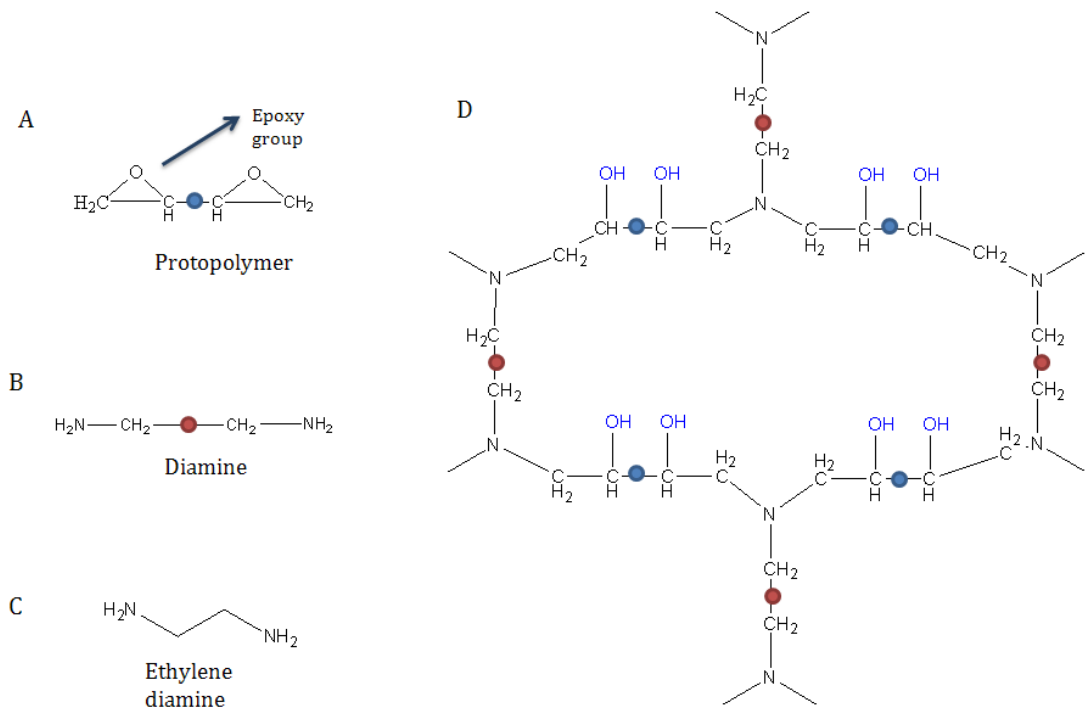


**Figure 2.3.** Chemical Structure of (a) Epoxy resin (b) Hardener (c) Cross-linking agent ethylene diamine and (d) Cross-linked network of epoxy.

#### 2.2.4. Fabrication of Nanofiber Reinforced Composites for DMA Testing

Sets of cross-linked P(St-co-GMA)/EDA fibers, along with PSt and P(St-co-GMA) as received fibers, were first cut into 12 mm x 50 mm pieces. The thickness of the electrospun fiber mat layer is approximately 25  $\mu\text{m}$ . Next, the fiber mats were embedded into epoxy resin (Hunstman Adv. Mat. Co. Araldite® LY 564 and XB 3404)

layer by layer, using a Teflon mold custom-designed for the net-shape of DMA specimen. The epoxy matrix composites reinforced by 10 layers of the fiber webs (corresponding approximately 2% fiber weight fraction) were cured at 50° for 15 hours and DMA specimens of size 2mm x 12mm x 50mm were obtained. Note that the fiber weight fraction of 2% here was a representative amount for the proof of cross-linking fiber/matrix interface concept, but the fiber content is an important factor to look into in future studies.

### **2.2.5. Characterization of the Electrospun Fibers and Composites**

Glass transition temperatures ( $T_g$ ) of the nanofiber-reinforced composites were determined by using a dynamic mechanical thermal analyzer (Netzsch DMA 242). Morphologies of PSt, P(St-co-GMA) and P(St-co-GMA)/EDA fibrous webs and fracture surfaces of the neat epoxy and nanofiber-reinforced composites were evaluated by scanning electron microscopy containing field emission gun (SEM LEO 1530VP) using secondary electron detector at 2kV. Both the electrospun mats and nanofiber reinforced composites were carbon coated for better electrical conduction. The DMA tests of the neat epoxy and nanofiber reinforced composites were performed in three point-bending mode at a frequency of 1 Hz over a temperature range of 20°- 90° C. Testing limits on amplitude, maximum dynamic force and static constant force were set as 30  $\mu$ m, 3 N and 0.01 N, respectively. Ten samples for each of the three fiber types were tested. Finally, a universal testing machine (UTM, ZWICK Proline Z100) was used to determine flexural strength and flexural modulus at room temperature using the ASTM D790 standard.

## **2.3. Results and Discussion**

It is vital to confirm that electro-spinning of the polymer solutions resulted in fibrous formation, based on the selected processing parameters. The morphologies of PSt and P(St-co-GMA) electrospun fibrous mats are shown in the SEM images in Figures 2.4a and b. The images demonstrate that bead-free fiber formation was achieved, and the diameter of PSt and P(St-co-GMA) fibers is in the range of 200 nm–

1  $\mu\text{m}$ . The variance in the fiber diameter is rather high and calls for a systematic study aiming for optimal process conditions of the minimal diameter and variance. A design-of-experiments-based study is detailed in *Chapter 3*.

The SEM micrograph of P(St-co-GMA)/EDA ribbon like fibers (Figure 2.4c) demonstrates that cross-linking was induced by the spraying of EDA on P(St-co-GMA) fibers. The cross-linked fiber diameter was in the range of 400 nm-2  $\mu\text{m}$  due to swelling caused by ethylenediamine. These changes on the morphology and solubility tests suggest that a high degree of cross-linking, around 70% occurred.

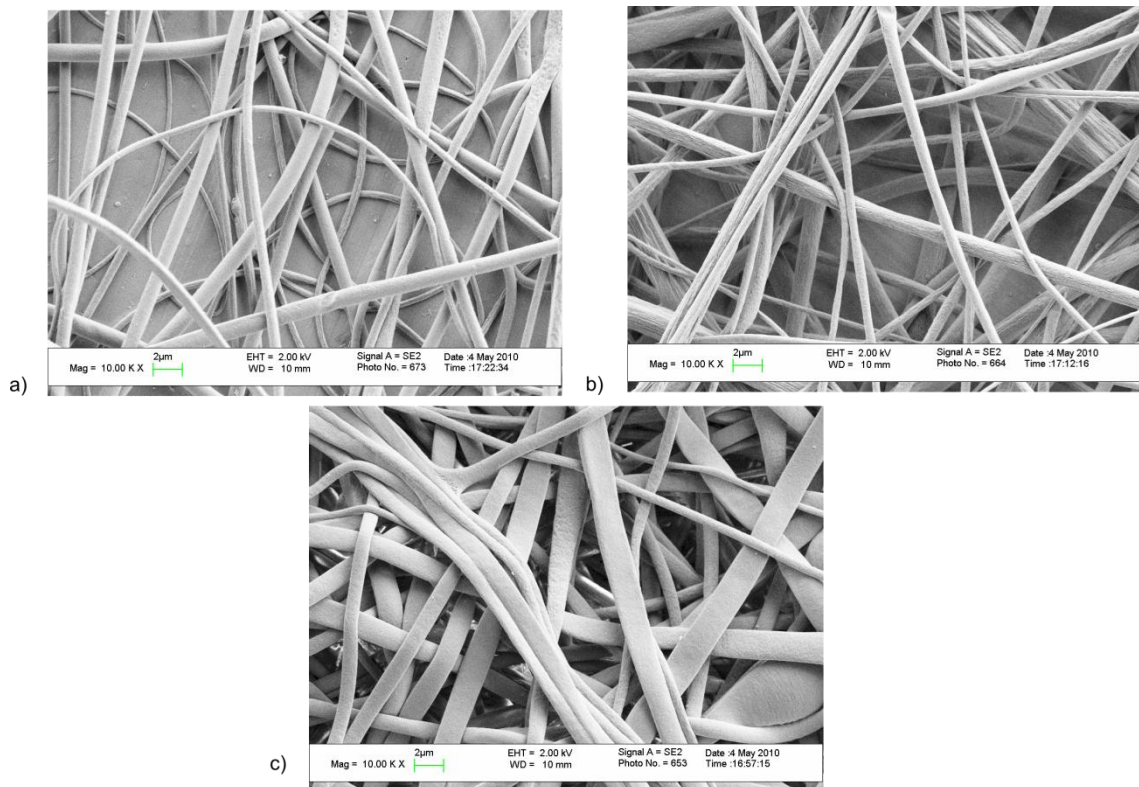


**Figure 2.4.** SEM micrographs of fibers within the fiber diameter range (a) PSt nanofibers in 300nm- 1  $\mu\text{m}$ , (b) P(St-co-GMA) nanofibers in 200nm - 1  $\mu\text{m}$  and (c) P(St-co-GMA)/EDA nanofibers in 400 nm- 2  $\mu\text{m}$ .

As the primary objective in this work is to enhance the interface performance by designing or engineering the surface chemistry of nanofibers, it is essential to assess the interface-related properties. The damping ratio, or loss tangent curves, recorded by DMA can be considered as one of the metrics for improved interfacial bonding. The damping ratio ( $\tan \delta$ ) reflects the ability of the material to dissipate energy, and in the case of composite or multiphase materials, interaction between the inner phases and interfaces dominate the energy dissipation [30, 33-36]. The energy loss at the interface

depends on the product of applied internal forces and the slipping displacement [37]. Zhou *et al.* [36], for instance, proposed “interfacial stick slip mechanism” for damping in nanofiller reinforced composites. Considering the inversely proportional influence of the interfacial strength on the slipping displacement, surface-modified nanofiber-reinforced composites with enhanced interfacial bonding is anticipated to result in smaller slipping displacement. Thus, the energy dissipation is reduced due to less slippage, causing the decrease in damping ratio. This is evident in Figure 2.5 among the  $\tan \delta$  comparison of the electrospun fiber reinforced composites. The damping ratio of PSt nanofiber reinforced composites, for instance, was higher than that of P(St-co-GMA) nanofiber reinforced composites for which the fiber-matrix interface is improved and stronger. The curve associated with the P(St-co-GMA)/EDA nanofibers is the broadest with the lowest amplitude, an indication of the improved compatibility or interface with the polymer matrix [23]. On the other hand, all of the embedded fiber mats here resulted in substantial increase in stiffness at a cost of damping ratio compared to the neat epoxy (Figure 2.5 and Figure 2.6). The reinforcing and stiffening effect due to good adhesion and load transfer between nanofibers and epoxy matrix appear to override the damping ratio enhancement that can be obtained due to interfacial interactions in nanocomposites when compared to neat polymer matrix. The reinforcement-damping tradeoff reported here is also consistent with literature; the results presented by Suhr *et al.* [30], for instance, on silica particle reinforced/stiffened nanocomposites.

Table 2.1 summarizes the glass transition temperature  $T_g$ , and loss tangent,  $\tan \delta$  determined by DMA ( $T_g$  is considered herein as the temperature associated with the peak of  $\tan \delta$ ). It shows that  $T_g$  of the nanofiber-reinforced epoxy matrix composites is higher than that of the neat epoxy. When attractive interactions are present at a polymer-nanofiller interface, confinement lead to enhancements rather than depressions in  $T_g$  relative to neat values [38]. Ellison *et al.* indicated that the origin of  $T_g$  nanoconfinement effect is related to surfaces and interfaces modifying relevant  $T_g$  dynamics [39]. At the interface, formed bonds restrain cooperative segmental mobility and lead to an increased  $T_g$  [40, 41].

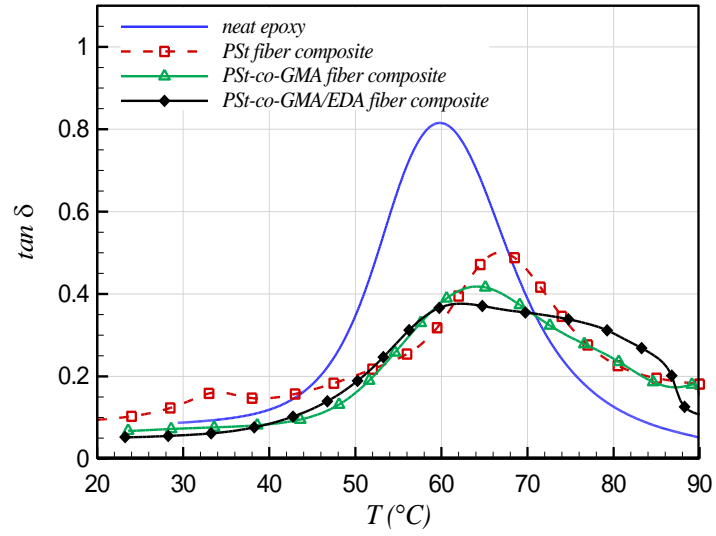


**Figure 2.5.** The damping ratio,  $\tan \delta$ , vs. temperature of reinforced and unreinforced epoxy specimens.

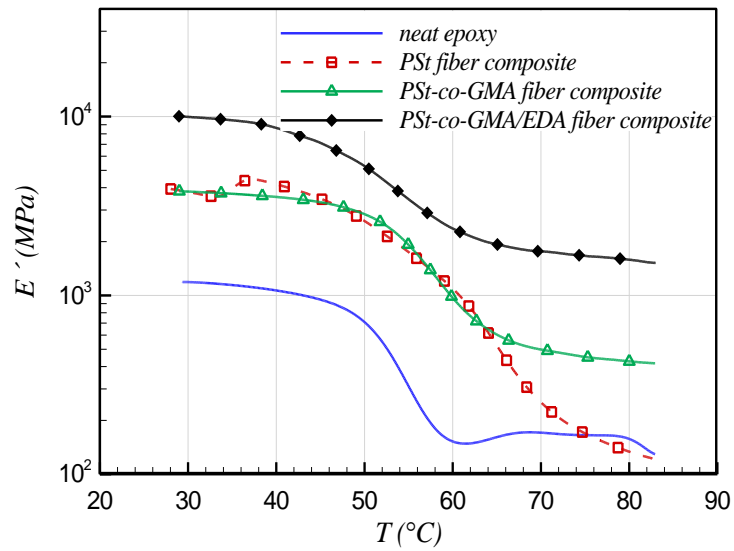


**Figure 2.6.** Storage modulus vs. temperature, reinforcement with P(St-co-GMA) with/without amine-sprayed nanofiber and PSt nanofiber reinforced composites compared to neat epoxy.



**Table 2.1.** Glass transition temperatures and  $E'$  storage modulus of composites incorporating electrospun fibers of P(St-co-GMA) with/without ethylenediamine spraying and PSt compared to neat epoxy in 30°C and 80°C.

Specimen	$T_g$ °C (peak tan $\delta$ )	Damping Ratio (tan $\delta$ )	$E'$ Storage Modulus (MPa) @ 30°C	$E'$ Storage Modulus (MPa) @ 80°C
Neat Epoxy	60.1	0.679	1187±50	130±3
Epoxy Reinforced by PSt Nanofibers	67.0	0.471	3939±50	130±10
Epoxy Reinforced by P(St-co-GMA) Nanofibers	64.8	0.397	3825±100	415±15
Epoxy Reinforced by P(St-co-GMA)/EDA nanofibers (with crosslinker agent spraying)	65.6	0.372	10038±100	1570± 15

It is known that large surface area of the fillers and associated interfacial bonding play a significant role in enhancing mechanical properties of the multiphase, composite materials [42]. The effectiveness of the nanofiber reinforcement is anticipated to correlate strongly with the quality of the interfacial bonding between the nanofibers and epoxy matrix. In support of this correlation, the sensitivity to the interfacial bonding was well captured in the storage modulus data from DMA tests, by which the three choices of nanofiber surface chemistry/treatment were investigated. Table 2.1 also summarizes the storage moduli ( $E'$ ) by DMA for the composites and the neat epoxy at 30°C and 80°C. The complete temperature scans are also reported here in Figure 2.6. Upon closer examination, the results indicate that incorporation of 2% weight fraction of PSt nanofibers in epoxy was remarkably effective on increasing the storage modulus of the composite at 30°C. There is more than a factor of three improvement by PSt nanofiber reinforcement, compared to neat epoxy. However, the influence of these fibers gradually decayed as the temperature was increased beyond the  $T_g$  of the composite. At 80°C, which is well above the curing and glass transition temperature, the mean storage moduli of PSt/epoxy composite and the neat epoxy are about the same. The PSt nanofibers and epoxy both are of similar aromatic structures that can

promote the interaction of the two materials. This results in the reinforcing effect provided by the PSt fibers. On the other hand, a significant downgrade in reinforcement at elevated temperature is attributed to the fact that PSt nanofibers and epoxy do not form strong chemical bonding or cross-linking across the interface, and its absence becomes further evident beyond the  $T_g$ .

In contrast, the chemistry of P(St-*co*-GMA) fibers introduces an epoxide group that could react with the NH group in the hardener for epoxy resin, so that the stable supplementary cross-linking with the epoxy matrix is promoted. Outlook for the P(St-*co*-GMA)/epoxy composite is also similar at 30°C, but these surface-designed fibers appeared to preserve their contribution and influence in the storage modulus at elevated temperature as well. At 80°C beyond the  $T_g$  of the material, the storage modulus reached a plateau, where the increase was still around a factor of three compared to the neat epoxy. Comparison of the storage modulus curves associated with PSt and P(St-*co*-GMA) fibers revealed that the benefit in the mechanical response due to presence of the fibers is preserved at elevated temperatures by supplementary GMA-epoxy interaction. To retain the high modulus even above the  $T_g$ , enhanced adhesion between nanofiber and matrix is needed, as also observed in modified clay-epoxy nanocomposites [35].

The next question was whether the proven effect of nanofiber reinforcement with purpose-designed surface chemistry can be further enhanced, as far as the mechanical response is concerned. A stronger fiber-matrix interface was aimed by reinforcement of the P(St-*co*-GMA) nanofibers, featuring epoxide rings in the surface chemistry and an additional process step of overcoating with the cross-linking agent ethylenediamine, before the resulting P(St-*co*-GMA)/EDA fibrous mats were embedded into the epoxy matrix. DMA results indicated that the storage modulus of epoxy reinforced with 2 wt% mass fractions of P(St-*co*-GMA)/EDA nanofibers was about an order of magnitude higher than the neat epoxy (See Table 2.1 and Figure 2.6).

Cross-linking agent ethylenediamine applied by spraying over the fibrous mats introduced significant improvement on mechanical behavior due to epoxide ring-amine group interaction. It is attributed to increased cross-linking density by two mechanisms: a) the nanofibers were themselves cross-linked, leading to an increase in inherent stiffness within the fibrous mat [18] (Figure 2.4), b) the amine residue on the nanofiber surfaces reacted with the surrounding epoxy matrix. As a result, the

reinforcing effect of P(St-co-GMA)/EDA nanofibers was more than twice of the reinforcement by P(St-co-GMA) nanofibers.

In addition, SEM micrographs in Figure 2.7a demonstrated that the fracture surface of neat epoxy was smooth and consisted of large surface steps, as also observed by Fong [19] and Hsieh *et al.* [43]. Nanofiber reinforced composites, on the other hand, have numerous fracture lines in smaller steps which appear to be associated with the fiber distribution, as shown in Figure 2.7b. These rough fracture surfaces including fiber breakages could be explained by their fracture energies where nanofiber reinforced composites exhibit higher fracture energy compared to neat epoxy [43]. Resistance to failure due to nanofibers can be explained by a “bridging mechanism” [44-46]. When a micro scale crack is initiated under flexural load, the surface modified nanofibers support the load and resist the crack opening, as shown in Figure 2.7c. As a result, the epoxy matrix is reinforced and toughened.

The flexural strength ( $S_F$ ) and flexural modulus ( $E_Y$ ) of the neat resin and nanocomposites containing single layer of nanofibrous mat, corresponding 0.2 wt% of electrospun P(St-co-GMA) nanofibers reinforced composites were also tested at room temperature. ASTM- D790 3-point-bending standard mechanical tests demonstrated that embedding a *single layer* of a PSt, P(St-co-GMA), P(St-co-GMA)/EDA nanofibrous mat increased the flexural modulus ( $E_Y$ ) by 23%, 27% and 30% with respect to that of the neat epoxy. The flexural strength ( $S_F$ ), when reinforced with 0.2% mass fraction of PSt, P(St-co-GMA), P(St-co-GMA)/EDA nanofiber, increased by 9%, 16% and 23%, correspondingly.

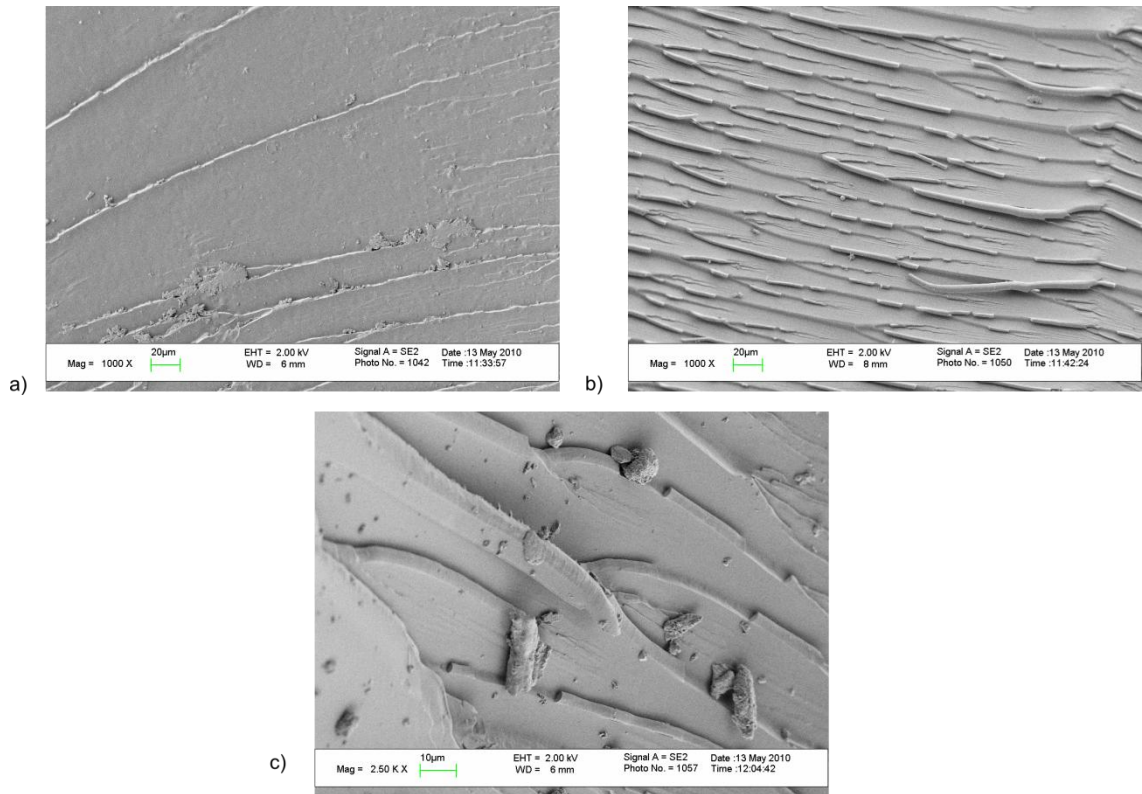


**Figure 2.7.** SEM micrographs of fracture surfaces: (a) neat epoxy (b) and (c) P(St-co-GMA)/EDA nanofiber reinforced composites.

## 2.4. Concluding Remarks

Three different electrospun fiber chemistries were studied for their reinforcing abilities when embedded into epoxy resin. Specifically, PSt, P(St-co-GMA) and P(St-co-GMA)/EDA electrospun fibers were utilized. The near-room-temperature performances of PSt and P(St-co-GMA) fibrous mats were quite similar, all showing a three-fold increase in storage modulus compared to that of neat epoxy. Beyond the  $T_g$ , effect of PSt, which had decayed, the reinforcing ability by P(St-co-GMA) was preserved. The performance of the cross-linked P(St-co-GMA)/EDA nanofibers, on the other hand, was far superior to composites of the other two fibers. Thermomechanical tests under flexural loads indicated that incorporation of low weight fraction (2wt %) P(St-co-GMA)/EDA nanofibers in epoxy are 10 and 2.5 times higher than neat and P(St-co-GMA) nanofiber reinforced epoxy, respectively, even beyond the glass transition temperature  $T_g$ . The significant increase in the mechanical response is attributed to the combined effect of the two factors: the inherent cross-linked fiber structure and the surface chemistry of the electrospun fibers leading to cross-linked polymer matrix-nanofiber interfacial bonding.

## CHAPTER 3

### MWCNTS/P(ST-CO-GMA) COMPOSITE NANOFIBERS OF ENGINEERED INTERFACE CHEMISTRY FOR EPOXY MATRIX NANOCOMPOSITES

#### 3.1. Background

Since the discovery of carbon nanotubes (CNTs) [47], they have attracted a lot of attention in materials and applied research due to their unique and fascinating structure and properties [48-52]. One specific application is the use of CNTs in polymer fibers to impart dramatically enhanced strength and toughness in the fibers [53-56]. The incorporation of CNTs into the polymeric media via electro-spinning, has been demonstrated to significantly improve the mechanical properties of the electrospun composite fibers [55, 57-59]. It is recognized that this technique is an ideal route to translate the unique superior properties of CNTs to meso and macro-scale structures [55] by first embedding the CNTs in the fibers and then incorporating of these composite fibers into a polymer matrix, successively.

Electro-spinning is a widely used process for forming ultrafine fibers by electrostatically induced self-assembly [60]. One of the challenges of the electro-spinning technique is controlling material and process parameters that affect the various properties and characteristics, such as overall strength, fiber diameter and morphology [61]. Electrospun polymeric nanofibers are recently being explored for their reinforcing ability in composites [14, 15, 20-22, 25]. They were utilized to specifically enhance the matrix-dominated mechanical properties of cross-linked polymer-matrix composites [2, 14, 28]. Several researchers [20, 25] have studied the use of interfacial bonding to

improve better mechanical performance, in nano-structure reinforced composites. In this application of polymer-matrix nanocomposites, as also described in *previous chapter* we demonstrated that the significant increase in the mechanical response is attributed to the combined effect of the two factors: the inherent cross-linked electrospun fiber structure and their surface chemistry lead to bonding at the interface between nanofibers and the cross-linked polymer-matrix.

In *this chapter*, the objective is to introduce CNTs into the nanofibers and nanocomposite system. The hypothesis herein is that it can be advantageous to electrospun reactive polymer nanofibers with CNTs for substantially improving the strength and toughness of composite nanofiber-reinforced epoxy due to both the inherent homogeneous distribution of CNTs and the affinity of the resultant composite fibers for epoxide group functionalization. Our present experimental procedure began with exploring the effect of CNTs along with the polymer concentration during the electro-spinning process. A factorial design of experiments (DOE) was performed to determine optimal set of parameters for polymer concentration and MWCNT concentration for effective electrospun fibrous nano-reinforcement of the epoxy matrix. The composite nanofibers as determined by this DOE were characterized primarily to achieve reproducible nanofibrous mats. Next, the mechanical response and thermal stability were also investigated for the CNT/polymer nanofiber-reinforced epoxy matrix composites.

## **3.2. Experimental Procedure**

### **3.2.1 Material Processing and Sample Production**

#### **a. Electro-spinning of P(St-co-GMA)/MWCNTs Nanofibers**

P(St-co-GMA) copolymer was synthesized using the same procedure as described in *Chapter 2*. P(St-co-GMA) was dissolved at three different concentrations 25 wt%, 27.5 wt% and 30 wt% in DMF. Multiwalled carbon nanotubes purity of 99% was then added to improve the mechanical properties of electrospun nanofibrous webs. The nominal diameter and length range of MWCNTs (Bayer Material Science-baytubes

C150 HP) were 5-20 nm and 1-10  $\mu\text{m}$ , respectively. No surface modification on CNTs was employed in this work. They were dispersed in polymer solutions at different mass fractions/concentrations (1%, 1.5% and 2%) by mechanical stirring. With three levels of each variable, the polymer concentration and MWCNT mass fraction, a total of nine different combinations were used to produce nanofiber (Table 2.1). The solutions were stirred magnetically for another 24 h at room temperature, to ensure homogeneity. The polymer solutions with dispersed MWCNTs were then electrospun to produce the non-woven fiber mats. An electrical bias potential (Gamma High Voltage ES 30P-20W) was applied to the polymer solutions, which were contained in a 2-mL syringe. An alligator clip attached to the syringe needle (diameter 300  $\mu\text{m}$ ) enabled biasing of the solution. The applied voltage was adjusted to 15kV, while the grounded collector covered with aluminum foil was placed 10 cm away from the syringe needle tip. A syringe pump (NewEra NE-1000 Syringe Pump) was used to maintain a solution flow rate of 30  $\mu\text{L/h}$  during electro-spinning.

#### **b. Preparation of Nanofiber Reinforced Composites for DMA Testing**

The experiments for electrospun MWCNT/P(St-co-GMA) composite nanofiber processing are summarized in Table 3.1, along with the designation of candidates for embedding in an epoxy matrix. The nanofiber mats were first cut into 12 mm x 50 mm pieces. The mean specific surface area of a typical electrospun fiber mat layer in this work is approximately 32.2  $\text{g/m}^2$ , obtained when electro-spinning 2 mL of polymer solution. Next, the fiber mats with thickness around 30  $\mu\text{m}$  were embedded into epoxy resin (Hunstman Adv. Mat. Co. Araldite® LY 564 and XB 3404) layer by layer, using a Teflon mold custom-made for the net-shape of DMA specimen. The epoxy matrix composites were reinforced by 1 and 10 layers of the fiber webs (corresponding approximately 0.2 and 2 % fiber weight fraction) and were cured at 50°C for 15 hours, and then subsequently postcured at 80°C for 48 hours.



**Table 3.1.** Electrospun composite nanofibers by P(St-co-GMA) and MWCNTs and their assignment for nanocomposites

Run	Polymer concentration (wt %)	MWCNT concentration (%)	Nanofiber reinforced composites
#1	25	1	NO
#2	25	1.5	NO
#3	25	2	NO
#4	27.5	1	NO
#5	27.5	1.5	NO
#6	27.5	2	NO
#7	30	1	<b>YES</b>
#8	30	1.5	<b>YES</b>
#9	30	2	<b>YES</b>

### 3.2.2 Material Characterization

For characterizing the materials and processes in this work, a variety of techniques and equipments were used. . Dynamic light scattering (DLS) measurements were carried out on Malvern Instrument DLS Zetasizer Nano ZS equipment to probe the hydrodynamic radius distribution of the MWCNTs, as a measure of the long term stability of electro-spinning solutions. The effect of MWCNTs on viscosity of the solutions, a key factor in the electro-spinning process, was elucidated by using a Malvern Bohlin CVO rotational rheometer. The shear viscosity of the solutions for the electro-spinning process was measured at a range of control shear stresses from 10 Pa to 1000 Pa. The morphologies of MWCNTs/P(St-co-GMA) fibrous webs were evaluated by imaging using 2keV secondary electrons in field-emission gun equipped scanning electron microscope (FE-SEM, LEO 1530VP). In addition, the dispersion of MWCNTs on the nanofiber was evaluated by using HRTEM (JEOL 2100). The diameter of electrospun nanofibers was estimated by the image processing toolbox of

MATLAB. The average fiber diameter and distribution were determined from about 25 measurements on the randomly selected fibers. Furthermore, drop shape analysis was performed to investigate the contact angle response of the webs for water and epoxy resin. The contact angles were measured on a Krüss GmbH DSA 10 Mk 2 goniometer with DSA 1.8 software. More than eight 5-mg droplets of distilled ultra-pure water and uncured epoxy resin/hardener mixture were averaged. To verify the presence of MWCNTs in the composite nanofiber mats, the Raman spectroscopy (Renishaw InVia Reflex Raman Microscopy System; Renishaw Plc., New Mills, Wotton-under-Edge Gloucestershire, UK) was used. The 830 nm laser was used to probe structural response which was in the range  $2000\text{-}500\text{ cm}^{-1}$ . The thermo-mechanical behavior and characteristics of the MWCNTs/P(St-co-GMA) fiber-reinforced epoxy matrix composites were also explored. Storage modulus was determined by using a dynamic mechanical thermal analyzer (Netzsch DMA 242). The DMA tests of nanofiber-reinforced hybrid materials along with the neat epoxy specimens were performed in three point-bending mode at a frequency of 1 Hz over a temperature range of  $25^{\circ}\text{-}150^{\circ}\text{ C}$ . The amplitude, maximum dynamic force and static constant force parameters were set as  $30\text{ }\mu\text{m}$ , 5 N and 0.01 N, respectively. Five samples were tested for each DMA analysis. Finally, a universal testing machine (UTM, ZWICK Proline Z100) was used to determine flexural strength and flexural modulus at room temperature using the ASTM D790 standard. Eight samples were characterized for each UTM test.

### 3.3. Results and Discussion

The electro-spinning of polymer solutions containing MWCNTs is a complicated process. Specifically, suspending the CNTs in the polymer solution and ensuring the formation of homogenous stable suspensions prior to electro-spinning are the frontline challenges. Therefore, we had initially focused on the dispersability of MWCNTs in the solution. Furthermore, solution conductivity and suspension viscosity were investigated, as they are among the dominant factors in the electro-spinning process. The Design of Experiment (DOE) approach was incorporated to identify and determine the significance of these process parameters in the production of uniform nanofibers. The existence of the MWCNTs in the composite fibers was demonstrated by TEM

images and Raman spectroscopy. Electrospun webs of uniform fibrous morphology were used to reinforce epoxy matrix. Lastly, the mechanical response and thermal stability of the polymer composite nanofiber-reinforced nanocomposites were investigated.

### **3.3.1 Polymer Solution Characteristics**

#### **a. The stability of polymer solution containing MWCNTs**

In the electro-spinning process, the characteristics of the initial solution determine the final composite fibrous structure and especially the diameter of the electrospun nanofibers. In order to determine the processing parameters for achieving stable and homogenous suspensions, a systematic study of DLS measurements was carried out. To monitor the system dynamics and the hydrodynamic radii distributions of a polymeric solution at 30 wt% concentration containing 1 wt% MWCNTs were determined at several time intervals: 1, 2, 4, and 24h. The hydrodynamic radii at the initial stage exhibited three sharp peaks around 100 nm, 300 nm and 1000 nm, whereas the z-average particle size was 410 nm. The consecutive experiments with a time interval of 1, 2, 4, and 24 h (See Figure 3.1) with the lack of mechanical driving forces revealed that agglomerates became stabilized based on the appropriate selection of polymer with styrene repeat unit and DMF as the solvent. Aromatic compounds, such as the benzene ring in our styrene are known to interact strongly with graphitic sidewalls of carbon nanotubes through effective  $\pi$ - $\pi$  stacking [62, 63]. These interactions are manifested in the dispersion of CNTs in aromatic solvents [64, 65], as well as in solutions of certain polymers [66-70]. The  $\pi$ -stacking interactions increase binding to CNTs, increasing as a consequence solubility of nanotubes in our polymer solution [71]. In addition, the z-average particle size remained smaller than 580 nm, even after 24 h, and no precipitation was observed in the electro-spinning solution. Increasing the MWCNTs concentration did not change the stabilization of the polymer. The largest hydrodynamic radii was still not higher than 1  $\mu$ m at 2% MWCNTs/ P(St-co-GMA) solution. The size of the CNTs bundles did not vary in the subsequent hours, due to stabilization effect of the benzene ring in the polymer structure. Furthermore, P(St-co-GMA) has an aromatic ring that would assist in the long term stabilization of

MWCNTs in polymer solution during nanofiber formation. In fact, completely opaque solutions that are stable over a long term were achieved.

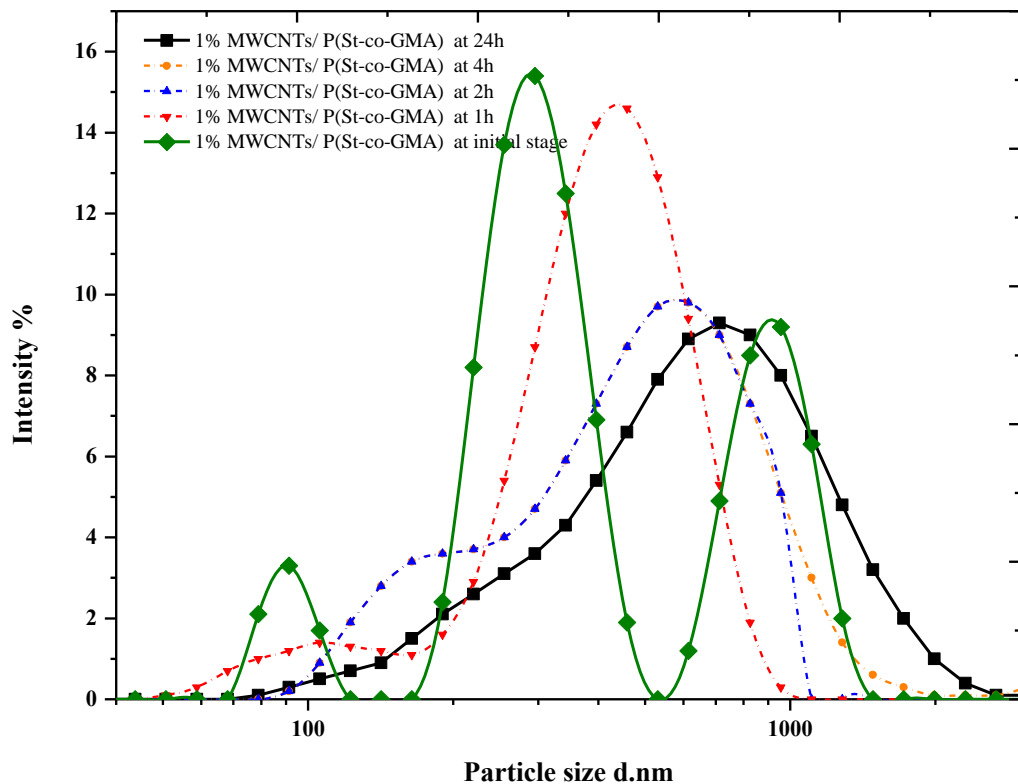


**Figure 3.1.** Hydrodynamic radii of the polymer solution at initial stage and after MWCNTs added. The times correspond to the delay after mixing: 1, 2, 4, and 24 h; the z-average of electro-spinning solutions at initial stage, 1, 2, 4, and 24h were 410, 505, 510, 520 and 580 nm, respectively.

### b. Suspension viscosity characteristics by MWCNTs

Several factors related to the suspension viscosity (such as polymer concentration, particle/filler concentration, and the rheological behavior of the fine particle system) influence electro-spinning process and the diameter of the fibers. Suspension viscosity should be examined, in order to discuss the flow behavior of solutions containing different amounts of MWCNTs under shear conditions, similar to those applied during the electro-spinning process. Furthermore, as Park *et al.* [72] pointed out, the resultant shear stresses increases as the applied DC electric field increases in electro-spinning. The measurements of shear viscosity in this research were conducted at different proportions of MWCNTs and neat P(St-co-GMA) in DMF solution. The results obtained show that viscosity decreases considerably with the addition of MWCNTs.

Rotational rheometer results in Figure 3.2 reveal that at a shear stress of 10 Pa, the shear viscosity of the neat polymer solution and the solution containing 1% MWCNTs were  $9.98 \times 10^{-2}$  Pa.s and  $10.50 \times 10^{-2}$  Pa.s, respectively. Exceptionally, at shear stress 1000 Pa, shear viscosity of the solutions dropped down to  $47.14 \times 10^{-3}$  Pa.s and  $8.76 \times 10^{-3}$  Pa.s. Moreover, the shear viscosity of the polymer solutions containing 1% and 2% MWCNTs was also measured under the same conditions, and shear thinning behavior was observed in both solutions. The resultant shear viscosity at 1000 Pa dropped, to  $8.76 \times 10^{-3}$  Pa.s and  $6.73 \times 10^{-3}$  Pa.s, correspondingly. The effect of suspension viscosity will be further discussed the fiber morphology in *Section 3.2.2*.

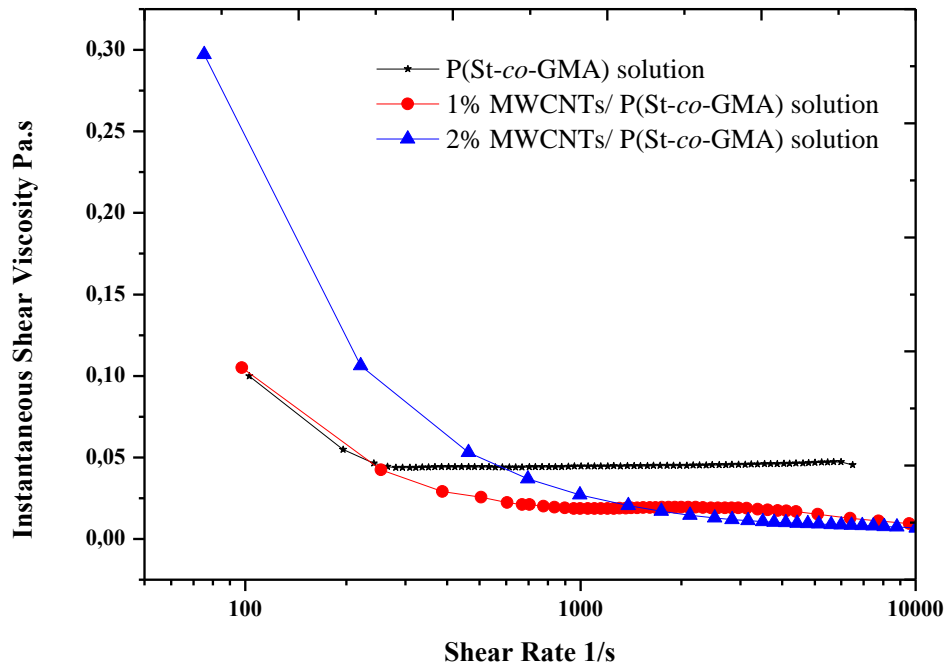


**Figure 3.2.** Suspension shear viscosity versus shear rate of neat polymer solutions and polymer solutions with 1% and 2% MWCNTs

### 3.3.2. Process Optimization for Composite Electrospun Nanofibers

#### a. Designing Experiments

The properties of the electrospun nanofiber formations, in particular the fiber diameter and morphology, depend on various parameters that can be divided into three groups: polymer solution properties (solution viscosity, solution concentration, polymer

molecular weight etc.); processing conditions (applied voltage, volume flow rate etc.), and ambient conditions (temperature, humidity etc.). In this study, processing and ambient conditions were held constant, in order to systematically investigate the effect of solution properties on the average fiber diameter. As we discussed in *Chapter 2*, without the addition of MWCNTs neat P(St-co-GMA) nanofibers were electrospun successfully at polymer concentrations of 30 wt% and higher. Here, polymer concentrations lower than 30 wt% and the addition of MWCNTs were considered, in order to investigate the possibility of spinning composite fibers with narrower fiber diameter. Three levels of polymer (25 wt%, 27.5 wt% and 30 wt %) and three levels of MWCNTs concentrations (1 wt%, 1.5 wt% and 2 wt% ) resulted in nine possible combinations for factor setting (Table 3.2). A schematic of the experimental design is shown in Figure 3.3. The fibers were first electrospun under the same processing conditions, morphologies and average diameters of the fibers were then investigated by SEM.

**Table 3.2.** Design of experiment (factors and levels)

Factor	Factor Level
Polymer Concentration (wt. %)	25, 27.5, 30
MWCNTs Concentration (wt. %)	1, 1.5, 2

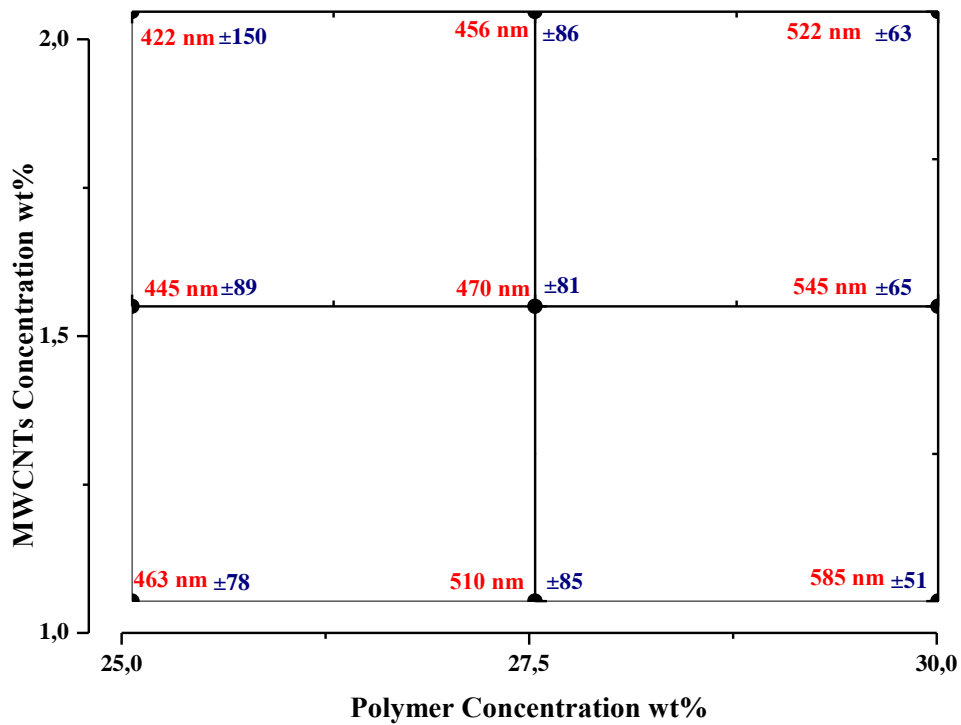


**Figure 3.3.** Experimental design. Red colored and blue colored values show the average fiber diameters (nm) and the standard deviation of fiber diameter of about 25 measurements.

### b. Morphology of Electrospun Fibers and Mats

Figure 3.4 shows the morphology of fibers obtained by varying the polymer and the MWCNTs concentration at 15 kV and a constant collector distance of 10 cm. The fiber diameter increased with polymer concentration, as anticipated, while fiber diameter decreases by tuning the MWCNT concentration. The effect on the fiber radius by MWCNTs is attributed to two factors: electrical conductivity [73, 74] and rheological changes in polymer solution (evidenced by reduced shear viscosity). It is widely known that the addition of MWCNTs increases the electrical conductivity of solutions (see Table 3.3). What is less acknowledged is that, depending on the surface and physical characteristic of particles, suspensions exhibit a range of rheological behavior that also influence the electro-spinning process. Pseudoplastic materials, such as some polymer solutions, show signs of shear thinning behavior which is an effect where viscosity decreases with increasing rate of shear stress. Moreover, shear thinning behavior would influence fiber diameter, as interpreted by Mazinani *et al.* [73] as the

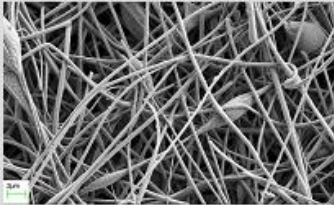
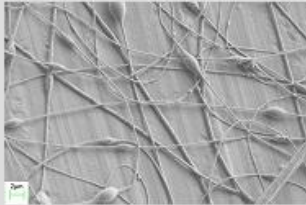
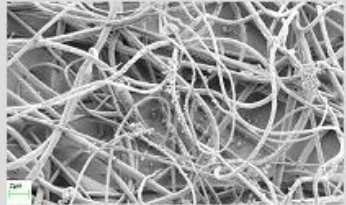
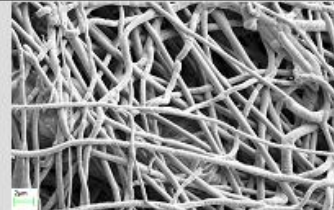
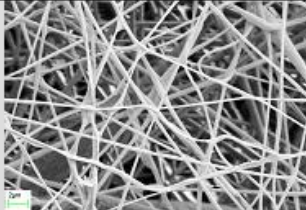
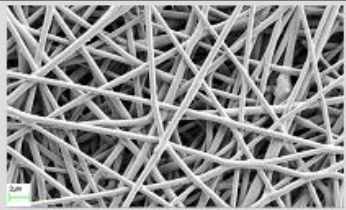
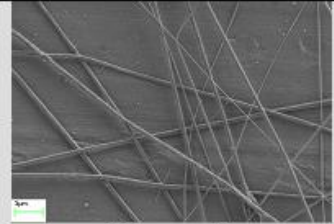
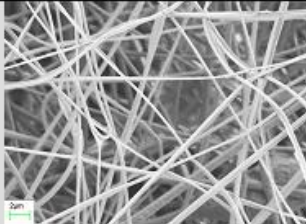
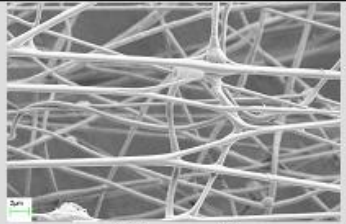
break-up of the polymer chains during sonication. However, sonication was not applied in our case. Therefore the reduced viscosity is attributed to the nanotube-polymer interaction under shear which lead to the thinner nanofibers by electro-spinning.

Using a polymer concentration of 25 wt% yielded thinner fibers (20% narrower compared to nanofibers at 30 wt%), but less homogeneous nanowebs due to bead like formations. Figure 3.5a suggests that the process resulted in spraying along with spinning, which prevented the formation of homogenous webs at 27.5 wt% concentrations. In addition, branched nanofibers are displayed in Figure 3.5b. These observations are also consistent with our published work [2]. Therefore, for further steps of hybrid material preparation, 30 wt% polymer concentrations were preferred for obtaining electrospun fiber and web homogeneity. It is worthy to note that increasing MWCNTs concentration also led to the formation of bead-like structures (Figure 3.5c) and a high variance in the fiber diameter. Figure 3.4 suggests that at higher polymer concentration, MWCNTs concentration has more impact on the average fiber diameter than at lower polymer concentration. To summarize, the fiber diameter tends to increase with polymer concentration and decrease with MWCNTs concentration.

**Table 3.3.** The conductivity ( $\mu\text{S}/\text{cm}$ ) of MWCNTs/ 30 wt % P(St-co-GMA) solutions at different MWCNTs concentrations.

	<i>MWCNTs Concentration</i>		
	1%	1.5%	2%
<i>The conductivity (<math>\mu\text{S}/\text{cm}</math>)</i>	20.9	27.5	39.1



MWCNTs		Concentration (wt %)		
Polymer Concentration (wt%)	1%	1.5%	2%	
25%				
	463 nm ± 78	445 nm ± 89	422 nm ± 150	
27.5%				
	510 nm ± 85	470 nm ± 81	456 nm ± 86	
30%				
	585 nm ± 51	545 nm ± 65	522 nm ± 63	

**Figure 3.4.** The morphology of fibers and average diameter with standard deviations at applied voltage 15kV by varying polymer and MWCNTs concentration. The scale bars for fibers are 2  $\mu$ m.

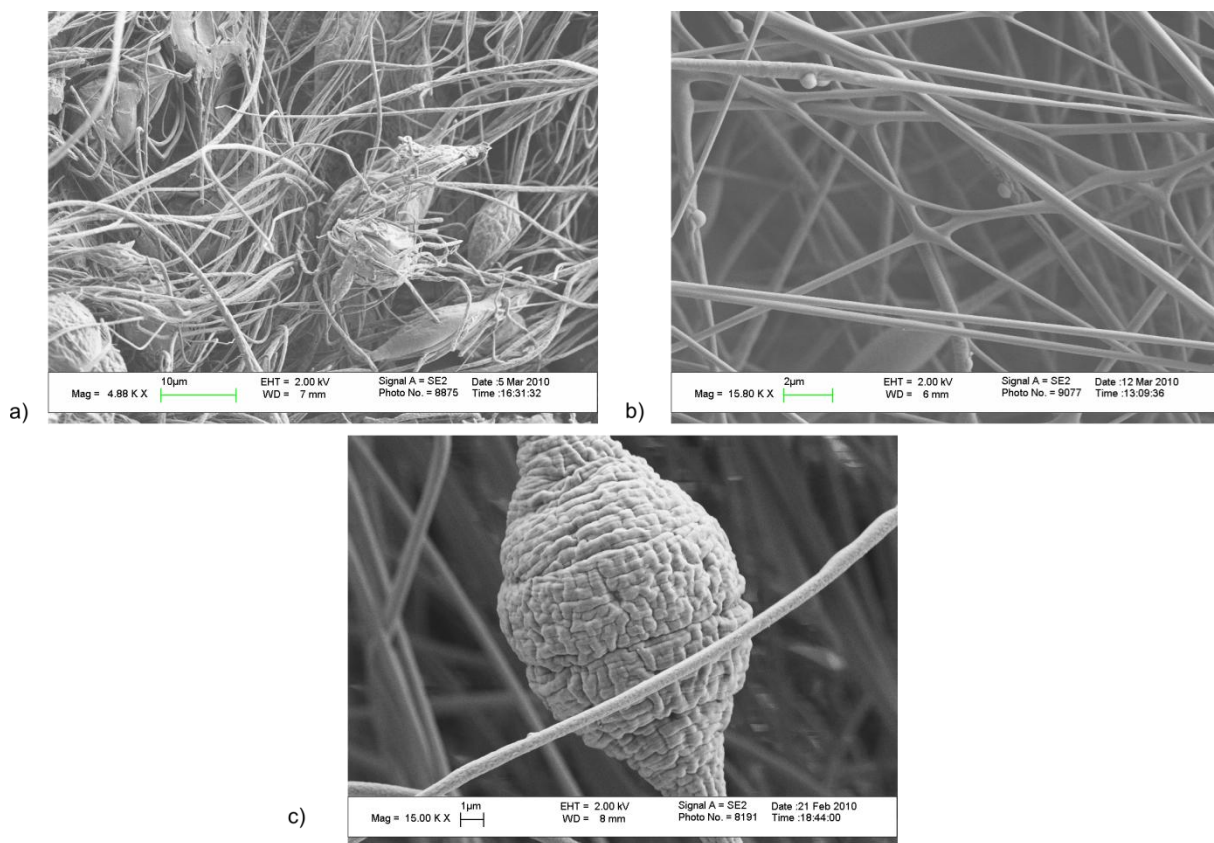


**Figure 3.5.** Morphology of nanofibers (a) at 25 wt % polymer and 2% MWCNT concentrations, partially sprayed inhomogeneous webs (b) branched nanofibers at 27.5 wt % (c) Magnified view of bead-like structures at 25 wt % polymer and 1 % MWCNTs concentration.

### 3.3.3. Detection of MWCNTs by TEM and Raman Spectroscopy

Raman spectra of non-woven mats were obtained using a red laser ( $\lambda = 830 \text{ nm}$ ) for determining the signature of the MWCNTs. Among the characteristic peaks of MWCNTs detected by Raman spectroscopy using a red laser (see Figure 3.6), two peaks could be distinguished located at  $1585 \text{ cm}^{-1}$  (G) and around  $1325 \text{ cm}^{-1}$  (D) [75-77]. P(St-co-GMA) nanofibers themselves exhibit sharp peak around  $1580 \text{ cm}^{-1}$ , which complicated determination of the MWCNT content. However, the peak at  $1585 \text{ cm}^{-1}$  for the composite nanofibers was a broader peak, when compared to the very narrow spectral feature of the neat polymeric nanofibers at this shift range, which is attributed to the existence of the MWCNTs. In addition, perturbations to the peaks are more distinctive for the 1% MWCNT and 2% MWCNT composite nanofibers, as the

increasing MWCNT concentration increased intensity and width of the peaks. Measurements from the surface of nanofibers demonstrated that it is possible to detect MWCNTs in such small amounts.

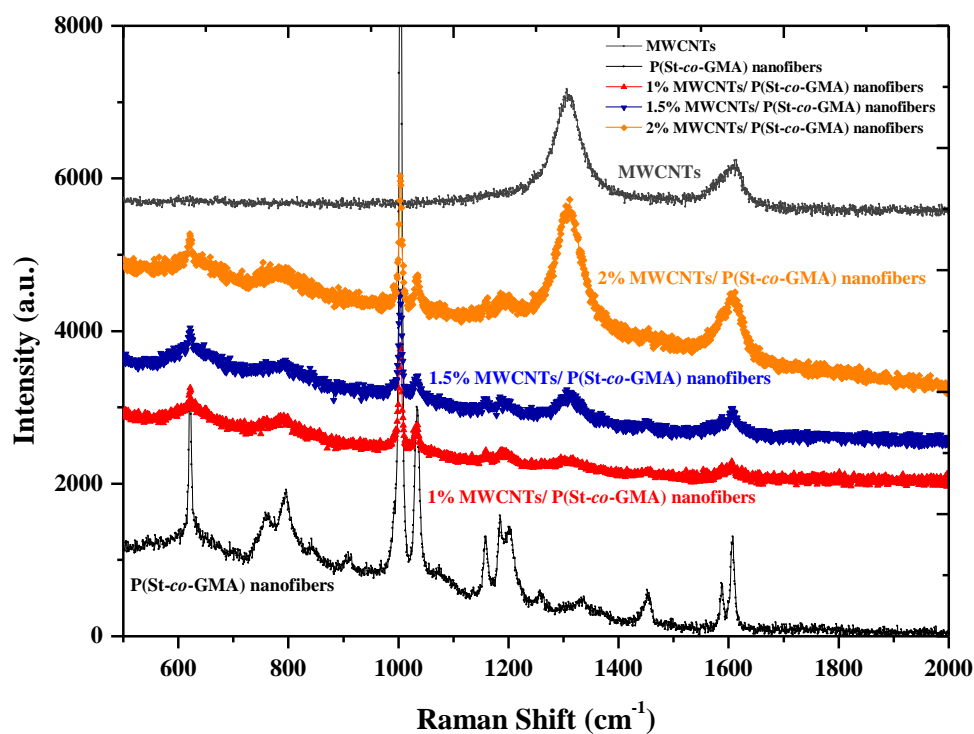


**Figure 3.6.** Raman Spectra of final nonwoven webs from red laser 830 nm (300 mW).

Evidence of the incorporation MWCNT was also obtained by TEM imaging and their appearance within the polymer fiber were studied by HRTEM. Transmission electron microscopy observation of 1.0 wt% MWCNT/P(St-co-GMA) fibrous webs produced by electro-spinning demonstrated that MWCNTs maintained their straight shape, even as they were positioned within the polymer fiber by electro-spinning under an electrical potential (See Figure 3.7).

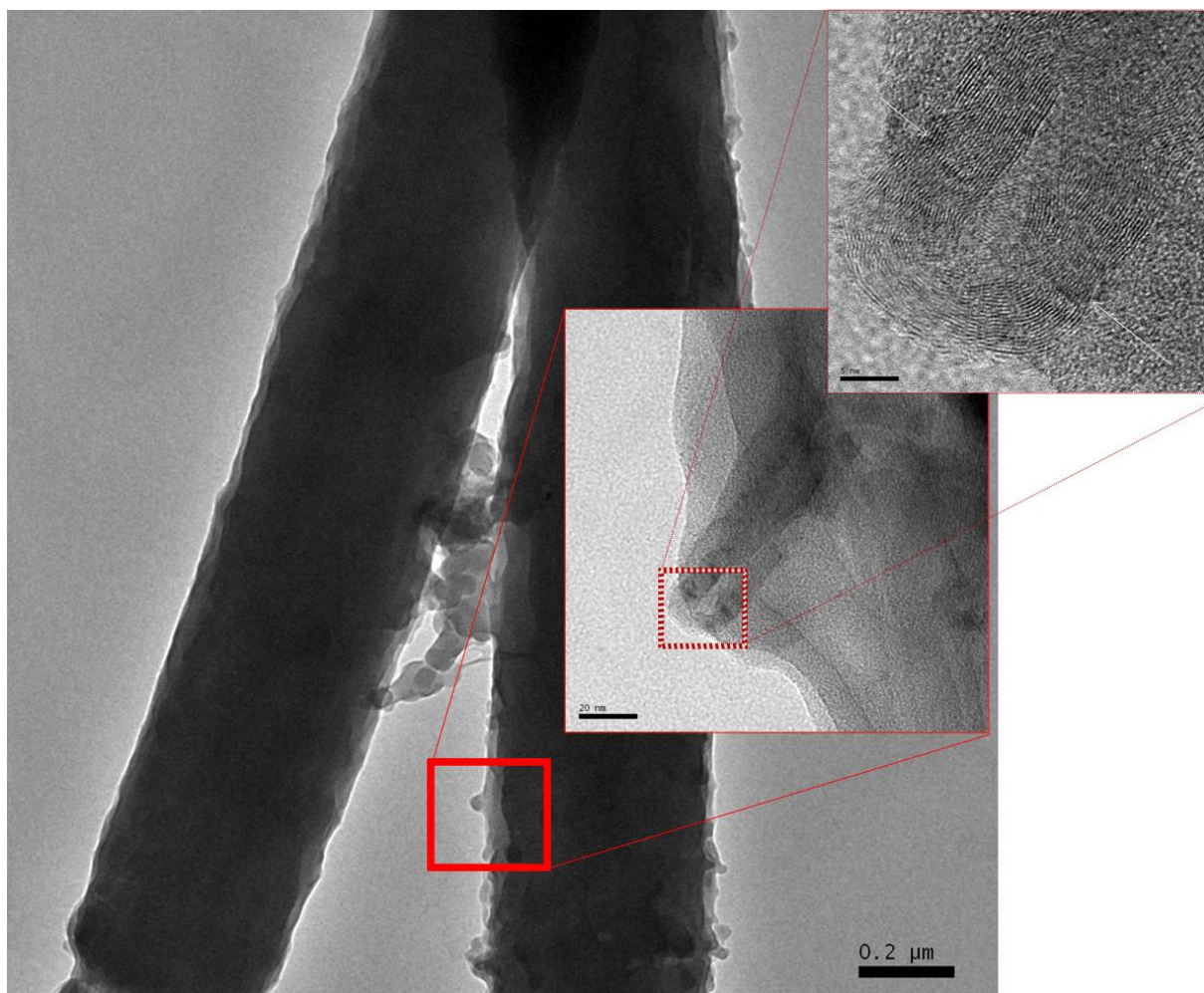


**Figure 3.7.** HRTEM of 1.0 wt% multiwalled carbon nanotubes in P(St-*co*-GMA).

### 3.3.4. Surface Wettability of Nanofibrous Webs

The elevations formed by the fibers themselves and the inter-fiber porosity contribute to a high degree of meso-scale roughness on the surface of electrospun nanowebs. Wettability of a rough surface was determined by the physical interaction between the solid surface and the particular liquid. Wenzel [78] and Cassie-Baxter [79] theories on the wettability of rough surfaces indicated that wetting was restrained due to roughness if the contact between the solid and liquid was not favored. For instance, water contact angle on the smooth P(St-*co*-GMA) surface prepared by dip coating was measured to be  $97.4 \pm 2.77^\circ$ , which indicated that the copolymer was hydrophobic. Accordingly, the rough nature of the electrospun surface increased this angle to



131.6±8.45°. On the other hand, wetting was induced due to the roughness if the cohesive forces between the solid and liquid phases dominated. The surface and chemical characteristics of functional MWCNTs/ P(St-co-GMA) nanoweb were essential for the wettability by epoxy resin in structural composites. In order to determine the wettability of the electrospun mat by the resin, epoxy droplets were deposited on the surface of MWCNTs/ P(St-co-GMA) mat as shown in Figure 3.9 and eventually, average contact angle was measured to be as low as 26.5 ± 6.10°. This result indicates that attractive forces between the copolymer and epoxy resin provided the liquid to spread over the rough surface and even penetrate through the micro pores without encountering a negative capillary pressure. Otherwise, high contact angles would be measured. Thus, the adhesion between epoxy resin and the nanofibrous MWCNTS/ P(St-co-GMA) nanoweb was high, which confirmed the physically reliable epoxy - hybrid material system.



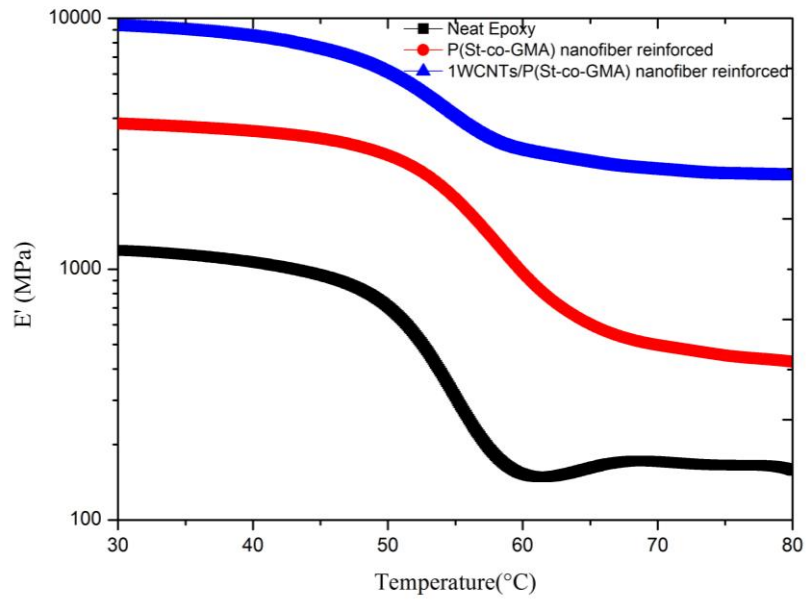
**Figure 3.9.** Frames taken during DSA measurements. Average contact angle is 26.5±6.10° for distilled epoxy droplet.

### **3.3.5 Mechanical Characterization of Composite Nanofiber-Reinforced Hybrid Materials**

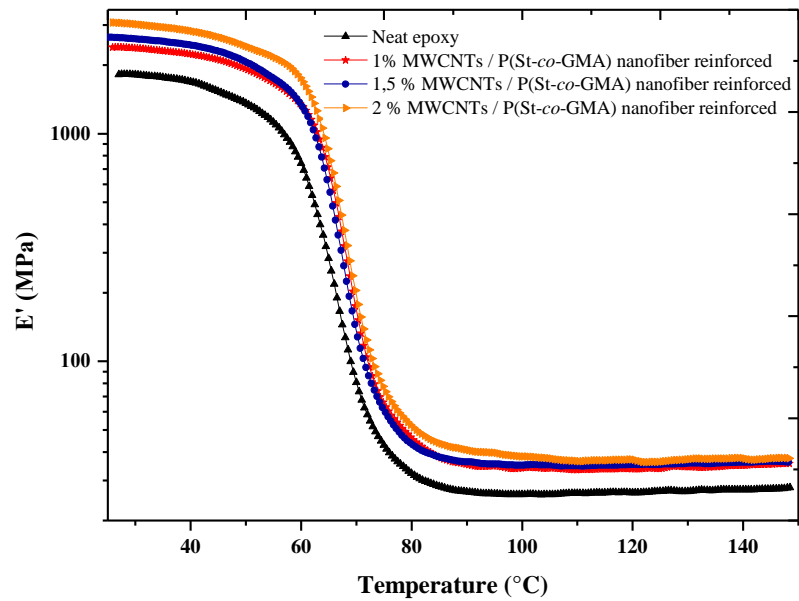
Stronger fiber-matrix interface has been explored before in reinforcing and toughening of the epoxy resin by the P(St-co-GMA) nanofibers. Here MWCNTs were introduced into the material system and the process as described in *Section 3.2.1*. MWCNTS/P(St-co-GMA) composite fibers, yet featuring epoxide rings in the surface chemistry for strengthening the interface, were embedded into epoxy resin. Thermo-mechanical and mechanical properties of the nanocomposite were investigated so that associated reinforcement due to the composite nanofibers electrospun at 30% wt

polymer concentration and various MWCNT fractions can be discussed. The results compared to earlier study in *Chapter 2*, indicated that incorporation of 2% weight fraction of 1% MWCNTs/P(St-co-GMA) composite nanofibers in epoxy was remarkably effective in increasing the storage modulus of the composite at 30 °C. There is more than a factor of 8 improvement with 1% MWCNTs/P(St-co-GMA) nanofiber reinforcement, in contrast with the neat epoxy. At 80 °C beyond the  $T_g$  of the composite material, the storage modulus reached a plateau, where the increase was around a factor of 18 compared to the neat epoxy (Figure 3.10a).

In addition, thermomechanical tests revealed that embedding a single layer of composite nanowebs resulting in 0.2% fiber weight fraction improve storage modulus of epoxy matrix nanocomposites as a function of MWCNTs concentration (Figure 3.10b). Specifically, MWCNTs/P(St-co-GMA) nanofibrous mats of 1%, 1.5% and 2% CNT weight fraction, respectively increased room temperature storage modulus of the nanocomposites by 32, 46, and 69% and by 27, 29, and 34 % at elevated temperature 150°C relative to that of the neat epoxy. The flexural strength ( $S_F$ ) and flexural modulus ( $E_Y$ ) of the neat resin and MWCNTs/P(St-co-GMA) nanofiber-reinforced hybrid materials were also measured at room temperature. ASTM- D790 3-point bending standard mechanical tests demonstrated that embedding a *single layer* of MWCNTs/P(St-co-GMA) nanofibrous mats of 1%, 1.5% and 2% CNT weight fraction, increased the flexural modulus of the epoxy matrix nanocomposites (at 0.2 % composite fiber weight fraction) ( $E_Y$ ) by 22, 23, and 23%, respectively, relative to that of the neat epoxy. Furthermore, the flexural strength ( $S_F$ ) increased by 15, 16, and 18%, respectively. To be a reference point, earlier studies, also discussed in *Chapter 2* revealed that  $S_F$  and  $E_Y$  when reinforced at 0.2% mass fraction of P(St-co-GMA) nanofiber (no CNT addition), increased by 6% [74] and 16% [2] correspondingly. These comparative results suggested that increase in the strength was dominated by the polymer fibrous web, and existence of CNT at the fractions tested appeared to be ineffective for further increase. The increase in stiffness on the other hand was substantially enhanced despite the low fraction of CNT introduced into the system.



a)



b)

**Figure 3.10.** (a) Storage modulus vs temperature measurements on nanofiber-reinforced materials (reinforcement with *ten layers* of 1% MWCNTs/P(St-co-GMA) and P(St-co-GMA)) webs and neat epoxy (b) Storage modulus vs temperature measurements on nanofiber reinforced hybrid materials (reinforcement with a *single layer* of MWCNTs/P(St-co-GMA) webs with 1, 1.5, and 2% MWCNTs weight fractions) and neat epoxy.

### 3.4. Concluding Remarks

In *this chapter*, the feasibility of fiber-matrix interface strengthening was investigated by reinforcing and toughening of the epoxy resin by embedding carbon nanotubes in polymer nanofibers and by modifying the composite fiber surface chemistry to include epoxide rings. Specifically, MWCNTs/P(St-co-GMA) composite nanofibers at three different nanotube weight fractions were electrospun in this work for the first time. Rheological properties and thermodynamic stabilization of MWCNTs in P(St-co-GMA)-DMF polymer solution were demonstrated. The MWCNT fraction was found correlated with shear thinning effect and the corresponding drop in the polymer viscosity resulted in lower fiber diameter. It was also shown that electrospun fiber diameter can be reduced by directly lowering polymer concentration at several MWCNTs fraction, but at the cost of the homogeneity and uniformity of the fiber formation within the electrospun mats. A polymer concentration of 30% was further studied, resulting in narrowing of the fiber diameter from an average 630 to 460 nm, as MWCNT weight fraction (1, 1.5 and 2%) was increased. These electrospun MWCNTs/P(St-co-GMA) composite nanofibers were then embedded into epoxy resin for exploring their reinforcing abilities. The significant increase was observed in the mechanical response up to >20% in flexural modulus compared to neat epoxy despite a very low composite fiber weight fraction (at about 0.2% by a single layer fibrous mat). The increase is attributed to the combined effect of the two factors: the strength of well dispersed MWCNTs in the structure and the modified surface chemistry of the electrospun fibers leading to bonding across the cross-linked polymer matrix-nanofiber interface. In fact, an increase in the flexural strength by nearly 15%, due to composite nanofibers was also noted. However, the absence of perceptible variation by various fractions of the MWCNT suggested that the strength increase was primarily due to the existence of cross-linked polymer nanofiber and interface reinforcement.



## CHAPTER 4

### STRUCTURAL COMPOSITES HYBRIDIZED WITH EPOXY COMPATIBLE COMPOSITE NANOFIBROUS INTERLAYERS

#### 4.1. Background

Intra-and inter-laminar resistance to failure in laminated composite materials has been an active and constantly growing research field. Matrix toughening and interlayer toughening have emerged to increase delamination resistance [80]. Kim and Reneker [22] introduced an innovative idea and showed the ability of electrospun nanofibers as potential bulk toughening elements. In line with Reneker's work, Dzenis *et al.* [8] explored the use of electrospun nanofibers as interlayer toughening elements within the traditional laminated composites. Dzenis observed that entangled nanofibers improved interlaminar fracture resistance much like the hooks and loops in Velcro and also played a part in crack deflection, nanofiber pull-out, plastic deformation, and crack bridging [8]. This pioneering idea was applied to several composite systems and studied under various testing conditions [81-86]. In this chapter, it is intended to contribute on the experimental demonstration and data generation of the nanofiber reinforced interlayers in laminated composites. In support of the effective use of electrospun nanofibers in structural composites, *Chapter 2&3* introduce the concept of tailoring or designing the chemistry of electrospun fiber and their interface with the polymer matrix. We emphasized earlier that P(St-co-GMA) is a promising base polymer for nanofiber production due to its chemical compatibility with epoxy systems in composite applications. It is our interpretation in collaborative work of Bilge K. and Ozden-Yenigun E. *et al.* [4] that integration of nanocomposites, nanofibrous filler

forms in particular, into conventional structural composites calls for both further data generation and multi-scale modeling or framework for accurate mechanical/structural behavior predictions.

We initially aim to show the potential of electrospun P(St-co-GMA) with/without MWCNTs based nanofibers as interlayers in conventional carbon fiber reinforced epoxy laminates. Given the choice of nanofiber chemistry is in favor of nanofiber-matrix compatibility and complete epoxy wettability, reinforcing abilities of the nanofibrous interlayers against transverse matrix cracking and delamination were explored. The overall flexural performance increases through the incorporation of nanofibrous interlayers as reported. Resistance against delamination was measured in mode II by end notched flexure (ENF) tests whereas transverse matrix cracking resistance was primarily characterized by transverse Charpy impact tests and transversial tension tests. The effect of MWCNT presence in the fibrous structure was further evaluated through parallel testing of P(St-co-GMA) interlayered laminates. More detailed information about the procedure is accessible through MSc Thesis of Bilge *et al.* [87] and our published work in *Composite Science and Technology* [4].

## **4.2. Experimental Procedure**

### **4.2.1. Electro-spinning Process and Laminate Manufacturing**

Synthesis of P(St-co-GMA) copolymer was reported in *Section 2.2.1*. The polymer solution was electrospun directly onto carbon/epoxy prepreg layers. Consequently, a thin homogenous layer of nanofibers, was electrospun on the prepreg surface forming the interlayer with an additional weight as low as 0.2% of the prepreg ply weight. Electro-spinning conditions were set as described in *Section 3.2.1.a*. Note that whether being subject to electro-spin or not, out-of-the freezer time and conditions of the prepreg plies were kept consistent. After stacking the plies for intended laminates, each stack was put on a metallic tooling plate along with a release film and peel ply. Another sheet of peel ply was then laid on the pile of plies followed by a nonwoven breather layer. Next, the whole lay-up was vacuum bagged and kept under vacuum during the cure cycle. The cure temperature was primarily selected in accordance with the glass

transition temperature of P(St-co-GMA) copolymer fibers, as stated in *Chapter 2*. Prepreg stacks were heated up 100 °C at a rate of 0.85 °C/min, and hold time was 48 h. Through screening flexural tests, this prolonged cure cycle resulted in very close flexural performance on unidirectional (UD) specimens compared to typical cure cycle at 132°C for four hours: flexural modulus  $45.7 \pm 0.8$  vs  $46.5 \pm 1.6$  GPa and flexural strength  $875 \pm 15$  vs  $867 \pm 19$  MPa.

#### 4.2.2. Mechanical Testing

Mechanical tests were performed using of Zwick Roell Z100 Universal Testing Machine and CEAST Resil Impactor machine. Loading rates and machine accessories were set up in accordance with the testing types namely, unnotched Charpy impact, three point bending, end notched flexure and transversal tension tests. Flexural strength and modulus of interlayered and non-interlayered, (0/0/0) and (90/0/90) laminates were calculated via three point bending tests. For interlayered laminates, two interlayers on the interlaminar planes separated by a carbon/epoxy ply were added. Test configurations and preparation of the specimens were done according to ASTM D790 testing standards. Mode II critical strain energy release rate ( $G_{IIc}$ ) of the composite laminates was investigated by ENF tests. (0)<sub>4</sub> uni-directional laminates containing mid-surface delamination were tested under three point bending load configuration. A non-adherent, 30 µm thick film layer was inserted to create the initial delamination during consolidation of the laminates. Unlike the 3-point bending tests the interlayer was inserted only at the midplane. Tests were conducted with a constant displacement rate of 1 mm/min and  $G_{IIc}$  values were calculated using direct beam theory [88]. Transverse tensile tests were performed in accordance with ASTM D3039 test standards. Laminates stacked as (90)<sub>4</sub> having interlayers between the adjacent plies were used. Tests were conducted with a constant displacement rate of 1 mm/min. Maximum stress at failure was measured to determine the tensile strength of the tested laminates. Charpy impact tests were performed in accordance with the ASTM D 6110 testing standards. Specimens of (0)<sub>4</sub> laminates were subjected to transversal impact loading from the longitudinal edge. Interlayered specimens contained 3 layers of interply reinforcement.

An impact hammer of 4J energy capacity was used with an initial release angle of 150°. The amount of energy absorbed upon transverse impact was recorded.

#### **4.2.3. Surface and Cross-sectional Analysis**

Cross section and fracture surface analysis of the composite laminates were carried out with a LEO Supra VP35 field emission scanning electron microscope after sputter deposition of a thin conductive carbon coating onto the samples. Contact angle measurements of the epoxy resin on the electrospun fiber mats were performed using the same method described in *Chapter 3*. 5 mg droplets of resin/hardener mixture were put on the electrospun P(St-co-GMA) fibrous mat surface to investigate the epoxy wetting.

### **4.3. Results and Discussion**

#### **4.3.1. Structural Compatibility of P(St-co-GMA)/MWCNTs Interlayer**

We demonstrated in *Section 3.3.3* that MWCNTs were efficiently placed in the polymeric nanofibers as supplementary pin-like reinforcing elements. P(St-co-GMA)/MWCNTs nanofibers electrospun onto the prepreg surfaces at room temperature (Figure 4.1a and b). When the electrospun mat was heated up to 100 °C, the non-woven fibrous morphology was transformed into a net-like structure composed of fibers connected at micron scale bead-like nodal points (Figure 4.1c and d). This change in the microstructure suggests the presence of a good interaction between fibrous interlayers and matrix phase at the laminate curing temperature. The matrix and nanofiber interaction was also observable macroscopically. Figure 4.2 shows photograph of the electrospun layer-prepreg system kept at curing temperature 100°C (left hand side) and pristine samples at room temperature (right hand side) for comparison. It was quite visible that when the prepreg with the electrospun fibrous layer coat was heated, the epoxy matrix penetrated into the fibrous layer and wetting of the layer was completed even standing free with no vacuum bagging pressure (Figure

4.2b). Recall that the zoomed-in view of the surface of unheated laminate in Figure 4.2b appeared as shown in Figure 4.1a. However, when the temperature was increased, those layers of the majority of the nanofibers were no longer visible due to progressive self-wetting (Figure 4.2c and d). More formal investigation of the wettability was performed via contact angle measurements with epoxy/hardener mixture on the surface of the electrospun mat earlier in *Section 3.3.4*. We revealed the attractive forces between copolymer and epoxy system systematically.

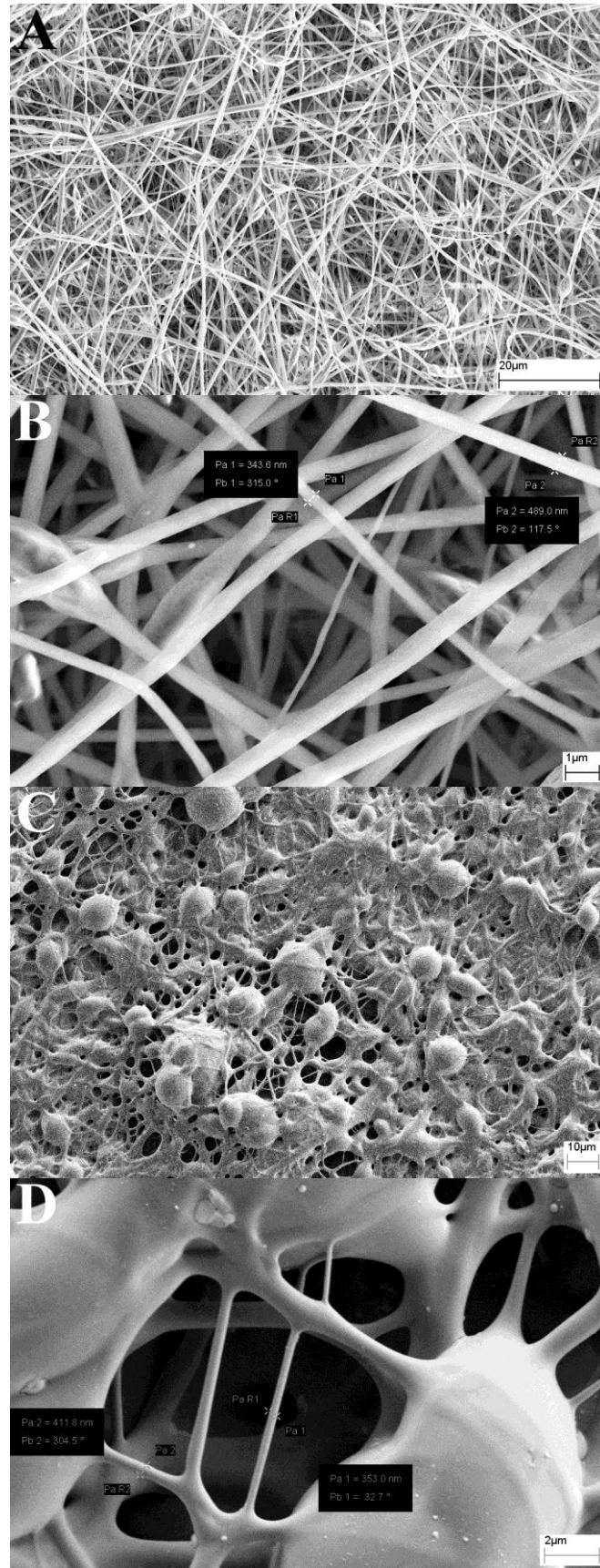


**Figure 4.1.** Nanofiber morphologies on the prepreg surfaces: (a) and (b) at room temperature and (c) and (d) at 100°C.

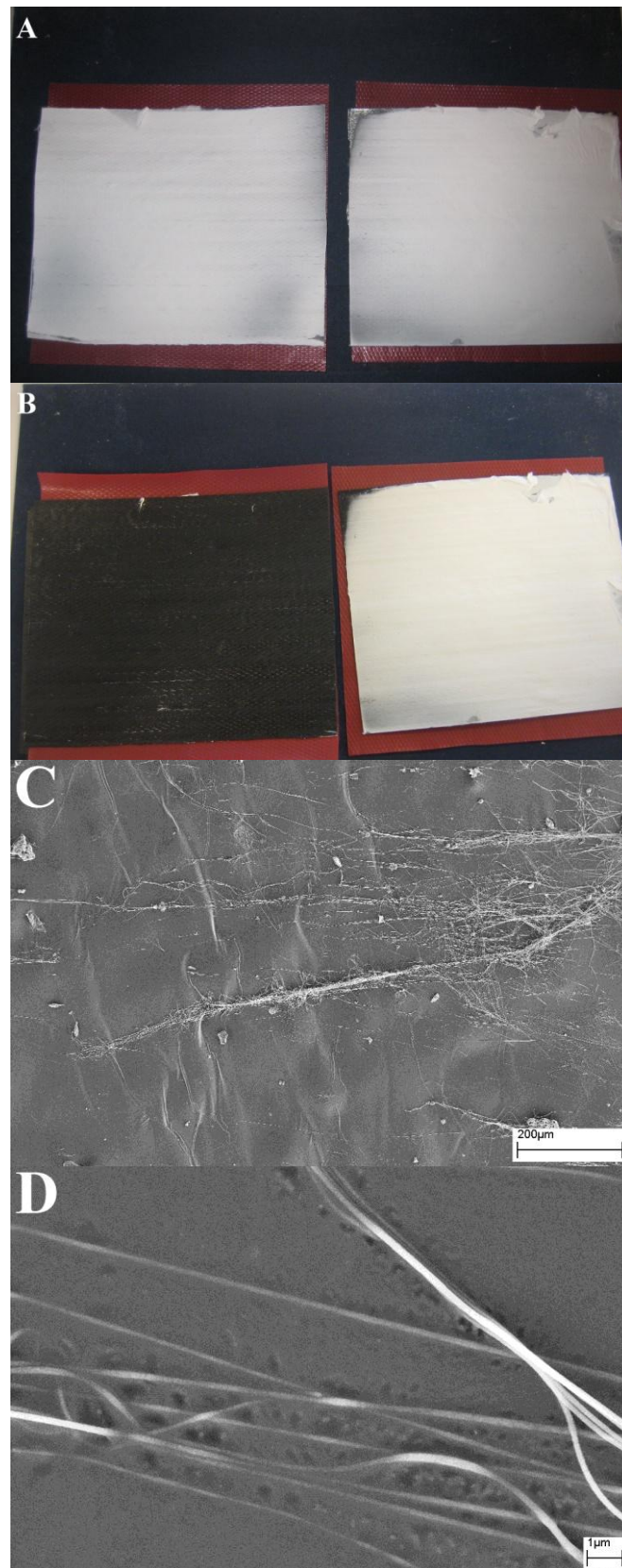


**Figure 4.2.** Nanofibrous mat over the prepreg layers (a) Just after electro- spinning (b) 30 minutes after at 100°C (c) and (d) Zoomed in view for fiber/epoxy interaction at 100°C.

#### 4.3.2. Flexural Performance by Three-Point Bending Tests

Comparison of three point bending tests on laminates with and without fibrous interlayers showed that their addition led to increase in both flexural strength and modulus of the samples. The nanofibrous interlayers (denoted by I) within the laminates (0/I/0/I/0) resulted in 11% and 17% increase in the flexural strength ( $\sigma_{\text{flex}}$ ) and flexural modulus ( $E_{\text{flex}}$ ), respectively (2<sup>nd</sup> and 3<sup>rd</sup> columns of Table 4.1). Introduction of nanotubes by 1% weight to the copolymer fibers led to a further improvement adding up to 16% and 25% increase in the corresponding values compared to results without nanocomposite interlayers incorporated. Comparing (90/0/90) vs (90/I/0/I/90) laminates, P(St-co-GMA) nanofibrous interlayers increased both the flexural strength and modulus of the samples by 17%. The increase in these values were 21% and 29% with P(St-co-GMA)/MWCNTs interlayers.

Post-failure SEM analyses on cross section of the specimens revealed that the lamination sequence was a factor in the fracture mode. Two distinct active failure mechanisms, transverse matrix cracking and/or delamination, were observed in (0/0/0) laminates. Co-existence of the two failure mechanisms on the samples is attributed to the inability of the three point bending test to create pure shear conditions. An example is shown in the SEM image of a (0/0) interface represented in Figure 4.3a where the two corresponding mechanisms were indicated with arrows (1: transverse matrix cracking and 2: delamination). Oblique intra-ply damage initiated at the end of delamination growth occurred due to the presence of high stress regions at the contact of the loading tip. The flexural strength and modulus increase reported by the three-point bending tests characterized both delamination resistance and matrix toughening introduced by the addition of the interlayer. This double effect of the interlayer was also studied and introduced by Sih *et al.* [85].

With (90/0/90) lamination sequence, fracture mechanism was driven by 90° plies. The presence of 90° plies at the outer surface ensured the arising of interlaminar stresses at 90/0 interface due to the stiffness mismatch. In addition the inherent weak links of 90° plies to tensile loads triggered a matrix crack induced failure on the bottom ply during bending loading (Figure 4.3b). Figure 4.4 shows the representative flexural force–displacement curves of specimens with and without nanocomposite interlayers.



The initial load drop (encircled in Figure 4.4) corresponds to the first ply failure due to the critical matrix cracking on the bottom 90° ply subjected to tension. Note that the local matrix failure did not cause the ultimate failure. Instead a stable crack growth characterized by the load drops in Figure 4.4 was observed and the final fracture occurred when 90 (failed)/0 interface progressed to delamination. Hence the overall flexural performance was governed by two major failure mechanisms. The increased resistance against initial matrix cracking may be noted by comparing the first ply failure loads whereas the delamination resistance of laminates may be compared by the ultimate load values. It is clearly visible from Figure 4.4 that the interlayer addition worked well for both mechanisms as it was suggested for (0/0/0) laminates.

**Table 4.1.** Mechanical Test Results.

Specimen Layup	<sup>1</sup> $\sigma_{flex}$ (MPa)	<sup>1</sup> $E_{flex}$ (GPa)	<sup>2</sup> $G_{IIc}$ (kJ/m <sup>2</sup> )	<sup>3</sup> Energy Absorbed (kJ)	<sup>4</sup> $\sigma_{2ult}$ (MPa)
(0/0/0)	875±16	45.7±0.8	-	-	-
(0/ <sup>a</sup> I/0/ <sup>a</sup> I/0)	965±17	53.5±0.9	-	-	-
(0/ <sup>b</sup> I/0/ <sup>b</sup> I/0)	1002±14	57.3±0.4	-	-	-
(90/0/90)	243±6	4.9±0.2	-	-	-
(90/ <sup>a</sup> I/0/ <sup>a</sup> I/90)	282±9	6±0.1	-	-	-
(90/ <sup>b</sup> I/0/ <sup>b</sup> I/90)	296±6	6.4±0.1	-	-	-
(0/0/0/0)	-	-	0.95±0.03	1.72±0.05	26.5±0.7
(0/0/ <sup>a</sup> I/0/0)	-	-	1.47±0.04	-	-
(0/0/ <sup>b</sup> I/0/0)	-	-	1.60 ±0.10	-	-
(0/ <sup>a</sup> I/0/ <sup>a</sup> I/0/ <sup>a</sup> I/0)	-	-	-	1.86±0.10	31.2±0.6
(0/ <sup>b</sup> I/0/ <sup>b</sup> I/0/ <sup>b</sup> I/0)	-	-	-	2.13±0.20	33.6±0.7

<sup>a</sup> P(St-co-GMA) interlayers

<sup>b</sup> P(St-co-GMA)/MWCNTs interlayers

<sup>1</sup> Three point bending.

<sup>2</sup> End notched flexure.

<sup>3</sup> Charpy impact.

<sup>4</sup> Transverse tensile.

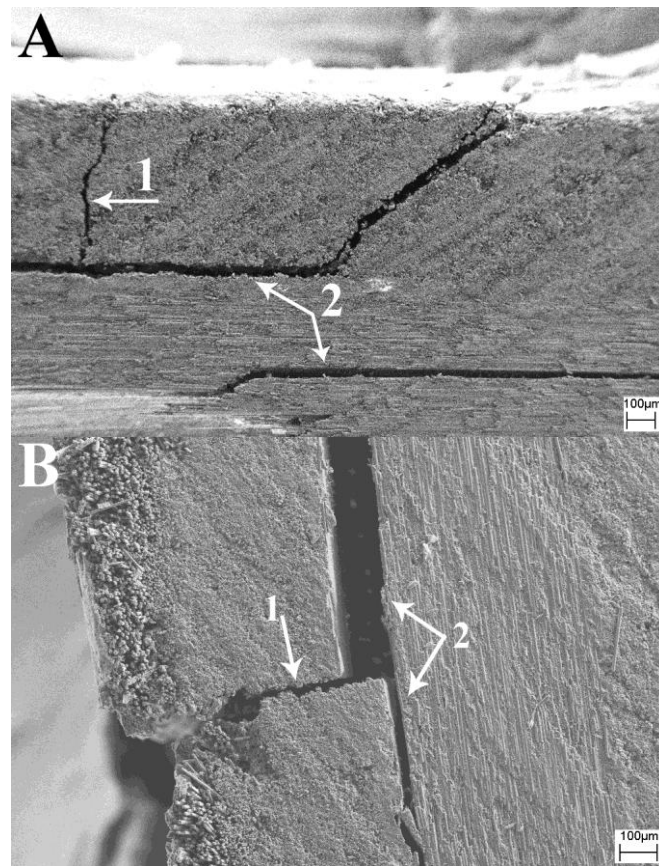


**Figure 4.3.** Cross-sectional view of fractured three point specimens. (a) (0/0/0) and (b) (90/0/90).

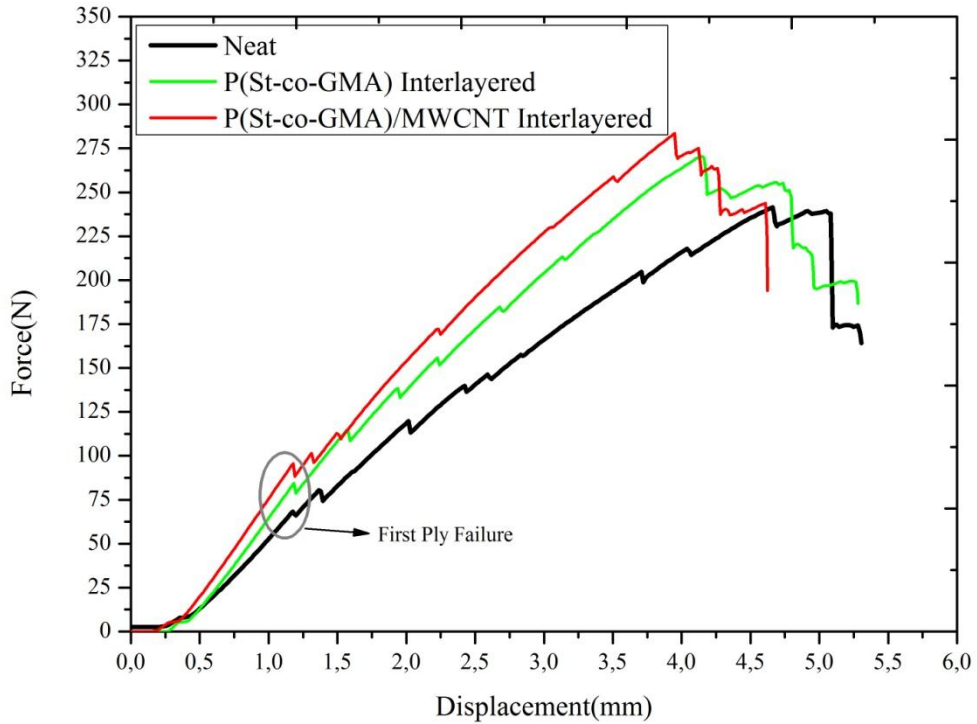


**Figure 4.4.** Representative force-displacement test curves for (90/0/90) laminates.

#### 4.3.3. Mode II Strain Energy Release Rate by ENF Tests

P(St-co-GMA) interlayer presence at the pre-crack tip increased  $G_{IIc}$  by 55% (4<sup>th</sup> column Table 4.1). Further increase up to 70% in  $G_{IIc}$  by P(St-co-GMA)/MWCNTs interlayers suggests that the toughening is also correlated with the incorporation of the MWCNTs on electrospun fiber surfaces. Failure of ENF specimens was observed as dominated by unstable crack growth parallel to the interlaminar plane with a sudden load drop. Formation of an unstable crack growth can be considered as an inherent characteristic in the testing of UD laminates under ENF test configurations with constant displacement rate [89]. Further analysis of the fracture surfaces also suggested that the increase observed in  $G_{IIc}$  was directly associated with the active role of interlayers on the fracture resistance. Common hackle patterns typically due to the micro-crack coalescence [90] all along the crack pathway are clearly visible on specimens without nanocomposite interlayers (Figure 4.5a) whereas the hackle patterns for the interlayered specimens were either locally altered and replaced by a more complex structure or enlarged in size (Figure 4.5b).

A different fracture mode was noted as the capillary-like damage marks indicated in Figure 4.5c. These damage marks were observed both in the areas consisting of epoxy-interlayer complex (left and right arrows) and around carbon fibers (center arrow) that is surrounded by epoxy-interlayer complex (Figure 4.5d). Close examination of the fracture pattern seen in Figure 4.5d revealed the presence of micro-crack formation through the interlayer–epoxy complex. This observation can be further supported by the cut-like damage marks inside the interlayer–epoxy complex, for which a zoomed-in image is shown in Figure 4.5e. Furthermore, the epoxy matrix and interlayers were not separated with a distinct interface, which was consistent with the structure shown in Figure 4.1c (image taken on ply).

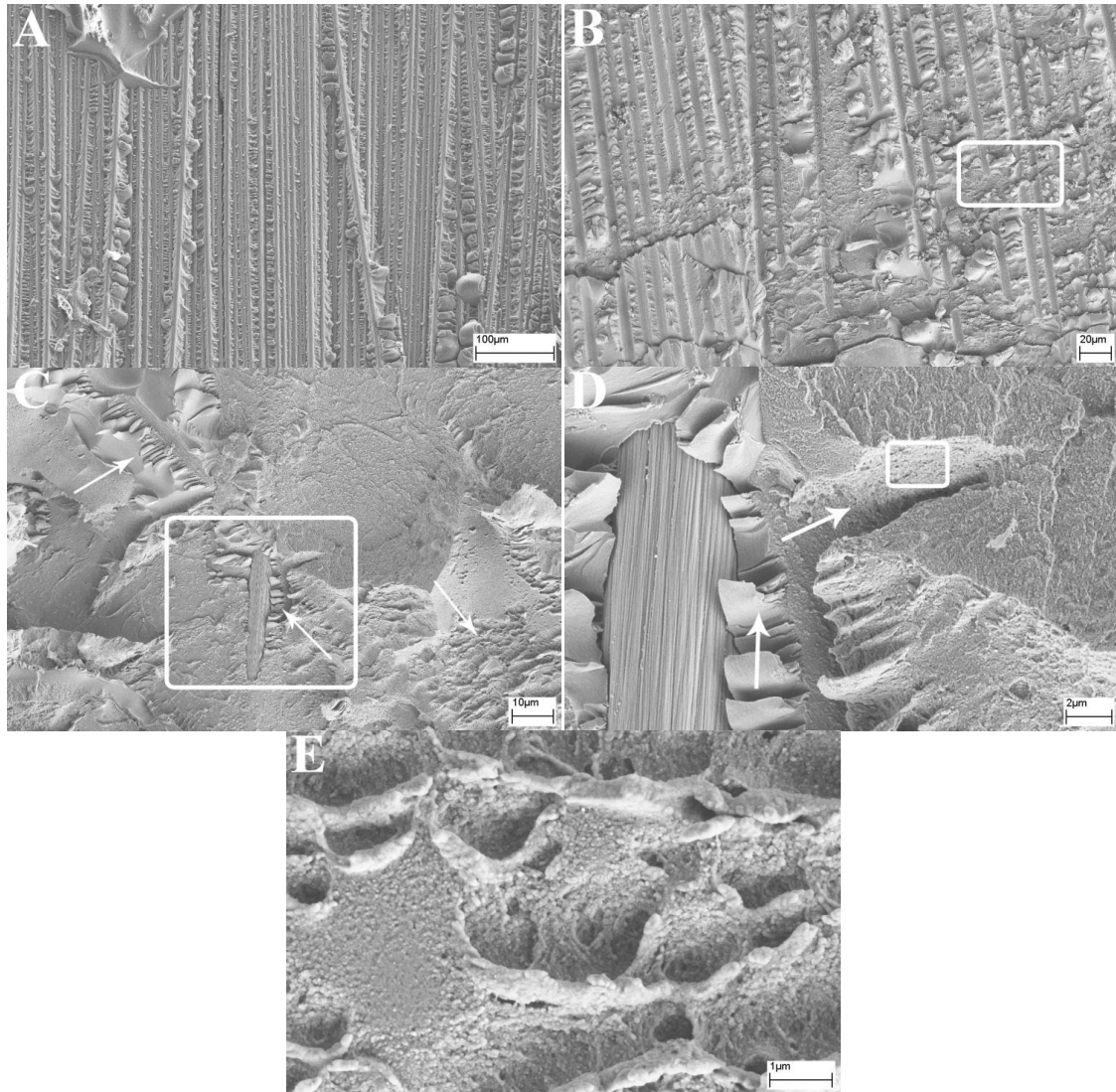


**Figure 4.5.** Fracture surfaces of (a) neat epoxy ply-to-ply interface and (b) P(St-co-GMA)/MWCNT interlayered interface (c) Zoomed in view for encircled area in 4.5b Arrows indicate the distinguishable damage marks (d) Zoomed in view for encircled area in 4.5c, arrows indicate two distinct failure regions (carbon fiber interface and through interlayer/epoxy complex) (e) Zoomed in view for encircled area in 4.5d Damage marks on interlayer/epoxy complex.

#### 4.3.4. Un-notched Charpy Impact Test Results

The effect of interlayers against the transverse micro-cracking as reported by preliminary three point bending results were further explored by Charpy impact tests. Unidirectional composite specimens were subjected to transversal impact (impact head to hit against the specimen longitudinal side wall rather than its surface) in order to create a failure initiated by sudden matrix cracking. An average increase up to 20% was

recorded with the interlayered specimens. Moreover, in consistence with the results reported in previous sections, the presence of MWCNTs on the fiber surfaces played a similar role in the overall performance of the laminates under impact loading conditions (5<sup>th</sup> column in Table 4.1).

#### 4.3.5. Transverse Tensile Test Results

Transverse tensile tests of the uni-directional laminates offer an easy way to test for the effect of interlayers on the matrix dominated characteristics. Integration of P(*St-co-GMA*) and P(*St-co-GMA*)/MWCNTs interlayers on each ply resulted in 17% and 27% increase, respectively in transverse tensile strength (6<sup>th</sup> column of Table 4.1), with no weight penalty. These results correlate well with the previous Charpy impact tests where toughening by nanocomposite interlayers was associated with the increase in absorbed impact energy. Ultimate fracture of the UD transverse tension specimens was in the matrix cracking mode as expected. The cross sectional analysis of failed specimens further revealed the difference in ply-to-ply resin structure at the interlaminar plane which was differentiated by the space between two subsequent carbon fibers as indicated in Figure 4.6.

Figure 4.6a corresponds to the cross-sectional view of a laminate of neat epoxy interlayer where the damage marks occurred due to the resin fracture are clearly visible and the between-ply and in-ply resin fracture patterns are consistent. On the contrary, the resin morphology between the plies (ply-to-ply interface) and inside the plies were different on the cross-sectional fracture surface of the P(*St-co-GMA*)/MWCNTs interlayered specimens, as can be seen in Figure 4.6b.

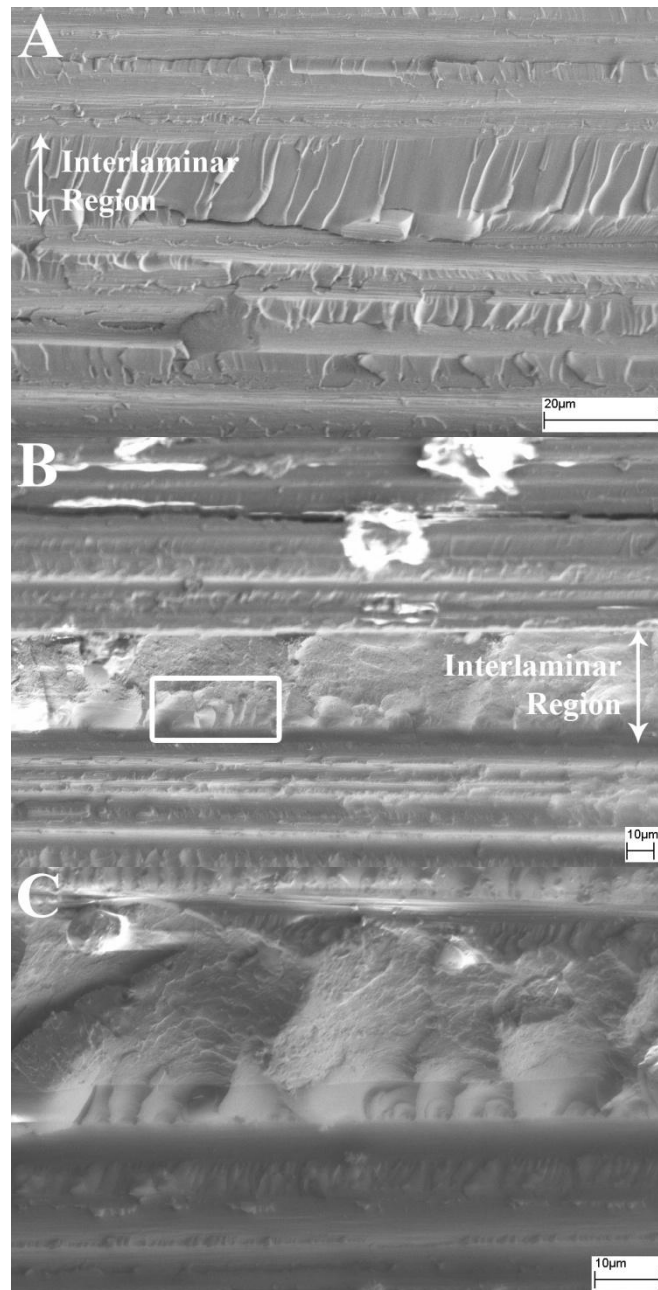


**Figure 4.6.** Cross-sectional view of a fractured transverse tensile UD test specimen (a) neat epoxy ply-to-ply interface and (b) P(St-co-GMA)/MWCNTs interlayered (c) Zoomed in view of encircled area in 4.6.

#### 4.4. Concluding Remarks

Nanofibrous P(St-co-GMA) and P(St-co-GMA)/MWCNTs interlayers were electrospun on uncured carbon/epoxy prepreg surfaces. Three point bending test results showed significant amount of increase in both flexural strength and flexural modulus up to 25% and 29%, respectively. The mode II delamination resistance was increased up to 70%, and noticeable changes in the fracture modes were observed when nanocomposite interlayers were incorporated into the laminates. The resistance against transverse matrix cracking was tested under impact and tension loads. Interlayered Charpy impact specimens absorbed 20% more energy than the non-interlayered ones. Transverse tensile strength of the interlayered UD specimens was about 27% higher than the non-interlayered specimens. Cross sectional fracture surface analysis suggested compatibility of interlayers with the surrounding matrix, which we attributed as the reason for resistance against matrix cracking. Chemical characteristics with the choice of P(St-co-GMA) also enable the incorporation of MWCNTs during electro-spinning, which eventually further increased the mechanical performance of the interlayered laminates with a very low weight penalty (at about 0.2% by a single fibrous layer).



## CHAPTER 5

### TRACING THE SUPERIOR THERMO-MECHANICAL PROPERTIES IN NANOCOMPOSITES OF CROSS-LINKED FILLERS AND INTERFACES: MOLECULAR POINT OF VIEW

#### 5.1. Background

*Chapter 5* presents two different numerical approaches; specifically to investigate the mechanical behavior of epoxy matrix nanocomposite. Reinforcing materials of interest are surface reactive P(St-co-GMA) nanofibers and carbon nanotubes. Effect of the nanofiller chemistry on mechanical behavior of thermoset polymer matrix nanocomposites is explored in *Chapter 5*. In *Section 5.2.1*, molecular dynamics (MD) simulations are employed to address the differences in the temperature dependence of the bulk, shear and Young's modulus when the characteristics of fiber-epoxy interface in the nanocomposites are modified. In *Section 5.2.2*, a multi-scale/fidelity approach is implemented not only to understand reinforcing function, but also cross-linking mechanism where the degree of cross-linking is the main element in cross-linked systems.

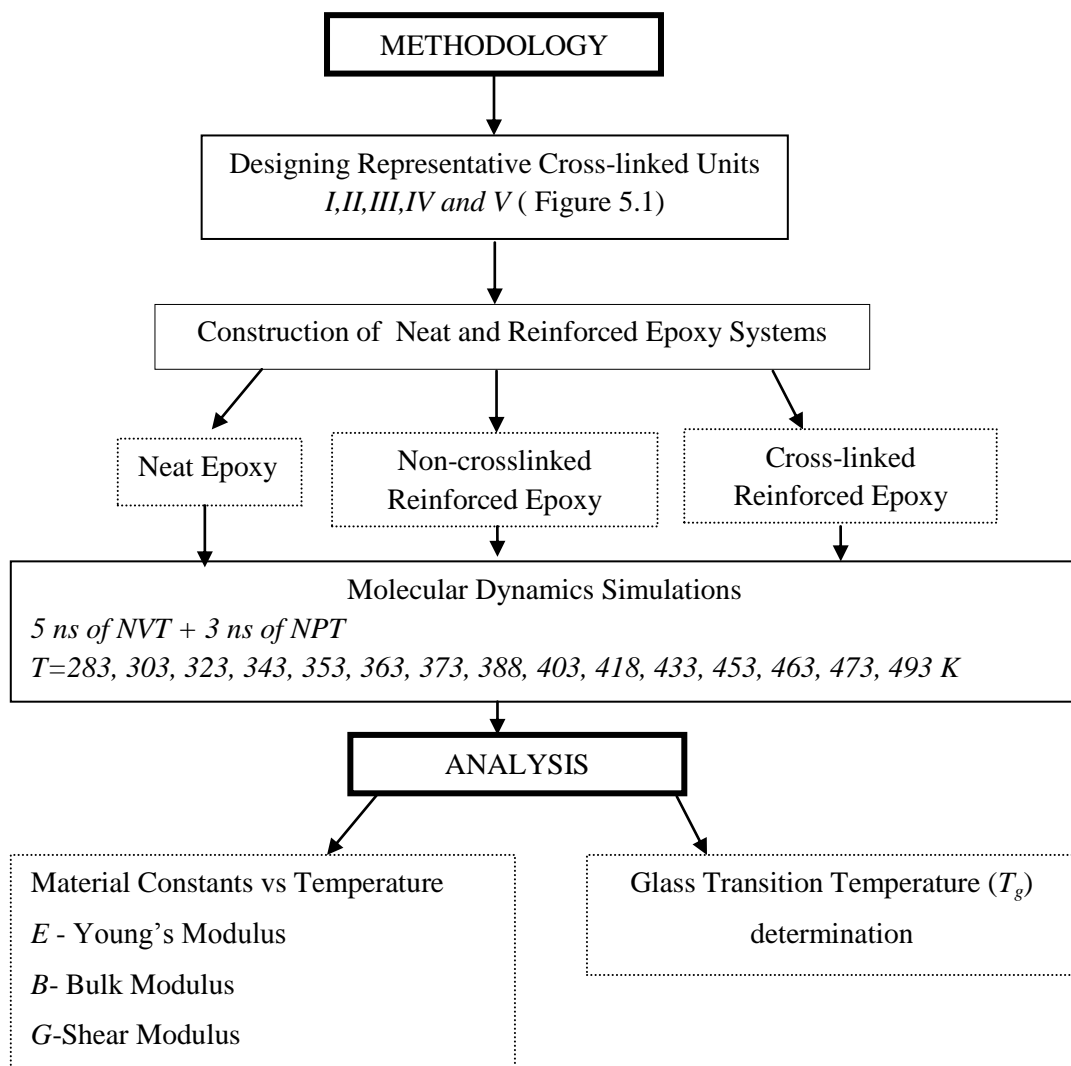
As discussed in earlier chapters, nanofiber reinforced polymer composites are commonly designed with the primary aim of obtaining superior mechanical properties in advanced structural applications, but they are also promising candidates as functional materials [91]. We demonstrated that nanofibers can provide the reinforcing function, particularly when they have good fiber-matrix adhesion, (*Chapters 2&3* [2, 3]). Cross-linked epoxy resins are often preferred as matrix in composites including the nanofibrous composites [91]. They have also been studied by computational materials

science methods, e.g. by molecular dynamics (MD) simulations to improve the understanding of epoxy cross-linked networks [92-94].

*Section 5.2.1* presents such an investigation by MD simulations, specifically towards the epoxy matrix nanocomposite mechanical behavior and the chemical interactions between the matrix and filler. The reinforcing materials of interest are surface reactive P(St-co-GMA) nanofibers, for which experimental insight was reported in earlier chapters. Correlation of the MD simulations and experimentally observed effect of the nanofiller chemistry on the mechanical properties of epoxy matrix-based nanocomposites is sought. *Section 5.2.1* is organized as follows: First, MD simulation methodologies are described. In reference to earlier studies in this field [93, 94] diglycidyl ether of bisphenol F (EPON862®) and triethylenetetramine (TETA®) in conformity with the different monomers used in our experimental studies were chosen as epoxy unit monomer and the curing agent, respectively. Next, the mechanical properties of neat and reinforced epoxy systems are computed and discussed to understand the dominating reinforcing mechanism at the atomistic level. Glass transition temperature of cross-linked neat epoxy and filler reinforced epoxy systems are presented in detail.

Investigations specific to build cross-linked epoxy matrix are still needed. Therefore, to the best of our knowledge, first time in the literature, we implemented a multi-scale model to investigate reinforcing mechanism in the thermoset matrix with the cross-linking reaction, in *Section 5.2.2*. A well-parameterized, coarse-grained model for a cross-linked epoxy resin system is proposed. Then, a reverse-mapping process to project an atomistic structure back onto the coarse-grained system is carried out. MD simulations on the reverse-mapped systems allow extraction of elastic properties.

Road Map of Section 5.2.1



## 5.2 Nanoscale Fingerprints of Superior Thermo-mechanical Properties in Nanocomposites

### 5.2.1. Molecular Dynamics Simulations via Representative Cross-linked Unit Method

#### a. Methods and Systems Studied

##### i. Molecular Dynamics Methodology

In order to construct the initial molecular structures and implement all ensemble simulations and post-processes, the molecular simulation program Material Studio ® 6.0 [95] has been used, and ab initio Condensed-phase Optimized Molecular Potentials for Atomistic Simulation Studies (COMPASS) [96] forcefield is applied to describe inter- and intra-atomic interactions: valence terms including diagonal and off – diagonal cross couplings and nonbonded interaction terms.  $E_b$ ,  $E_\theta$ ,  $E_\phi$  and  $E_\chi$  represent bond, angle, torsion and out – of – plane angle coordinates, respectively. Also,  $E_{bb}$ ,  $E_{b\theta}$ ,  $E_{b\phi}$ ,  $E_{\theta\theta}$ , and  $E_{\theta\phi}$  stand for cross – coupling terms between internal coordinates which helps to predict vibrational frequencies and structural variations associated with conformational changes.

In COMPASS forcefield (see Eq. 5.1), intra-molecular interactions are quite complex compared to other force fields in polymers. Particularly, bond stretching is represented by a polynomial with terms of order two, three, and four. Nonbonded terms due to interactions between pairs of atoms that are separated by two or more atoms or for different molecules, utilizes Coulombic and Lennard-Jones functions for electrostatic and van der Waals interactions. The Van der Waals interactions are represented the Lennard-Jones 9-6 function. In calculating the non-bonded potentials, the atom-based summation with a cutoff radius of 8.5 Å is used. Electrostatic interaction by Coulomb potential can be calculated using the Ewald summation method. In regard of force-field based simulation, Dreiding 2.21 and COMPASS have been employed to study thermoset materials [92-94]. Wu *et al.* concluded that the COMPASS is more favorable than the Dreiding2.21 for crosslinked epoxy systems and

demonstrated the importance of a well-tuned forcefield for an accurate prediction of structure and properties [92].

$$\begin{aligned}
E_{Total} = & \sum_b \left[ K_2(b-b_0)^2 + K_3(b-b_0)^3 + K_4(b-b_0)^4 \right] \\
& + \sum_\theta \left[ H_2(\theta-\theta_0)^2 + H_3(\theta-\theta_0)^3 + H_4(\theta-\theta_0)^4 \right] \\
& + \sum_\phi \left[ V_1(1-\cos\phi) + V_2(1-\cos 2\phi) + V_3(1-\cos 3\phi) \right] + \sum_\chi K_\chi (\chi-\chi_0)^2 \\
& + \sum_{b,b'} F_{b,b'}(b-b_0)(b'-b'_0) + \sum_{b,\phi} F_{b\phi}(b-b_0)(\theta-\theta_0) + \sum_{b,\phi} (b-b_0) \\
& \left[ F^{(1)}_{b,\phi}(1-\cos\phi) + F^{(2)}_{b,\phi}(1-2\cos\phi) + F^{(3)}_{b,\phi}(1-3\cos\phi) \right] \\
& + \sum_{\theta,\theta'} F_{\theta,\theta'}(\theta-\theta_0)(\theta'-\theta'_0) + \sum_{\theta,\theta',\phi} F_{\theta,\theta',\phi}(\theta-\theta_0)(\theta'-\theta'_0)\cos\phi \\
& + \sum_{i,j} \frac{q_i q_j}{\epsilon_0 r_{ij}} + \sum_{i,j} \epsilon_{ij} \left[ 2 \left( \frac{r_{ij}^0}{r_{ij}} \right)^9 - 3 \left( \frac{r_{ij}^0}{r_{ij}} \right)^6 \right]
\end{aligned} \tag{5.1}$$

## ii. Material constants for mechanical behavior

If the representative element is in equilibrium, the external stress must be exactly balanced by internal forces. Therefore, in the MD simulations the *shear moduli* ( $G$ ) of all atomistic unit cells are calculated using Material Studio ® 6.0 [95] where uniform external stress is applied to the unit cell. Stiffness matrix ( $C$ ) calculated from the second derivative of potential energy ( $U$ ) with respect to strain ( $\epsilon$ ):

$$C_{ij} = \frac{1}{V} \frac{\partial^2 U}{\partial \epsilon_i \partial \epsilon_j} \tag{5.2}$$

For small deformations, strains are given by generalized Hook's law as in Eq. 5.3.

$$\epsilon_{lm} = S_{lmnk} \sigma_{nk} \tag{5.3}$$

where  $\sigma$  is the stress and  $S_{lmnk}$  denotes the compliance components (inverse of the stiffness matrix  $C_{lmnk}$ ), respectively.

The Eq.5.4 and Eq.5.5 are for the Reuss and Voight definitions of the shear modulus, while the Hill values (Eq.5.6) are defined as the average of the two:

$$G_{VOIGHT} = \frac{1}{15}(C_{11} + C_{22} + C_{33}) + (-C_{12} - C_{13} - C_{23}) + 2(C_{44} + C_{55} + C_{66}) \quad (5.4)$$

$$G_{REUSS} = \frac{15}{4(S_{11} + S_{22} + S_{33} - S_{12} - S_{13} - S_{23}) + 3(S_{44} + S_{55} + S_{66})} \quad (5.5)$$

$$G_{HILL} = G = \frac{G_{REUSS} + G_{VOIGHT}}{2} \quad (5.6)$$

*Bulk modulus* ( $K$ ) in Eq. 5.7 is computed by the reverse of isothermal compressibility using the equation below;

$$K = \frac{k_B T \langle V \rangle}{\langle V \rangle^2 - \langle V^2 \rangle} \quad (5.7)$$

where  $\langle V \rangle$  is the average volume of the unit box,  $T$  is the temperature in kelvin units and  $k_B$  is Boltzmann constant. Young's Modulus ( $E$ ) is calculated by combining bulk modulus ( $K$ ) data from trajectory and shear modulus ( $G$ ) data from dynamic method as in Eq. 5.8:

$$E = \frac{9KG}{G + 3K} \quad (5.8)$$

Glass transition temperatures ( $T_g$ ) of these systems were determined by two different methods. In the first method, shear and Young's modulus data points are fitted to Boltzmann sigmoidal function to detect transition temperatures. Secondly,  $T_g$  is estimated from the relation of mean density of the system- temperature.

### iii. Designing representative crosslinked systems using MD simulations

Considering the computational cost of MD simulations, it is not practical to exactly reproduce atomic models of the epoxy-based polymers which are described in *Chapters 2 & 3*. To build cross-linked thermoset matrices, Yu *et al.* [93] proposed to use representative cross-linked units which can accurately describe the chemical structure

and estimate the mechanical properties. Following this idea [92, 93], we selected five epoxy unit designs as representative molecules (see Figure 5.1) and investigated their properties as described in our work [5]. Since there is no tractable difference between the five designs, and the degree of cross-linking is not totally controllable in the experiments, we use a final network structure containing all five of the different types of cross-linked units which is indicated as *neat epoxy case* in this study (See Figure 5.2 b).

After the cell construction containing five different cross-linked units, 1 molecule of I and 2 molecules each of II, III, IV, V cross-linked units, all the unit cells were simulated at fifteen different temperatures (283, 303, 323, 343, 353, 363, 373, 388, 403, 418, 433, 453, 463, 473 and 493 K) using 5 ns in NVT (fixed number of atoms, fixed volume and temperature) and 3 ns in NPT (fixed pressure, number of atoms and temperature) ensemble. At each temperature, the elastic modulus of the mixture unit cell structure is obtained using the same method as described in the previous subsection, and the results of at least 10 different simulations in each case are averaged for computational accuracy. Two models, *non-crosslinked reinforced system model* - the EPON 862 matrix reinforced with non-bonded P(St-co-GMA) molecule and *cross-linked reinforced system model* EPON 862 matrix reinforced with bonded P(St-co-GMA) molecule are studied. In the cross-linked case, the P(St-co-GMA) is bonded directly to a molecule of representative epoxy unit III, as illustrated in Figure 5.2a. Another detailed temperature sweep is performed on these reinforced model structure. We should emphasize that “cross-linked” term in reinforced systems represents the physical bonding between filler and epoxy matrix. To clarify, we already have constructed cross-linked network formed by five different representative cross-linked units in neat epoxy systems.

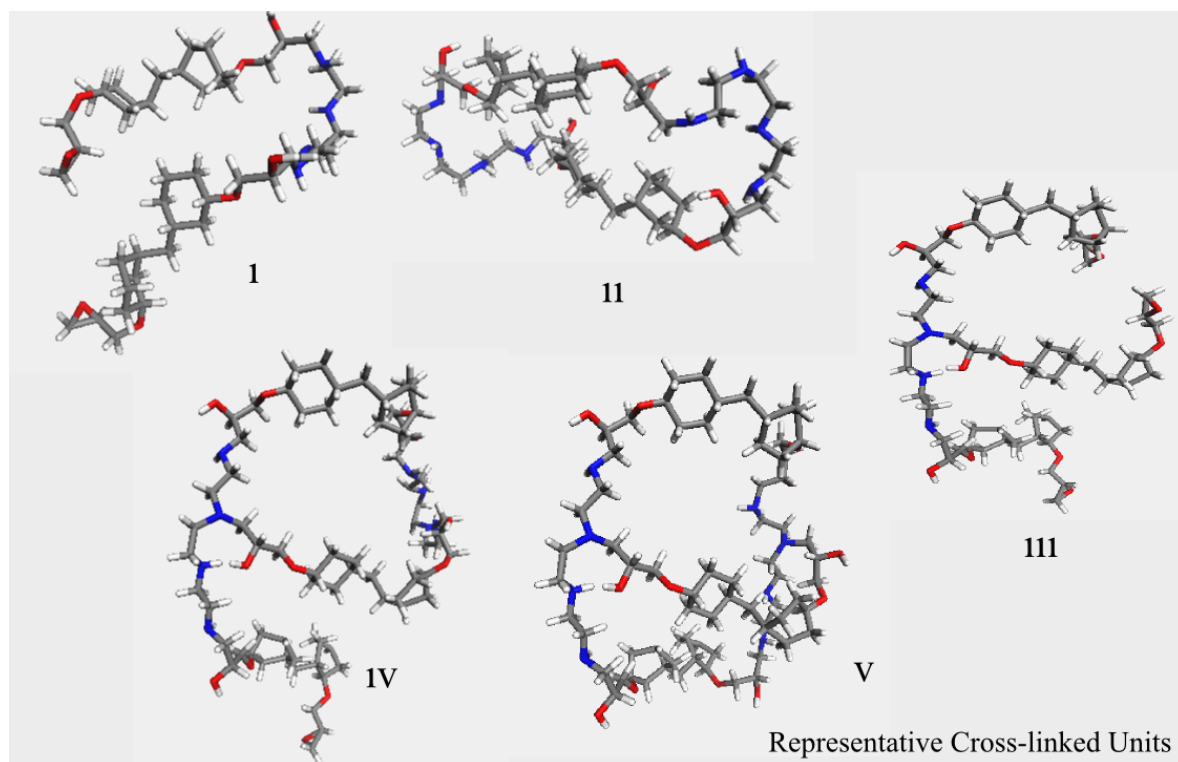


**Figure 5.1.** Five different representative cross linked units containing EPON 862 and TETA hardener stick model (red for oxygen, gray for carbon, white for hydrogen, blue for nitrogen).



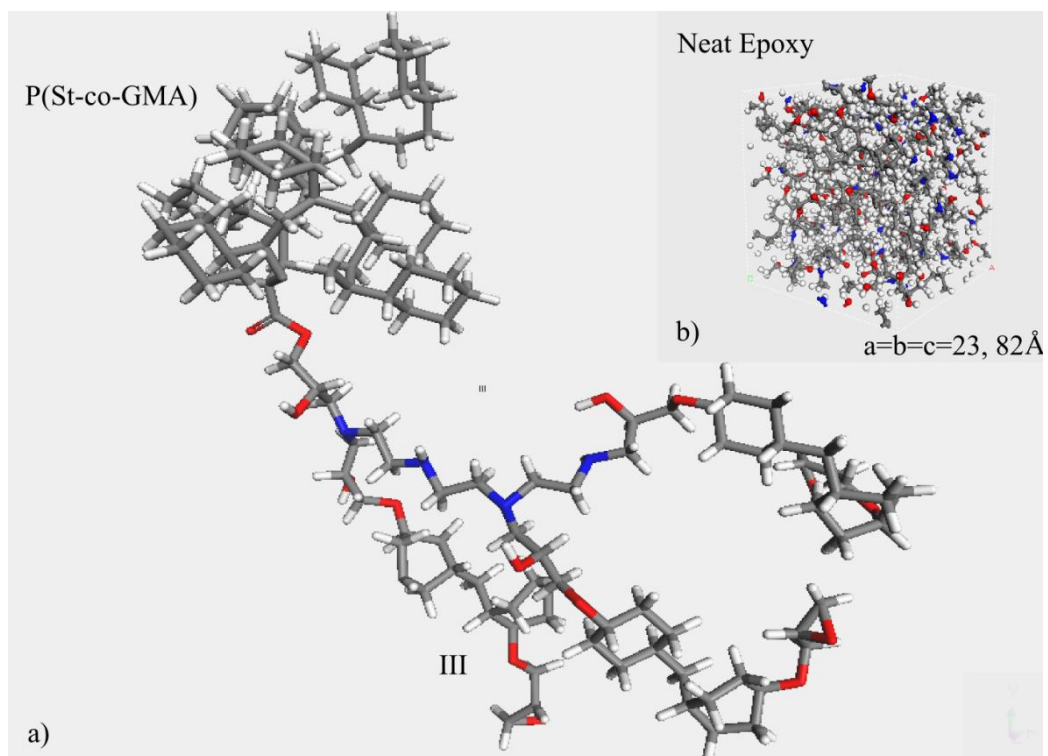


**Figure 5.2.** (a) Representative cross-linked unit bonded-III bonded to P(St-co-GMA) molecule: stick model; (b) Molecular model of neat epoxy systems generated: in ball-stick representation (red for oxygen, gray for carbon, white for hydrogen, blue for nitrogen).

## b. Results and Discussion

### i. Temperature effect on neat and reinforced cross-linked epoxy

First bulk modulus was computed from the inverse of isothermal compressibility using the trajectory from the last 2 ns NPT simulations at each temperature. The trajectories were divided into 5 chunks of 400-ps length, each yielding 400 data points. The results emphasize that bulk modulus ( $K$ ) decreases as the temperature increases, and all three system converges to a plateau, as in Figure 5.3a. Shear moduli ( $G$ ) of three systems follow the same trend with bulk moduli. In addition, as discussed in Figure 2.6, the same temperature effect on storage modulus was observed also experimentally. However, the transition temperatures between the high modulus and low modulus zone were more distinctive in Figure 5.3b. In Figure 5.3c the calculated values of the Young's modulus for the systems of neat epoxy versus those containing reinforcing agents are presented. Comparison of the MD based Young's moduli predictions for P(St-co-GMA) nonbonded and bonded to epoxy molecules correlates with the

macroscale experimental finding in *Chapter 2&3*. The experimentally observed benefit in the mechanical response due to the presence of the filler is preserved at elevated temperatures by supplementary GMA–epoxy interactions. However, we should emphasize that neither the high molecular weight polymers nor the incorporation of 2 wt % of nanofibers in the experiment are represented in our MD simulations. Therefore, the order of magnitude of the reinforcing effect is significantly different compared to experimental results, which are discussed in earlier Chapters. Nonetheless, integration of a single molecule of P(St-co-GMA) either bonded or nonbonded increases the Young's modulus compared to the neat epoxy system by 9% and 6% at 493 K, respectively.

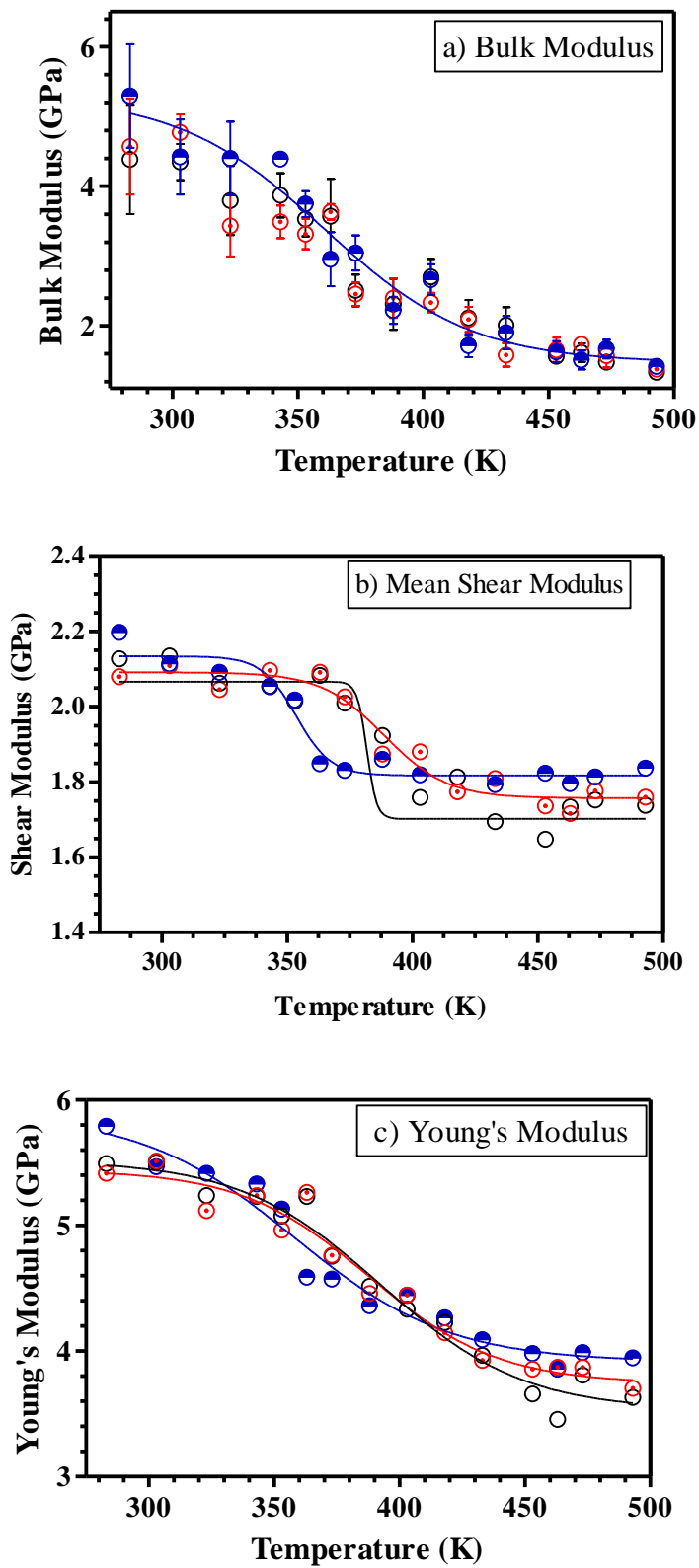


**Figure 5.3.** (a) Bulk modulus (b) shear modulus (c) Young's modulus vs temperature results of neat (black dotted), noncross-linked (red dotted) and cross-linked (blue dotted) reinforced epoxy system.

## ii. Glass Transition Temperature Determination

Bulk, shear and Young's modulus versus temperature results demonstrated that the mechanical response of these three systems exhibit two plateaus and a transition region. Determination of  $T_g$  would be interpreted from this transition region. Shear and Young's modulus data points were fitted to the Boltzmann sigmoidal function and best fit-V50 values were indicated as the  $T_g$  of different systems (Table 5.1). The second method was to estimate  $T_g$  from the relation of average density- temperature (See Figure 5.4). The density of the cell at each temperature from 283 K to 493 K was obtained from the last 2 ns of the NPT runs. The results demonstrated that  $T_g$  was depressed within the addition of P(St-co-GMA) which has lower  $T_g$  than EPON862 epoxy matrix. We emphasized in *Chapter 2* that  $T_g$  of P(St-co-GMA) was around 95°C (368 K). On the other hand, experimentally reported  $T_g$  values of EPON862-TETA hardener matrix is around 140°C (413 K) [97]. Thus, depletion in  $T_g$  could be interpreted in terms of observed kinetics of reinforcing agent and polymer matrices.

**Table 5.1.**  $T_g$  determination of neat, noncross-linked and cross-linked epoxy systems using the fitting method of the mechanical response and density average.

System	$T_g$		$T_g$		$T_g$
	(Young's Modulus)	R <sup>2</sup>	(Shear Modulus)	R <sup>2</sup>	(density average)
<i>Neat Epoxy</i>	393±6 K	0.97	382±21 K	0.81	381±10 K
<i>Non-crosslinked Reinforced</i>	388±7 K	0.97	389±5 K	0.96	377± 4 K
<i>Cross-linked Reinforced</i>	358±9 K	0.96	354±3 K	0.95	365 ± 4 K

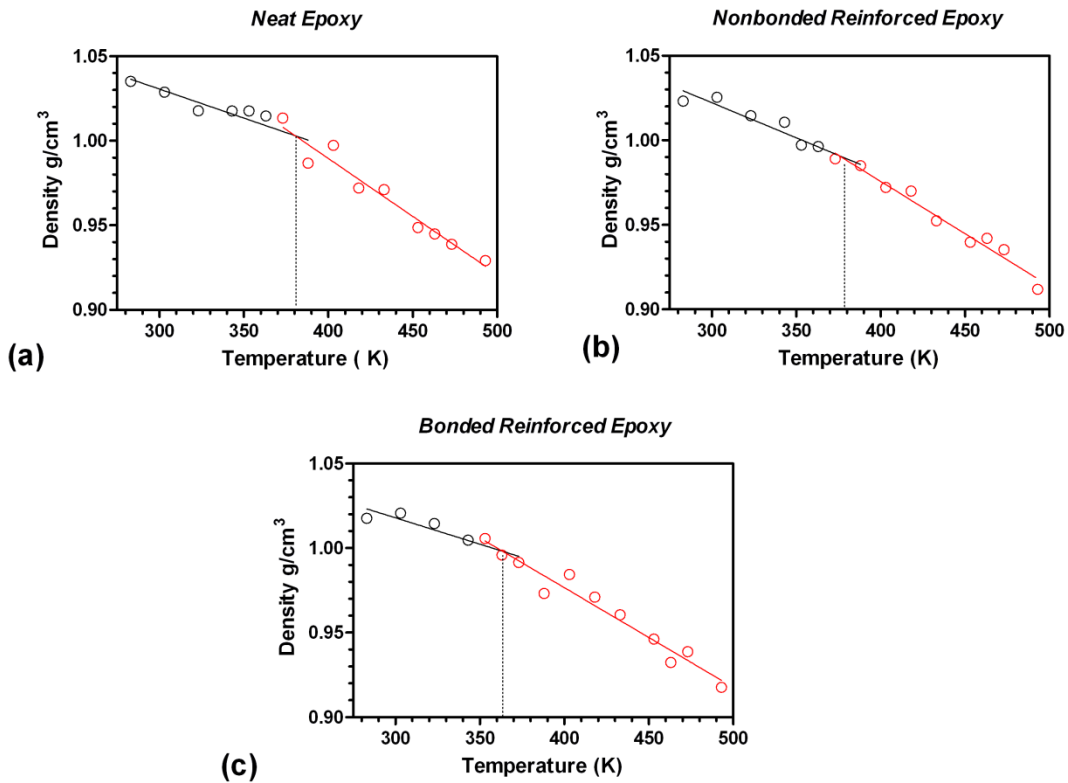
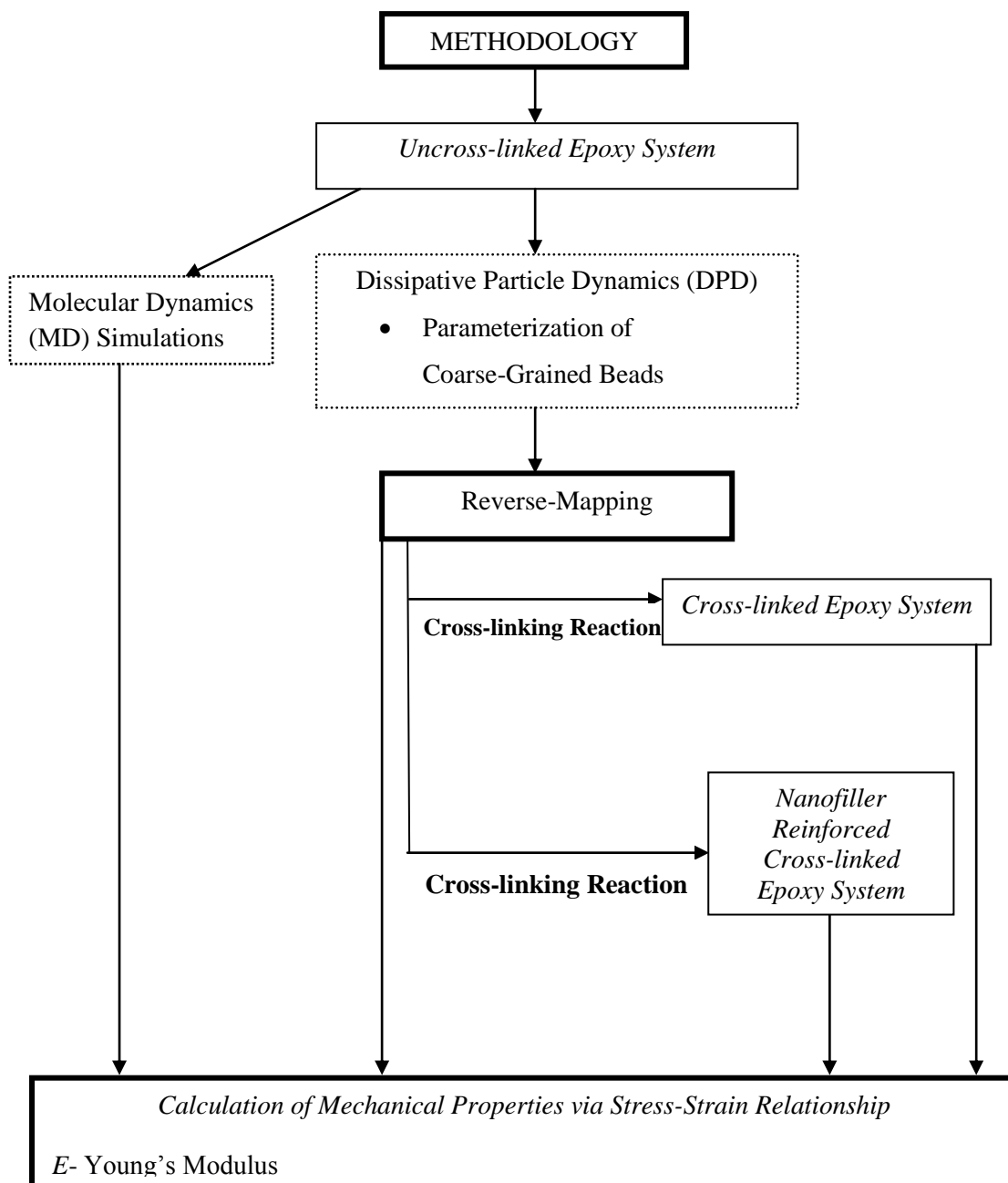


**Figure 5.4.** The mean density values versus temperature (a) neat epoxy (b) noncross-linked reinforced epoxy and (c) cross-linked reinforced epoxy.

### c. Concluding Remarks-I

MD simulations are employed to address the differences in the temperature dependence of the Young's modulus when the characteristics of fiber-epoxy interface in the nanocomposites are modified. We find that the contribution of both covalently and non-covalently bonded P(St-co-GMA) molecules have the similar influence of retaining a more elevated Young's modulus at temperatures above  $T_g$ . On atomistic-scale a kinetic parameter,  $T_g$ , can be detected and manipulated in composite polymeric systems. Results corroborating the experiments suggest that enhanced adhesion between nanofiber and matrix may be designed by modifying the chemistry of the constituents to retain a high modulus beyond the  $T_g$ . That moduli are modified only above  $T_g$  implies that the interactions along the interface are activated only when additional relaxation modes in the polymeric chains are onset.

Road Map of Section 5.2.2



## **5.2.2 Mapping and Reverse-Mapping of Epoxy Matrix System for a Molecular Understanding of Mechanical Response**

### **a. Methods and Systems Studied**

#### **i. Molecular Dynamics Methodology**

The molecular simulation software package Materials Studio<sup>®</sup> 6.0 [95] was used to construct the initial molecular structures, simulations and post-processing the collected trajectories. COMPASS [96] (Condensed-phase Optimized Molecular Potentials for Atomistic Simulation Studies) force field used in this study has been shown to be very effective in defining properties of synthetic polymers. The van der Waals interactions use the Lennard-Jones 9-6 function. In calculations of the non-bonded potentials, the atom-based summation with a cutoff radius of 8.5 Å was used. Electrostatic interaction by Coulomb potential was calculated using the Ewald summation method. Simulation boxes constructed using the Amorphous Cell module contained 375 molecules of EPON 862 and 125 molecules of TETA hardener at target density of 1.0 g/cc. MD simulations of the epoxy-hardener systems were carried out in the isothermal-isobaric (NPT) statistical ensemble, at  $P=1$  atm and  $T=298$  K. To maintain temperature and pressure fixed at their prescribed values, the Andersen-Berendsen thermostat-barostat was used [98, 99].

#### **ii. Coarse-Graining of Epoxy System without Cross-linking**

Coarse-grained DPD simulations are performed on a collection of particles, each made up of a suitably selected set of atoms (see below). The force acting on a given bead at each time step is the sum of soft repulsive forces acting along the line connecting the bead to its neighbors, a dissipative term and a random force term. In addition, a harmonic force connects the beads that are located consecutively along the contour of a chain. In a DPD simulation, the chains need to be partitioned into beads made up of chemically distinct units that also have similar sizes. The units we use in the current study are displayed in Figure 5.5 whereby the **A**, **B<sub>1</sub>**, **B<sub>2</sub>** and **C** units represent

epoxy and hardener segments. Hildebrand solubility parameters ( $\delta$ ) [100] were calculated from successive 1 ps equilibrations step and 100 ps MD simulations on simulation boxes that contain 10 beads of the same type with a density of 1.0 g/cc at 298 K, using the Amorphous Cell and Forcite modules of Materials Studio<sup>®</sup> [95]. For all non-bonded interactions, a cut-off radius,  $r_c$ , of 8.5 Å and periodic boundary conditions were applied in the canonical ensemble (NVT). Molar volume of the beads,  $V_m$ , was calculated using the ACDLabs/Chemsketch 5.0 [101]. Hildebrand solubility parameters were determined according to

$$\delta = \left( \frac{\Delta E_v}{V_m} \right)^{1/2} = (CED)^{1/2} \quad (5.9)$$

where  $\Delta E_v$  and CED correspond to molar energy of vaporization and cohesive energy density, respectively. Flory-Huggins interaction parameter,  $\chi$ , of the beads were then calculated from,

$$\chi = \frac{V_m(\delta_i - \delta_j)^2}{RT} \quad (5.10)$$

where  $V_m$  is the average molar volume of the beads  $i$  and  $j$ . The calculated values of  $\delta$  and  $V_m$  are displayed in Table 5.2. Flory-Huggins interaction parameter  $\chi$ , is related to the thermodynamics of mixing, and the DPD interactions parameters,  $a_{ij}$ , obtained from  $\chi$  is a measure of repulsion between the beads. The latter are calculated using the linear relationship put forth by Groot and Warren *et al.* [102] as  $a_{ii} = 25k_bT$  and  $a_{ij} \approx a_{ii} + 3.27\chi_{ij}$  for a box density of 3 DPD units (Table 5.2). We note that this treatment assumes equal repulsive interactions between like beads which is strictly true only when the molar volumes of the two components are equal [103]. For DPD simulations, using 3:1, epoxy: hardener, stochastic ratio simulation box was constructed by using the beads shown in Figure 5.6. Cubic boxes having  $50 \times 50 \times 50 u^3$  volume are constructed with a density of 3 DPD units where  $u$  is the cut-off radius. A harmonic spring constant of 4.0 was chosen for beads located consecutively along the chain. Temperature and each bead mass were taken as unity. The systems were equilibrated for 20,000 DPD steps, followed by 100,000 DPD steps for data collection and analysis. To test the accuracy of coarse-graining parameters, radial distribution function (RDFs) ( $g(r)$ ) of atomistic and



coarse-grained (**A**, **B<sub>1</sub>**, **B<sub>2</sub>** and **C**) sets were computed and corresponding potential  $V(r)$  for each set were generated via Boltzmann Inversion

$$V(r) = -k_B T \ln(g(r)) \quad (5.11)$$

where  $k_B$ ,  $T$ ,  $g(r)$  are Boltzmann constant, temperature (in kelvin) and pair correlation function, respectively.

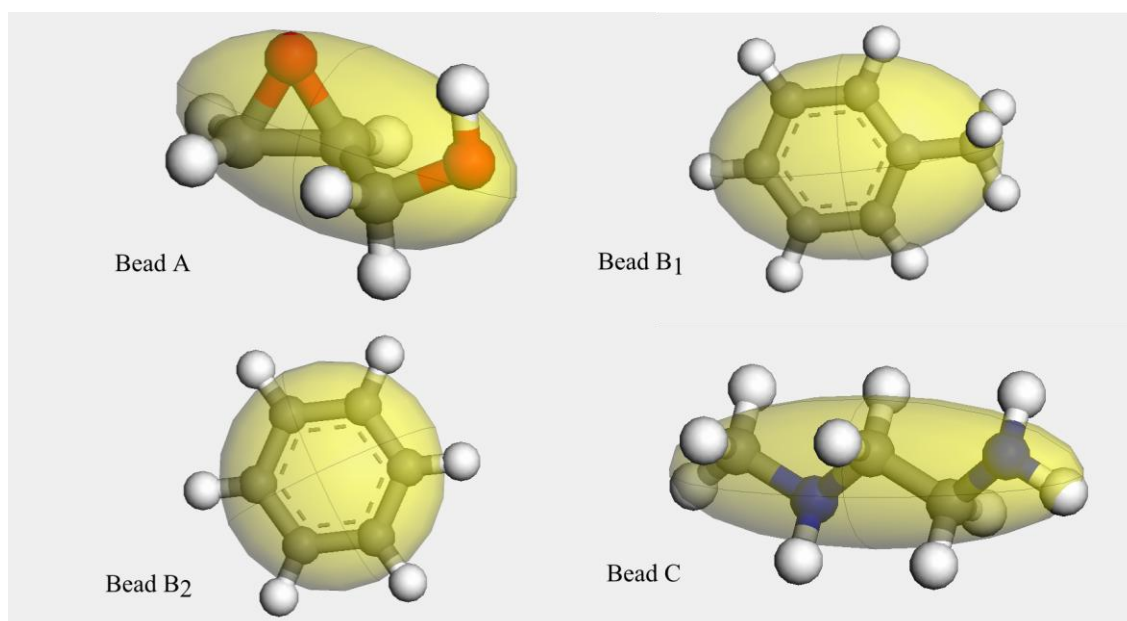


**Figure 5.5.** Partitioning of the beads (**A**, **B<sub>1</sub>**, **B<sub>2</sub>** and **C**) for coarse-grained simulations ball-stick model (red for oxygen, gray for carbon, white for hydrogen, blue for nitrogen).

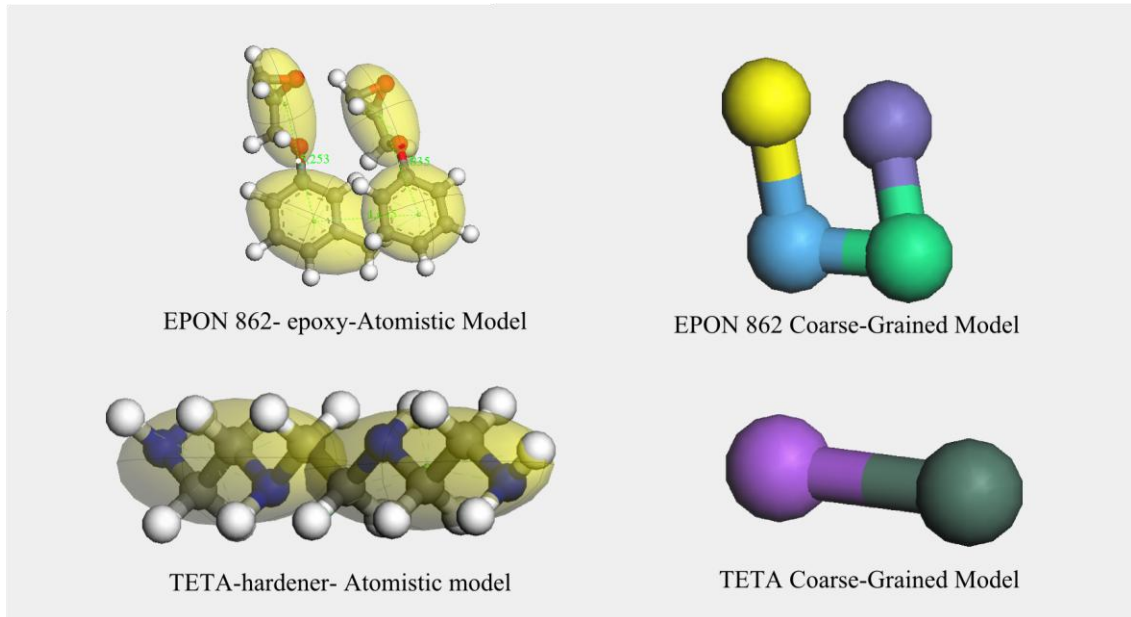


**Figure 5.6.** Atomistic ball-stick model and coarse-grained model representations of epoxy (EPON 862) and hardener (TETA) molecules, individual motion groups are represented in yellow shading.

**Table 5.2** Properties of beads as defined in Figure 5.5. Solubility parameters,  $\delta$ , molar volume  $V_m$ , and DPD interaction parameters,  $a_{ij}$ .

	A	B <sub>1</sub>	B <sub>2</sub>	C
$\delta, (cal/cm^3)^{1/2}$	12.46	9.58	9.99	12.66
$V_m (cm^3/mol)$	62.8	105.7	89.4	90.5
<b>A</b>	25	28.86	27.56	25.02
<b>B<sub>1</sub></b>	28.86	25	25.09	30.14
<b>B<sub>2</sub></b>	27.56	25.09	25	28.54
<b>C</b>	25.02	30.14	28.54	25

### iii. Calculation of Mechanical Properties via Stress-Strain Relationship

To calculate mechanical properties, another approach (different from *Section 5.2.1*) was implemented. Stress-states associated with the compressive loading was obtained from the deformation of cell. For each strain, the unit cell was compressed along one dimension (e.g. *y-direction*), and the other two dimensions (e.g. *x and z directions*) were extended to maintain the constant density; in each compression, the periodic cell was

rebuilt with the new dimensions. In each deformation step, an equilibration run of MD was performed and system was relaxed. Later, normal and shear stresses in all directions were recorded. Interpretation of stress-strain relationship was used to back-calculate Young's Modulus ( $E$ ) of uncross-linked, and reinforced epoxy systems.

## **b. Results and Discussion**

### **i. The Accuracy of Parameterization in Coarse-Graining**

We utilized DPD simulations to predict  $x$ ,  $y$ ,  $z$  coordinates of epoxy and hardener mixture at long equilibrium ( $\approx 25$  ns) in contrast to much shorter time scans in MD runs typically limited by the computational intensity. That being said, DPD interaction parameters,  $a_{ij}$ , should be well-parameterized in order to have accurate atomic positions. As seen in Figure 5.7, interaction potentials  $V(r)$  of bead sets (**A**, **B<sub>1</sub>**, **B<sub>2</sub>** and **2xC**) from DPD simulations, was in good agreement with iterative potentials derived from COMPASS force field in MD. Proposed coarse-graining force-field in DPD simulations has been shown to be very effective in defining properties of uncross-linked epoxy system. Further step in *Section 5.2.2* is reverse-mapping process to project an atomistic structure back onto the coarse-grained system. Therefore, Figure 5.7 demonstrated that defined bead-bead interactions preserved atomistic energetic details.

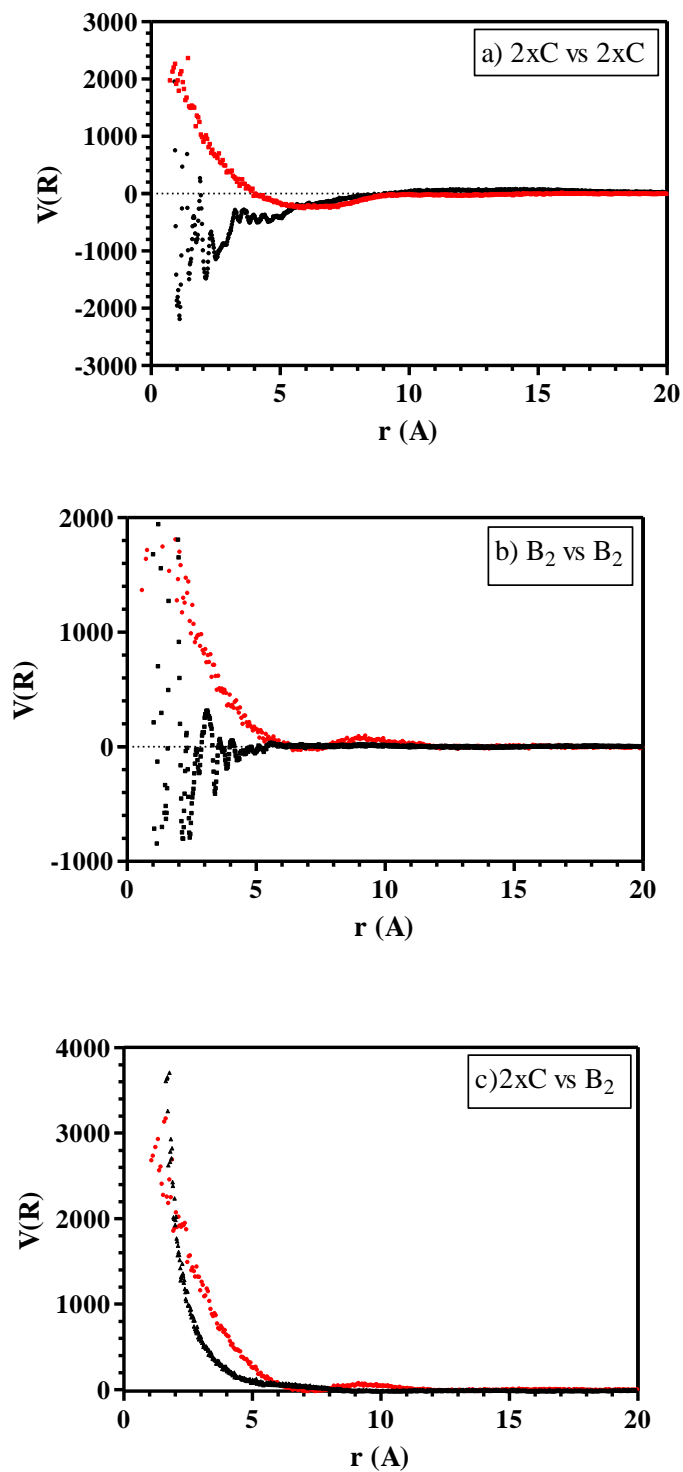


**Figure 5.7.** Effective potential,  $V(r)$ , of (a) hardener-hardener ( $2xC$  corresponds to TETA coarse-grained model) (b) epoxy-epoxy ( $B_2$  beads and representative atomistic set was selected for calculation) (c) hardener-epoxy in atomistic MD model (black dotted) and in coarse-grained model (red dotted).

## ii. Reverse-Mapping Methodology

In literature, several methods [104-111] have been proposed for reverse-mapping (RM) of the coarse-grained model into a detailed atomistic model. In our approach, general strategy in line with Marrink *et al.* [109], is adapted to reconstruct low-energy atomistic (AA) structures from their corresponding coarse-grained (CG) representations into Material Studio® program. Scripting module in Material Studio is implemented to execute reverse-mapping algorithm automatically and increase the applicability to reinforced epoxy systems while reducing data processing time. Three successive steps have been followed, to generate AA ensemble that underlies its corresponding CG system via scripting. First, AA particles were positioned close to their reference CG beads. Then, Simulated Annealing (SA) procedure was used, during which the AA system was coupled to the CG system via harmonic restraints. Finally, the restraints were gradually removed to yield a relaxed atomistic system (See Figure 5.8).

Next, we more closely characterized the energetic and structural properties of the reconstructed atomistic ensembles of the uncross-linked epoxy system. In particular, we were interested in how much information at the atomistic level can be retrieved back from well-relaxed CG structures. First, we analyzed potential energy ( $E_{pot}$ ) per unit volume of selected groups of atoms/molecules, which is also described as cohesive energy density (CED) (see Eq. 5.9) Figure 5.9 demonstrates CED for the ensembles in pure epoxy and pure hardener systems. The CED of EPON862 structure taken from the equilibrium MD and RM simulations is plotted as solid black and red line, respectively in Figure 5.9a. CED of EPON862 structure from RM simulations, are slightly lower than reference MD simulations. Similar results are also obtained for TETA hardener systems, as seen in Figure 5.9b. CED of reverse-mapped hardener and epoxy structures demonstrated that the reconstructed atomistic ensembles represent lower energy profile and yields proper ensembles of atomistic structures.

Next, cross-linking reaction will be simulated to construct cross-linked epoxy system at the atomistic level. Thus, the generation of an atomistic epoxy and hardener configuration from a CG representation while preserving structural information is an important step to investigate. In Figure 5.10a, EPON862–EPON862 radial distribution functions (RDFs) obtained from RM and direct MD simulations are compared. Epoxy molecules positioned at a closer distance compared to direct- MD simulations. On the

other hand, relative to direct MD simulations, TETA molecules preferred to stay at longer separation distance in reverse-mapped systems. The structural property of reconstructed atomistic TETA molecules corresponds to those obtained from direct MD atomistic simulations, as seen in Figure 5.10b. Chain conformations and chain dimensions over time can be interpreted as radius of gyration ( $R_g$ ) of epoxy and hardener molecules. The distribution of  $R_g$  is also a monitor applicability of Gaussian statistics of finite chain. Thus,  $R_g$  of EPON862 and TETA obtained from RM and MD simulations are compared to investigate chain conformations. In Figure 5.11a, indicated that reverse-mapped structures exhibited single peak distribution where low energy and well-relaxed systems are required to obtain this profile. Moreover, EPON chains swell more while TETA contracts (See Figure 5.11b).

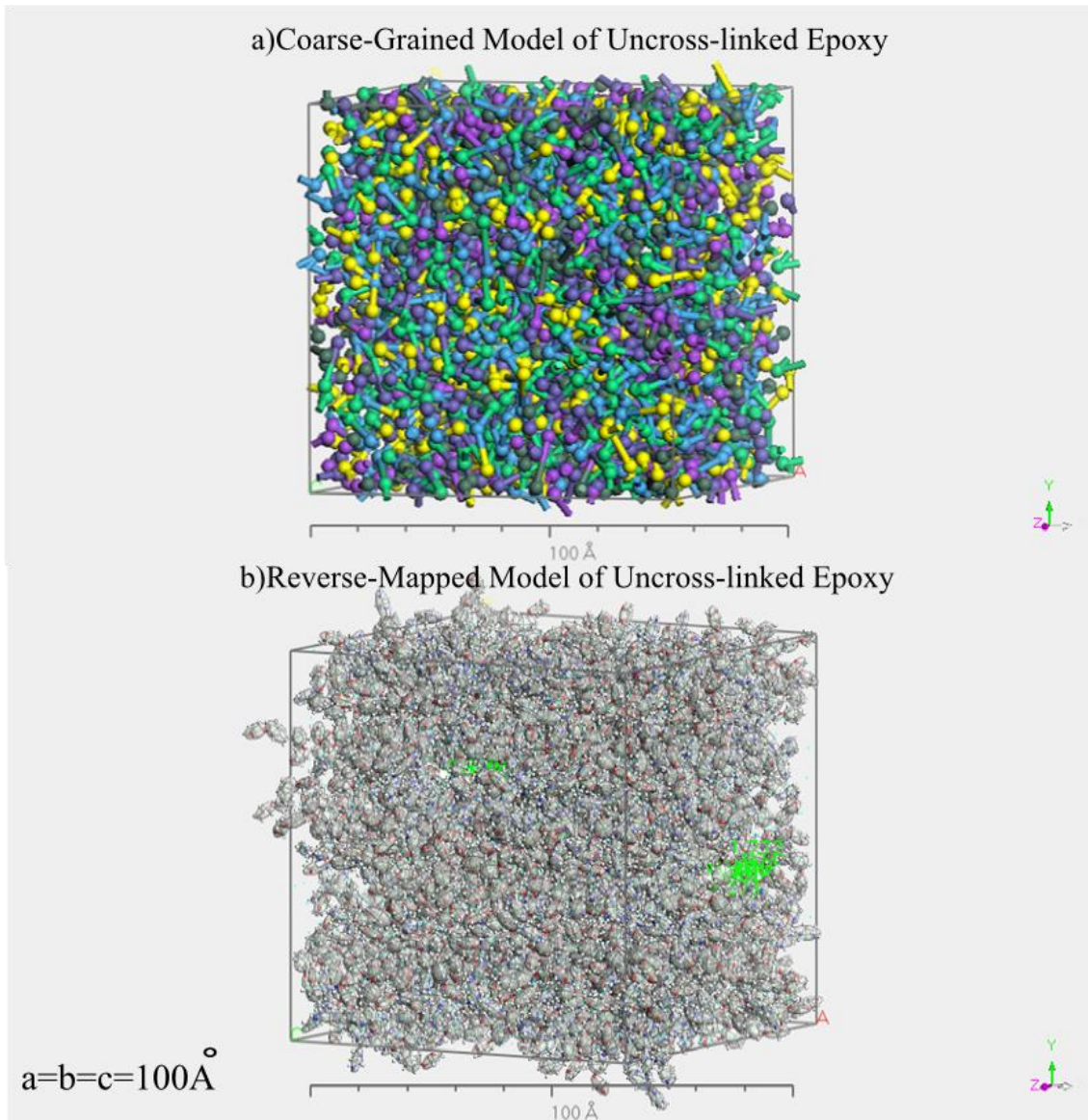


**Figure 5.8.** Reconstruction of atomic details in 100 Å simulation box, (a) Coarse-Grained representative model of uncross-linked epoxy (b) Reverse-mapped model of uncross-linked epoxy, motion groups of each atomic groups is displayed.

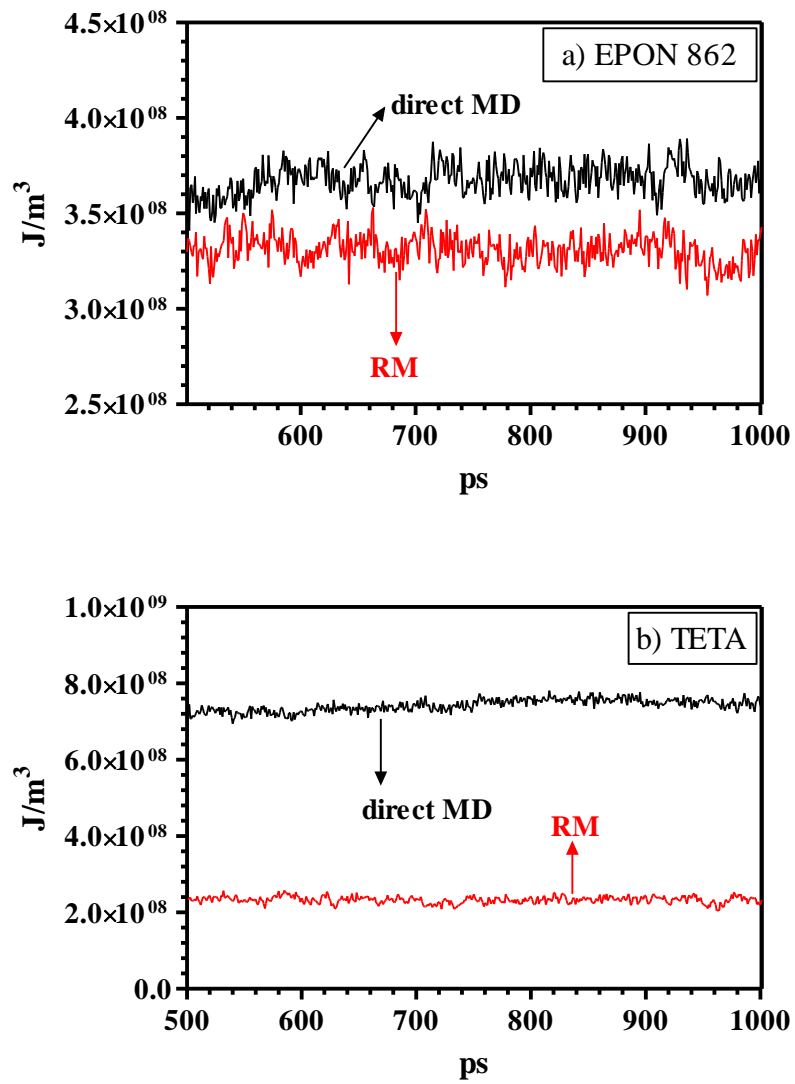


**Figure 5.9.** Cohesive energy densities of (a) pure EPON 862 and (b) pure TETA hardener systems, from reverse-mapped (RM) (solid red line) and direct atomistic-molecular dynamics (MD) (solid black line) trajectories.



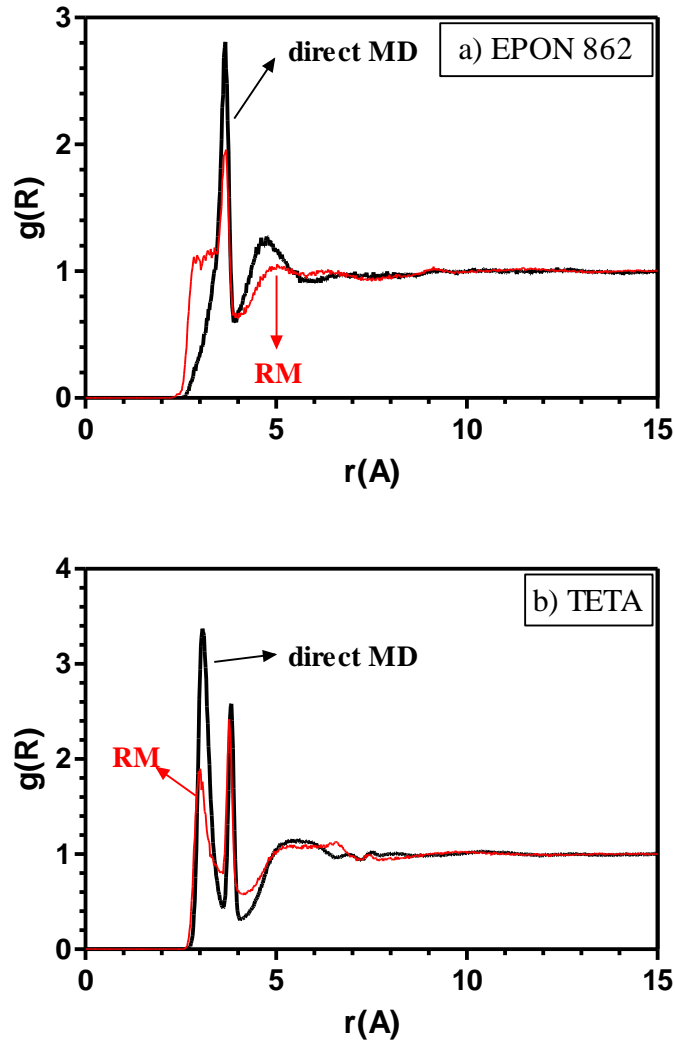


**Figure 5.10.** (a) EPON862-EPON862 radial distribution functions of reverse-mapped (solid red line) and direct MD (solid black line) structures. (b) TETA-TETA radial distribution functions of reverse-mapped (solid red line) and direct MD structures (solid black line)

### iii. Preliminary Mechanical Properties of Uncross-linked Epoxy

In *Section 5.2.2*, compression loading on the representative element was simulated at the atomistic scale to investigate mechanical properties of reverse-mapped and MD uncross-linked epoxy structures. Each equilibrated configurations is simulated under axial loading when the only applied compressive force is along its longitudinal  $y$  direction. After each compression, an equilibration run about 100 ps of MD was performed and the stress was averaged in normal and shear directions over the last half of the equilibration run. Normal stresses obtained from described method in transverse

$x$  and  $z$  directions are shown in Figure 5.12. Two different equilibrated configurations obtained from MD and RM systems were compared in terms of their transversal stress states. Normal stresses in  $x$  and  $z$  directions are overlapping, as seen in Figure 5.12b which pointed out the isotropic behavior of reverse-mapped structures at the atomistic-scale. We should emphasize that at this level of research, cross-linking reaction is not our focus. Low-energy-cross-linked structures do not have to exhibit isotropy in both transverse directions. We stated that RM structures ( $\approx 25$  ns) are in lower-energy states than configurations obtained from MD simulations (5 ns). Thus, while same normal stress profiles in  $x$  and  $z$  directions ( $\sigma_{xx}$  and  $\sigma_{zz}$ ) could be provided by projecting atomistic details back onto the long, relaxed coarse grained systems, we could not observe same transverse stress profile in MD simulations, as seen in Figure 5.12a.

Normal stresses in  $y$  direction ( $\sigma_{yy}$ ) are displayed in Figure 5.13a. Moreover, less stress fluctuations in  $y$ -directions compared to MD simulations are observed in RM structures (Figure 5.13a). Isotropic material assumption could be implemented to calculate material constants such as in Eq 5.12 Young's Modulus ( $E$ ). (Please see stress differences in transverse direction in Figure 5.13b). Preliminary results indicate that calculated Young's Modulus via stress-strain relationship, which is  $336\pm 10.2$  MPa, is lower than our earlier computational findings in *Section 5.2.1*. However, we studied uncross-linked epoxy systems. Thus, cross-linking procedure is our next research interest to build representative cross-linked epoxy system.

$$E_{yy} = \frac{\sigma_{yy}}{\varepsilon_{yy}} = E \quad (5.12)$$

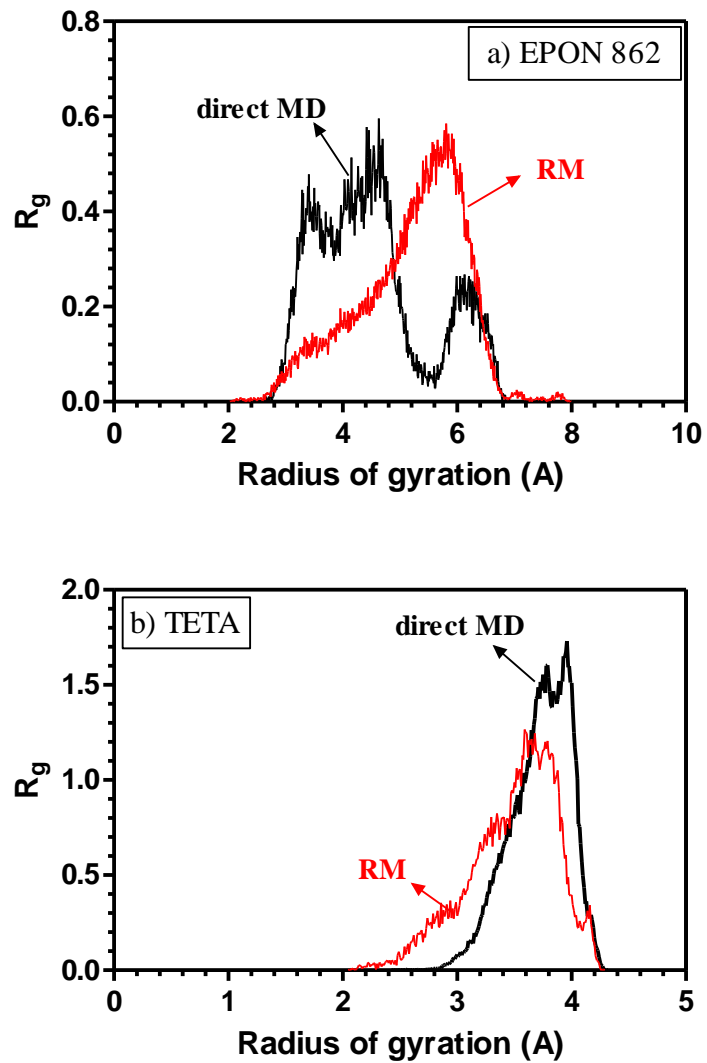


**Figure 5.11.** (a)  $R_g$  of EPON862 in reverse-mapped (solid red line) and direct MD (solid black line) structures. (b)  $R_g$  of TETA in reverse-mapped (solid red line) and direct MD (solid black line) structures.

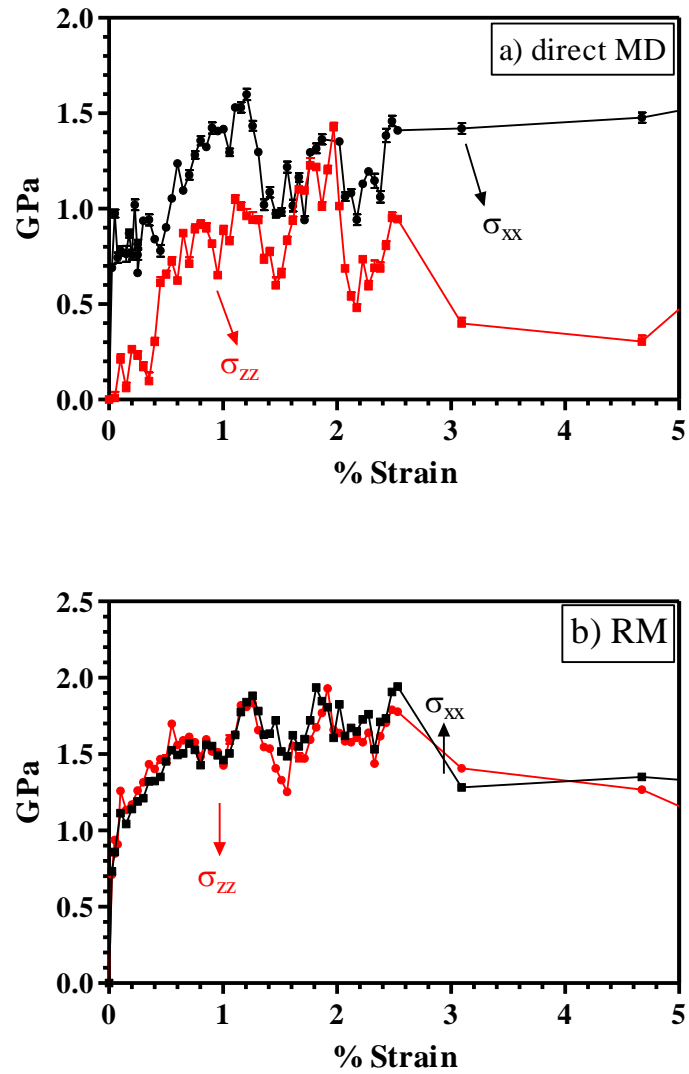


**Figure 5.12.** Average transverse normal stresses in  $x$  and  $z$  directions ( $\sigma_{xx}$  (solid black line) and  $\sigma_{zz}$  (solid red line)) obtained from (a) direct MD structures and (b) reverse-mapped atomistic structures.

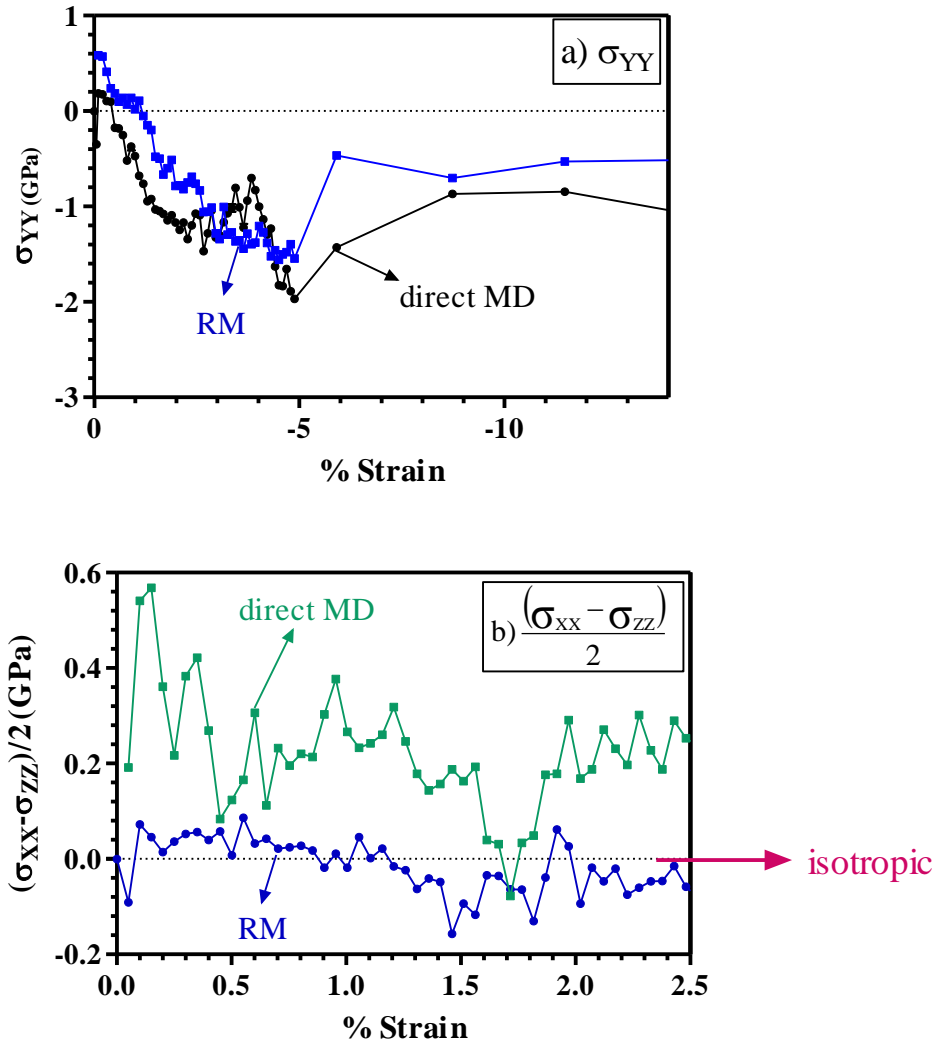


**Figure 5.13.** (a) Average uniaxial normal stresses in y direction ( $\sigma_{yy}$ ) obtained from direct MD (solid black line) and reverse-mapped (solid blue line) atomistic structures (b) average transverse stress differences ( $(\sigma_{xx} - \sigma_{zz})/2$ ) of MD (solid green line) and RM (solid blue line) structures.

### c. Concluding Remarks-II

Coarse grained DPD simulations has been employed for investigating the longer time- and length-scale dynamics of neat and reinforced uncross-linked epoxy systems. To the best of our knowledge, for the first time in nanocomposite systems, reverse-mapping process to project an atomistic structure back onto the coarse-grained system has been carried out. The overall mechanical response of uncross-linked matrix generated from both reverse mapped and atomistic systems when subjected to mechanical loading, is provided by stress-strain relationship at the atomistic scale.

## CHAPTER 6

### CONCLUSION AND FUTURE WORK

#### 6.1. Ongoing Studies: Cross-Linking Reaction at the Atomistic Scale and Reinforced Epoxy Matrices

Another algorithm was created to simulate cross-linking reaction at the atomistic level. This script was designated to create cross-links in a system containing an oligomer (EPON 862) and a cross-linking molecule (TETA). Reactive atoms on the EPON862 and TETA cross-linker were selected by assigning a specific name to the atoms (e.g.  $R_1$  and  $R_2$ ). Close contacts were calculated between the reactive atoms and bonds were created if atoms have names  $R_1$  and  $R_2$ . Once close contacts were built, new connections were created and hydrogen atoms were reset. To relax the new formed bonds, we performed short optimization (50 ps). Fan *et al.* [112] emphasized that based on the weight ratio (100:15.4) of the mixed epoxy and the curing agents, the ratio of epoxy: hardener molecules must be 3:1.

The stochastic ratio was reset in epoxy-hardener mixture; a new reverse-mapped system was redesigned. Cross-linking ratio could be adjusted and altered gradually. Preliminary stress profile results in  $x$ ,  $y$ ,  $z$  directions indicated that high degree of fluctuations was recorded during compression testing in cross-linked neat epoxy systems. Therefore, new algorithm should be considered to relax and optimize cross-linked matrices. This part of research is still in progress. New formed cross-linked epoxy systems will be tested as same method described earlier under uniaxial loading.

Moreover, nanofiller reinforced epoxy systems could be designed via same coarse-graining and reverse-mapping procedure, as illustrated in Figure 5.14. This time-

effective multi-scale modeling technique offers useful insight to nanofiller reinforced composite structures at the atomistic level. Moreover, silica nanoparticles, clay, MWCNTs, SWCNTs or any spherical/cylindrical or tube form nano-sized component could be coarse-grained and utilized as reinforcement in thermoset or thermoplastic matrices. Meso-scale system allows us to build different layers to represent nanofiller and surrounding matrix individually, as in Figure 6.1a. Via calculated  $a_{ij}$  DPD interactions, the coarse-grained meso-scale model is assigned (See Figure 6.1b). Reverse-mapping algorithm is revised to optimize and relax SWCNT (10,10) reinforced epoxy system (Figure 6.1c). Our primary goal in this part of research is to model nanofiber with/without CNT reinforced epoxy systems which is described in *Chapters 2 and 3*, to monitor dominated mechanisms at the interface.

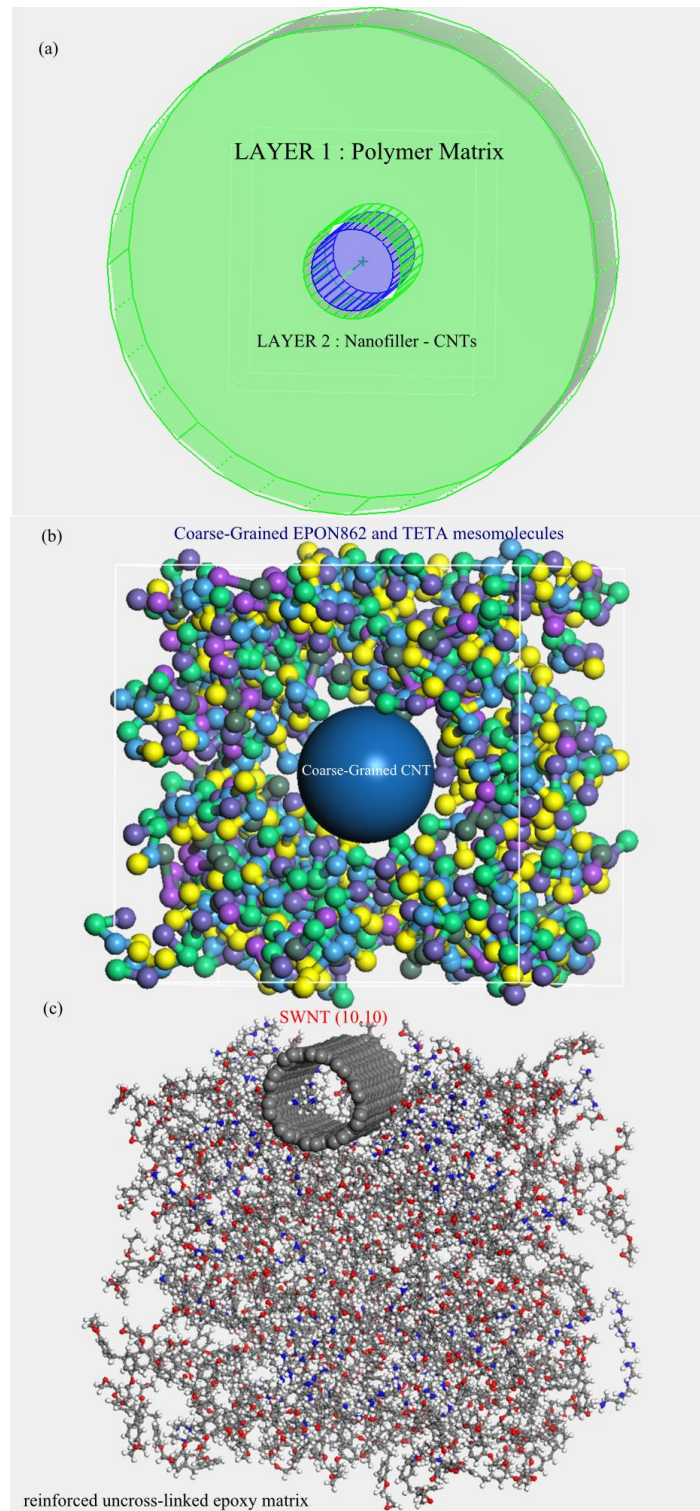


**Figure 6.1.** (a) Meso-scale system built of Layer 1 and Layer 2, each layer represents different meso-molecules (b) Coarse-grained meso-system assigned by DPD force-field (c) Reverse-mapped SWNT(10,10) (space-filled representation) reinforced epoxy system(ball-stick representation).



## 6.2. Conclusion

The synergetic effect of forming nanocomposites for superior mechanical properties combined with fidelity to other preferred properties of the excess component has been studied by experimental and numerical techniques. The novelty of this thesis is based on designing the chemistry of the electrospun nanofibers, so that the resultant composites substantially benefit from cross-linking between the nanofibers and the polymer matrix.

Overall, the idea of chemistry specific design of interface in nanofibrous matrix composites is significantly effective. The experimental results show that given the knowledge of the matrix system, smart choice of fiber polymer provides stronger interfacial bonding and improved mechanical properties. Simulation tools, on the other hand may trace the signatures of these improvements, and promise an efficient assessment methodology for interface design which can be help to optimize also the experimental efforts.

In *Chapter 2*, we focused on mimicking cross-linking in nanofiber-reinforced epoxy composites to enhance mechanical properties. Synthesized copolymers polystyrene-*co*-glycidyl methacrylate P(St-*co*-GMA) is electrospun to produce mats of surface reactive nano-to- submicron scale fibers that are accompanied later by spraying over the ethylenediamine (EDA) as a supplementary cross-linking agent for epoxy. The P(St-*co*-GMA)/EDA fiber mats are then embedded into an epoxy resin. Analysis of the three-point-bending mode of the composites reveals that the storage modulus of P(St-*co*-GMA)/EDA nanofiber-reinforced epoxy are about 10 and 2.5 times higher than that of neat and P(St-*co*-GMA) nanofiber-reinforced epoxy, respectively, even though the weight fraction of the nanofibers was as low as 2 wt %. The significant increase in the mechanical response is attributed to the inherently cross-linked fiber structure and the surface modification/chemistry of the electrospun fibers that results in cross-linked polymer matrix-nanofiber interfacial bonding.

*Chapter 3* exemplifies how embedding MWCNTs into surface modified P(St-*co*-GMA) nanofibers impact process parameters while electro-spinning, as well as the mechanical response of strengthened nanofiber-reinforced epoxy matrix. In addition, it shows the need of optimization in electro-spinning process in the explanation of

complex behavior of CNTs. Functionalization of these MWCNT/P(St-co-GMA) composite nanofibers with epoxide moieties facilitates bonding at the interface of the cross-linked fibers and the epoxy matrix, effectively reinforcing and toughening the epoxy resin. Rheological properties are determined and thermodynamic stabilization is demonstrated for MWCNTs in the P(St-co-GMA)-DMF polymer solution. Homogeneity and uniformity of the fiber formation within the electrospun mats are achieved at polymer concentration of 30 wt %. Results show that the MWCNT fraction decreases the polymer solution viscosity, yielding a narrower fiber diameter. The fiber diameter drops from an average of 630 nm to 460 nm, as the MWCNTs wt fraction (1, 1.5, and 2%) is increased. The electrospun nanofibers of the MWCNTs/P(St-co-GMA) composite are also embedded into an epoxy resin to investigate their reinforcing abilities. A significant increase in the mechanical response is observed, up to >20% in flexural modulus, when compared to neat epoxy, despite a very low composite fiber weight fraction (at about 0.2% by a single-layer fibrous mat). The increase is attributed to the combined effect of two factors: The inherent strength of the well-dispersed MWCNTs, and the surface chemistry of the electrospun fibers that have been modified with epoxide to enable cross-linking between the polymer matrix and the nanofibers.

*Chapter 4* demonstrates the potential of designed nanowebs as interlayers in commercial pre-pregs at the macro-scale. Comparisons of increase in mechanical performance by incorporating P(St-co-GMA) and P(St-co-GMA)/MWCNTs interlayers also show the contribution of MWCNTs presence in the copolymer nanofibers. Flexural strength and stiffness of (0/0/0) and (90/0/90) laminate increase up to 17% when the nanocomposite interlayers are integrated. Cross-sectional SEM analyses of the failure surfaces suggest reinforcing ability of interlayers both against transverse cracking and delamination. Further examination for the delamination resistance is presented by the End Notched Flexure (ENF) tests. An improvement up to 70% in mode II strain energy release rate ( $G_{IIc}$ ) is recorded for the laminates with nanocomposite interlayers. The resistance against transverse matrix cracking in the presence of interlayers is also elaborated. Charpy-impact and transverse-tension tests result in up to 20% and 27% increase in the impact energy absorbance and transverse tensile strength, respectively. Overall, the test results suggest that mechanical behavior of the laminates is enhanced by the nanofibrous interlayers chemically tuned for epoxy cross-linking, with no weight penalty.

In *Chapter 5*, our research interest is directed towards determining the dominating reinforcing contributions at the atomistic scale. We expect these efforts to eventually provide a more accurate representation of our experimentally tested nanocomposite systems. The first part of *Chapter 5* presents an investigation by MD simulations, specifically focusing on epoxy matrix nanocomposite mechanical behavior at the interface. These simulations are employed to address the differences in the temperature dependence of the bulk, shear and Young's modulus when the characteristics of fiber-epoxy interface in the nanocomposites are modified. The results indicate that well above  $T_g$ , incorporation of single molecules of bonded P(St-co-GMA) and nonbonded P(St-co-GMA) lead to a small but distinguishable increase in Young's modulus over neat epoxy system. Glass transition temperatures of composite systems are also studied. Results corroborating the experiments suggest that the manipulation in glass transition temperature at the interface may be designed by modifying the chemistry of the constituents. The second part of *Chapter 5* pursues a novel multi-scale numerical simulation method for nanocomposites. First, well-parameterized coarse-graining is employed to study of thermoset matrices on longer length scales. Next a reverse-mapping process to project atomistic structure back onto the coarse-grained system is carried out. Consecutive numerical simulations at different length-scales allow predicting long-term behavior of polymer matrices where direct MD simulations are not time-effective to study.

We demonstrated the reliability and applicability of proposed multi-scale analysis on polymer matrices. The next step of this research will focus on cross-linking procedure of thermoset matrices and analyzing the mechanical properties of reinforced nanocomposites. In addition, the proposed multi-scale method will be extended to study the mechanical, thermal or thermo-mechanical properties of any soft matter system. Designing molecular interactions and cross-linking at the interface via computationally cost effective, multi-scale models offers useful insight to applicability at the macro scale.

## APPENDICES

### APPENDIX A: Screenshots of Abstract of Publications related to Thesis

LETTER

# Engineering Chemistry of Electrospun Nanofibers and Interfaces in Nanocomposites for Superior Mechanical Properties

Elif Özden, Yusuf Z. Mencilođlu, and Melih Papila\*

Sabancı University, Materials Science and Engineering, Advanced Composites and Polymer Processing Laboratory, 34956 Tuzla, Istanbul, Turkey

**ABSTRACT** The novelty of this work is based on designing the chemistry of the electrospun nanofibers, so that the resultant composites substantially benefit from cross-linking between the nanofibers and the polymer matrix. Specifically, the solution of in-house synthesized copolymers polystyrene-co-glycidyl methacrylate P(St-co-GMA) is electrospun to produce mats of surface reactive nano-to-submicron scale fibers that are accompanied later by spraying over the ethylenediamine (EDA) as a supplementary cross-linking agent for epoxy. The P(St-co-GMA)/EDA fiber mats are then embedded into an epoxy resin. Analysis of the three-point-bending mode of the composites reveals that the storage modulus of P(St-co-GMA)/EDA nanofiber-reinforced epoxy are about 10 and 2.5 times higher than that of neat and P(St-co-GMA) nanofiber-reinforced epoxy, respectively, even though the weight fraction of the nanofibers was as low as 2 wt %. The significant increase in the mechanical response is attributed to the inherently cross-linked fiber structure and the surface modification/chemistry of the electrospun fibers, that results in cross-linked polymer matrix–nanofiber interfacial bonding.


**KEYWORDS:** electrospinning • nanofiber • composite • surface modification • cross-linked interface

I.

# MWCNTs/P(St-co-GMA) Composite Nanofibers of Engineered Interface Chemistry for Epoxy Matrix Nanocomposites

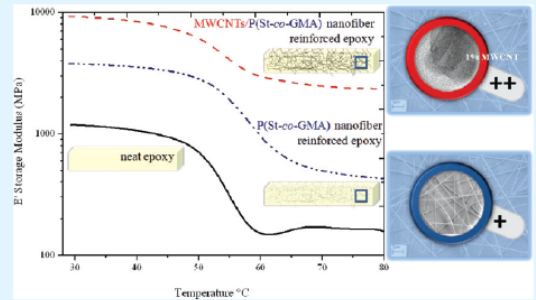
Elif Özden-Yenigün, Yusuf Z. Menceloğlu,\* and Melih Papila<sup>‡</sup>

Sabancı University, Materials Science and Engineering, Advanced Composites and Polymer Processing Laboratory, 349S6 Tuzla, Istanbul, Turkey

 Supporting Information

**ABSTRACT:** Strengthened nanofiber-reinforced epoxy matrix composites are demonstrated by engineering composite electrospun fibers of multi-walled carbon nanotubes (MWCNTs) and reactive P(St-co-GMA). MWCNTs are incorporated into surface-modified, reactive P(St-co-GMA) nanofibers by electrospinning; functionalization of these MWCNT/P(St-co-GMA) composite nanofibers with epoxide moieties facilitates bonding at the interface of the cross-linked fibers and the epoxy matrix, effectively reinforcing and toughening the epoxy resin. Rheological properties are determined and thermodynamic stabilization is demonstrated for MWCNTs in the P(St-co-GMA)-DMF polymer solution. Homogeneity and uniformity of the fiber formation within the electrospun mats are achieved at polymer concentration of 30 wt %. Results show that the MWCNT fraction decreases the polymer solution viscosity, yielding a narrower fiber diameter. The fiber diameter drops from an average of 630 nm to 460 nm, as the MWCNTs wt fraction (1, 1.5, and 2%) is increased. The electrospun nanofibers of the MWCNTs/P(St-co-GMA) composite are also embedded into an epoxy resin to investigate their reinforcing abilities. A significant increase in the mechanical response is observed, up to >20% in flexural modulus, when compared to neat epoxy, despite a very low composite fiber weight fraction (at about 0.2% by a single-layer fibrous mat). The increase is attributed to the combined effect of the two factors the inherent strength of the well-dispersed MWCNTs and the surface chemistry of the electrospun fibers that have been modified with epoxide to enable cross-linking between the polymer matrix and the nanofibers.

**KEYWORDS:** electrospinning, composite nanofibers, surface modification, cross-linked interface, carbon nanotubes



## II.

### Structural composites hybridized with epoxy compatible polymer/MWCNT nanofibrous interlayers

K. Bilge, E. Ozden-Yenigun, E. Simsek, Y.Z. Menceloglu, M. Papila\*,<sup>1</sup>

Faculty of Engineering and Natural Sciences, Advanced Composites and Polymer Processing Laboratory (AC2PL), Sabanci University, Istanbul, Turkey

#### ARTICLE INFO

**Article history:**  
Received 14 April 2012  
Accepted 8 July 2012  
Available online 15 July 2012

**Keywords:**  
A. Nanocomposites  
A. Structural composites  
E. Electro-spinning  
B. Delamination  
Interlayer

#### ABSTRACT

Surface reactive P(St-co-GMA) copolymer and P(St-co-GMA)/MWCNT fibrous mats are placed onto a conventional carbon fiber/epoxy prepreg as interlayer reinforcing material. Experimental observations are used to demonstrate excellent epoxy wetting and structural compatibility of the interlayers chemically tuned for the epoxy matrix. Comparisons of increase in mechanical performance by incorporating P(St-co-GMA) and P(St-co-GMA)/MWCNT interlayers also show the contribution of MWCNT presence in the copolymer nanofibers. Flexural strength and stiffness of (0/0/0) and (90/0/90) laminates increase up to 17% when the nanocomposite interlayers are integrated. Cross-sectional SEM analyses of the failure surfaces suggest reinforcing ability of interlayers both against transverse cracking and delamination. Further examination for the delamination resistance is presented by the End Notched Flexure (ENF) tests. An improvement up to 70% in mode II strain energy release rate ( $G_{IIc}$ ) is recorded for the laminates with nanocomposite interlayers. The resistance against transverse matrix cracking in the presence of interlayers is also elaborated. Charpy-impact and transverse-tension tests result in up to 20% and 27% increase in the impact energy absorbance and transverse tensile strength, respectively. Overall, the test results suggest that mechanical behavior of the laminates is enhanced by the nanofibrous interlayers chemically-tuned for epoxy crosslinking, with no weight penalty.

© 2012 Elsevier Ltd. All rights reserved.

## III.

## Designed-in Molecular Interactions Lead to Superior Thermo-mechanical Properties in Nanocomposites

E. Ozden, A.R. Atilgan, K. Bilge, Y.Z. Menceloglu, C. Atilgan and M. Papila

Faculty of Engineering and Natural Sciences, Sabanci University, Istanbul 34956, Turkey

### ABSTRACT

The effect of the nanofiller chemistry on the mechanical behaviour of thermoset polymer matrix nanocomposites is investigated. The interaction between a crosslinked polymer resin and the reinforcing nanofibers driven by their chemistry is revealed by molecular dynamics simulations. Specifically, crosslinked network systems of neat epoxy and epoxy-P(St-co-GMA) are modeled to discuss the effect of various molecular interactions as a function of temperature on a molecular basis. At 433K°, incorporation of single molecule of bonded P(St-co-GMA) and nonbonded P(St-co-GMA) lead to increase in Young's modulus by 10% and 6%, respectively, compared to neat epoxy system.

IV.

ECCM15 - 15<sup>TH</sup> EUROPEAN CONFERENCE ON COMPOSITE MATERIALS, Venice, Italy, 24-28 June 2012

## TRACING THE SUPERIOR THERMO-MECHANICAL PROPERTIES IN NANOCOMPOSITES OF CROSSLINKED FILLERS AND INTERFACES: MOLECULAR POINT OF VIEW

E. Özden-Yenigün<sup>1\*</sup>, C. Atilgan<sup>1</sup>, Y. Z. Menceloğlu<sup>1</sup>, M. Papila<sup>1,2</sup>

<sup>1</sup> Faculty of Engineering and Natural Sciences, Material Science and Engineering, Sabanci University, Tuzla-Istanbul 34956

<sup>2</sup> currently in Department of Aeronautics&Astronautics, Stanford University, Stanford CA, USA

\*elifozden@sabanciuniv.edu

**Keywords:** nanocomposites, molecular dynamics, crosslinked interface, surface modification

### Abstract

*This study presents an investigation by molecular dynamics (MD) simulations, specifically focus on epoxy matrix nanocomposite mechanical behavior. Reinforcing materials of interest are surface reactive P(St-co-GMA) nanofibers. Effect of the nanofiller chemistry on mechanical behavior of thermoset polymer matrix nanocomposites is explored. Molecular dynamics simulations are employed to address the differences in the temperature dependence of the bulk, shear and Young's modulus when the characteristics of fiber-epoxy interface in the nanocomposites are modified. The results indicated that at 493K°, incorporation of single molecule of bonded P(St-co-GMA) and nonbonded P(St-co-GMA) lead to increase in Young's modulus by 9% and 6%, respectively, compared to neat epoxy system. Glass transition temperatures of composite systems are also studied. Results corroborating the experiments suggest that the manipulation in glass transition temperature at the interface may be designed by modifying the chemistry of the constituents.*

V.

**Electrospun Polymer/MWCNTs Nanofiber Reinforced Composites**  
**“Improvement of Interfacial Bonding by Surface Modified Nanofibers”**

Journal:	2009 MRS Fall Meeting
Manuscript ID:	1224-FF10-23.R1
Symposium:	Symposium FF
Date Submitted by the Author:	
Complete List of Authors:	Ozden, Elif; Sabanci University, Material Science and Engineering Menceloglu, Yusuf; Sabanci University, Material Science and Engineering Papila, Melih; Sabanci University, Material Science and Engineering
Keywords:	fiber, nanostructure, polymer

**Electrospun Polymer/MWCNTs Nanofiber Reinforced Composites**  
**“Improvement of Interfacial Bonding by Surface Modified Nanofibers”**

Elif Ozden, Yusuf Menceloglu, Melih Papila  
Sabanci University, Material Science and Engineering, 34956, Tuzla, Istanbul, Turkey

**ABSTRACT**

In-house synthesized copolymers Polystyrene-co-glycidyl methacrylate (PSt-co-GMA) are electrospun as mat of surface modified nanofibers with and without multi walled carbon nanotubes (MWCNTs). Composites are then formed by embedding layers of the nanofiber mats into epoxy resin. Interfacial bonding between polymer matrix and the nanofibers, and surface modification driven enhancement in mechanical response is assessed under flexural loads. Results indicate that at elevated temperature storage modulus of epoxy reinforced by PSt-co-GMA nanofibers and PSt-co-GMA/ MWCNTs composite nanofibers is about 10 and 20 times higher than the neat epoxy, respectively, despite weight fraction of the nanofibers being as low as 2 wt%. Interfacial interaction is revealed by the storage modulus comparison of unmodified Polystyrene (PSt) and modified PSt-co-GMA nanofiber reinforced composite. To enhance further the resulting “crosslinked” structure, crosslinking agent ethylenediamine is also sprayed on the nanofibrous mats. Increased crosslinking density improves mechanical response of sprayed-over PSt-co-GMA nanofibers reinforced composites which is about 4 times higher than plain PSt-co-GMA nanofibers.

**VI.**

**STRENGTH OF LAMINATES WITH SURFACE MODIFIED  
POLYMER/MWCNTS NANO-COMPOSITE INTERLAYERS**

K.Bilge<sup>1</sup>, E.Ozden<sup>1</sup>, Y.Z.Menceloglu<sup>1</sup>, M.Papila<sup>1\*</sup>

<sup>1</sup> Faculty of Engineering and Natural Sciences, Advanced Composites and Polymer Processing  
Laboratory(AC2PL), Sabanci University , Istanbul, Turkey

\* Corresponding author (mpapila@sabanciuniv.edu)

**VII.**

**Keywords:** *laminated composites, electrospun nanofiber, interlayer, delamination resistance*



## REFERENCES

- [1] Schandler L. S., Brinson L. C., Sawyer W. G. Polymer nanocomposites: A small part of the story. *Jom*. 2007;59(3):53-60.
- [2] Ozden E., Menceloglu Y. Z., Papila M. Engineering chemistry of electrospun nanofibers and interfaces in nanocomposites for superior mechanical properties. *ACS Applied Materials & Interfaces*. 2010;2(7):1788-1793.
- [3] Ozden-Yenigun E., Menceloğlu Y. Z., Papila M. MWCNTs/P(St-co-GMA) composite nanofibers of engineered interface chemistry for epoxy matrix nanocomposites. *ACS Applied Materials & Interfaces*. 2012;4(2):777-784.
- [4] Bilge K., Ozden-Yenigun E., Simsek E., Menceloglu Y. Z., Papila M. Structural composites hybridized with epoxy compatible polymer/MWCNT nanofibrous interlayers. *Composites Science and Technology*. 2012;72(14):1639-1645.
- [5] Özden Yenigün E., Atılğan A. R., Bilge K., Menceloğlu Y. Z., Atılğan C., Papila M. Designed-in molecular interactions lead to superior thermo-mechanical properties in nanocomposites. *Mater. Res. Soc. Symp. Proc. Vol. 1304*, Boston, USA (2011).
- [6] Özden Yenigün E., Atılğan C., Menceloğlu Y. Z., Papila M. Tracing the superior thermo-mechanical properties in nanocomposites of crosslinked fillers at the interface: Molecular point of view. European Society of Composite Materials (ECCM15) Proceedings 2012.
- [7] Beecroft L. L., Ober C. K. Nanocomposite materials for optical applications. *Chemistry of Materials*, vol. 91997. p. 1302-1317.
- [8] Dzenis Y. Materials science - structural nanocomposites. *Science*. 2008;319(5862):419-420.
- [9] Gangopadhyay R., De A. Conducting polymer nanocomposites: A brief overview. *Chemistry of Materials*. 2000;12(3):608-622.
- [10] Hussain F., Hojjati M., Okamoto M., Gorga R. E. Review article: Polymer-matrix nanocomposites, processing, manufacturing, and application: An overview. *Journal of Composite Materials*. 2006;40(17):1511-1575.
- [11] Krishnamoorti R., Vaia R. A. Polymer nanocomposites. *Journal of Polymer Science Part B-Polymer Physics*. 2007;45(24):3252-3256.
- [12] Okada A., Usuki A. Twenty years of polymer-clay nanocomposites. *Macromolecular Materials and Engineering*. 2006;291(12):1449-1476.
- [13] Schmidt G., Malwitz M. M. Properties of polymer-nanoparticle composites. *Current Opinion in Colloid & Interface Science*. 2003;8(1):103-108.
- [14] Bergshoef M. M., Vancso G. J. Transparent nanocomposites with ultrathin, electrospun nylon-4,6 fiber reinforcement. *Advanced Materials*. 1999;11(16):1362-1365.
- [15] Chen G. F. S., Liu H. Q. Electrospun cellulose nanofiber reinforced soybean protein isolate composite film. *Journal of Applied Polymer Science*. 2008;110(2):641-646.
- [16] Chronakis I. S. Novel nanocomposites and nanoceramics based on polymer nanofibers using electrospinning process - A Review. *Journal of Materials Processing Technology*. 2005;167(2-3):283-293.
- [17] Dodiuk-Kenig H., Lizenboim K., Roth S., Zalsman B., Mchale W. A., Jaffe M., et al. Performance enhancement of dental composites using electrospun nanofibers. *Journal of Nanomaterials*. 2008.

- [18] Fang J., Lin T., Tian W., Sharma A., Wang X. G. Toughened electrospun nanofibers from crosslinked elastomer-thermoplastic blends. *Journal of Applied Polymer Science*. 2007;105(4):2321-2326.
- [19] Fong H. Electrospun nylon 6 nanofiber reinforced bis-GMA/TEGDMA dental restorative composite resins. *Polymer*. 2004;45(7):2427-2432.
- [20] Gao Y., Sagi S., Zhang L. F., Liao Y. L., Cowles D. M., Sun Y. Y., et al. Electrospun nano-scaled glass fiber reinforcement of bis-GMA/TEGDMA dental composites. *Journal of Applied Polymer Science*. 2008;110(4):2063-2070.
- [21] Han S. O., Son W. K., Youk J. H., Park W. H. Electrospinning of ultrafine cellulose fibers and fabrication of poly(butylene succinate) biocomposites reinforced by them. *Journal of Applied Polymer Science*. 2008;107(3):1954-1959.
- [22] Kim J. S., Reneker D. H. Mechanical properties of composites using ultrafine electrospun fibers. *Polymer Composites*. 1999;20(1):124-131.
- [23] Lin S., Cai Q., Ji J. Y., Sui G., Yu Y. H., Yang X. P., et al. Electrospun nanofiber reinforced and toughened composites through in situ nano-interface formation. *Composites Science and Technology*. 2008;68(15-16):3322-3329.
- [24] Rasheed A., Dadmun M. D., Britz P. F. Polymer-nanofiber composites: Enhancing composite properties by nanofiber oxidation. *Journal of Polymer Science Part B-Polymer Physics*. 2006;44(21):3053-3061.
- [25] Romo-Urbe A., Arizmendi L., Romero-Guzman M. E., Sepulveda-Guzman S., Cruz-Silva R. Electrospun nylon nanofibers as effective reinforcement to polyaniline membranes. *ACS Applied Materials & Interfaces*. 2009;1(11):2502-2508.
- [26] Dagdeviren C., Papila M. Dielectric behavior characterization of a fibrous-zno/pvdf nanocomposite. *Polymer Composites*. 2010;31(6):1003-1010.
- [27] Greiner A., Wendorff J. H. Electrospinning: A fascinating method for the preparation of ultrathin fibres. *Angewandte Chemie-International Edition*. 2007;46(30):5670-5703.
- [28] Salehi-Khojin A., Stone J. J., Zhong W. H. Improvement of interfacial adhesion between uhmwpe fiber and epoxy matrix using functionalized graphitic nanofibers. *Journal of Composite Materials*. 2007;41(10):1163-1176.
- [29] Zhu J., Peng H. Q., Rodriguez-Macias F., Margrave J. L., Khabashesku V. N., Imam A. M., et al. Reinforcing epoxy polymer composites through covalent integration of functionalized nanotubes. *Advanced Functional Materials*. 2004;14(7):643-648.
- [30] Suhr J., Koratkar N. A., Ye D. X., Lu T. M. Damping properties of epoxy films with nanoscale fillers. *Journal of Intelligent Material Systems and Structures*. 2006;17(3):255-260.
- [31] Jiang L. Y. Macroscopic behavior of carbon nanotube (CNT)-reinforced composite accounting for interface cohesive force. *Journal of Adhesion*. 2010;86(3):273-289.
- [32] Demir M. M., Menceloglu Y. Z., Erman B. Effect of filler amount on thermoelastic properties of poly (dimethylsiloxane) networks. *Polymer*. 2005;46(12):4127-4134.
- [33] Chandra R., Singh S. P., Gupta K. Damping studies in fiber-reinforced composites - A Review. *Composite Structures*. 1999;46(1):41-51.
- [34] Rajoria H., Jalili N. Passive vibration damping enhancement using carbon nanotube-epoxy reinforced composites. *Composites Science and Technology*. 2005;65(14):2079-2093.
- [35] Ratna D., Chakraborty B. C., Dutta H., Banthia A. K. Nanoreinforcement of flexible epoxy using layered silicate. *Polymer Engineering and Science*. 2006;46(12):1667-1673.
- [36] Zhou X., Shin E., Wang K. W., Bakis C. E. Interfacial damping characteristics of carbon nanotube-based composites. *Composites Science and Technology*. 2004;64(15):2425-2437.

- [37] Chen L., Gong X. L., Li W. H. Effect of carbon black on the mechanical performances of magnetorheological elastomers. *Polymer Testing*. 2008;27(3):340-345.
- [38] Rittigstein P., Torkelson J. M. Polymer-nanoparticle interfacial interactions in polymer nanocomposites: Confinement effects on glass transition temperature and suppression of physical aging. *Journal of Polymer Science Part B-Polymer Physics*. 2006;44(20):2935-2943.
- [39] Ellison C. J., Torkelson J. M. The distribution of glass-transition temperatures in nanoscopically confined glass formers. *Nature Materials*. 2003;2(10):695-700.
- [40] Frank C. W., Rao V., Despotopoulou M. M., Pease R. F. W., Hinsberg W. D., Miller R. D., et al. Structure in thin and ultrathin spin-cast polymer films. *Science*. 1996;273(5277):912-915.
- [41] Priestley R. D., Ellison C. J., Broadbelt L. J., Torkelson J. M. Structural relaxation of polymer glasses at surfaces, interfaces and in between. *Science*. 2005;309(5733):456-459.
- [42] Gawandi A. A., Whitney J. M., Tandon G. P., Brockman R. B. Three-dimensional analysis of the interaction between a matrix crack and nanofiber. *Composites Part B-Engineering*. 2009;40(8):698-704.
- [43] Hsieh T. H., Kinloch A. J., Masania K., Taylor A. C., Sprenger S. The mechanisms and mechanics of the toughening of epoxy polymers modified with silica nanoparticles. *Polymer*. 2010;51(26):6284-6294.
- [44] Crosby A. J., Lee J. Y. Polymer nanocomposites: The "nano" effect on mechanical properties. *Polymer Reviews*. 2007;47(2):217-229.
- [45] Lawn B. R. *Fracture of brittle solids*. London: Cambridge University Press; 1993.
- [46] Marshall D. B., Cox B. N., Evans A. G. The mechanics of matrix cracking in brittle-matrix fiber composites. *Acta Metallurgica*. 1985;33(11):2013-2021.
- [47] Iijima S. Helical microtubules of graphitic carbon. *Nature*. 1991;354(6348):56-58.
- [48] Ago H., Petritsch K., Shaffer M. S. P., Windle A. H., Friend R. H. Composites of carbon nanotubes and conjugated polymers for photovoltaic devices. *Advanced Materials*. 1999;11(15):1281.
- [49] Alexandrou I., Kymakis E., Amaratunga G. a. J. Polymer-nanotube composites: Burying nanotubes improves their field emission properties. *Applied Physics Letters*. 2002;80(8):1435-1437.
- [50] Hughes M., Shaffer M. S. P., Renouf A. C., Singh C., Chen G. Z., Fray J., et al. Electrochemical capacitance of nanocomposite films formed by coating aligned arrays of carbon nanotubes with polypyrrole. *Advanced Materials*. 2002;14(5):382-385.
- [51] Kymakis E., Amaratunga G. a. J. Single-wall carbon nanotube/conjugated polymer photovoltaic devices. *Applied Physics Letters*. 2002;80(1):112-114.
- [52] Moniruzzaman M., Winey K. I. Polymer nanocomposites containing carbon nanotubes. *Macromolecules*. 2006;39(16):5194-5205.
- [53] Anderson M. R., Mattes B. R., Reiss H., Kaner R. B. Conjugated polymer-films for gas separations. *Science*. 1991;252(5011):1412-1415.
- [54] Dror Y., Salalha W., Khalfin R. L., Cohen Y., Yarin A. L., Zussman E. Carbon nanotubes embedded in oriented polymer nanofibers by electrospinning. *Langmuir*. 2003;19(17):7012-7020.
- [55] Ko F., Gogotsi Y., Ali A., Naguib N., Ye H. H., Yang G. L., et al. Electrospinning of continuous carbon nanotube-filled nanofiber yarns. *Advanced Materials*. 2003;15(14):1161-+.
- [56] Ye H. H., Lam H., Titchenal N., Gogotsi Y., Ko F. Reinforcement and rupture behavior of carbon nanotubes-polymer nanofibers. *Applied Physics Letters*. 2004;85(10):1775-1777.

- [57] Ge J. J., Hou H. Q., Li Q., Graham M. J., Greiner A., Reneker D. H., et al. Assembly of well-aligned multiwalled carbon nanotubes in confined polyacrylonitrile environments: Electrospun composite nanofiber sheets. *Journal of the American Chemical Society*. 2004;126(48):15754-15761.
- [58] Jose M. V., Steinert B. W., Thomas V., Dean D. R., Abdalla M. A., Price G., et al. Morphology and mechanical properties of Nylon 6/MWNT nanofibers. *Polymer*. 2007;48(4):1096-1104.
- [59] Sen R., Zhao B., Perea D., Itkis M. E., Hu H., Love J., et al. Preparation of single-walled carbon nanotube reinforced polystyrene and polyurethane nanofibers and membranes by electrospinning. *Nano Letters*. 2004;4(3):459-464.
- [60] Reneker D. H., Chun I. Nanometre diameter fibres of polymer, produced by electrospinning. *Nanotechnology*. 1996;7(3):216-223.
- [61] Yordem O. S., Papila M., Menciloglu Y. Z. Effects of electrospinning parameters on polyacrylonitrile nanofiber diameter: An investigation by response surface methodology. *Materials & Design*. 2008;29(1):34-44.
- [62] Hunter C. A., Sanders J. K. M. The nature of pi-pi interactions. *Journal of the American Chemical Society*. 1990;112(14):5525-5534.
- [63] Zhao J. J., Lu J. P., Han J., Yang C. K. Noncovalent functionalization of carbon nanotubes by aromatic organic molecules. *Applied Physics Letters*. 2003;82(21):3746-3748.
- [64] Bahr J. L., Mickelson E. T., Bronikowski M. J., Smalley R. E., Tour J. M. Dissolution of small diameter single-wall carbon nanotubes in organic solvents? *Chemical Communications*. 2001(2):193-194.
- [65] Sun Y., Wilson S. R., Schuster D. I. High dissolution and strong light emission of carbon nanotubes in aromatic amine solvents. *Journal of the American Chemical Society*. 2001;123(22):5348-5349.
- [66] Chen J., Liu H. Y., Weimer W. A., Halls M. D., Waldeck D. H., Walker G. C. Noncovalent engineering of carbon nanotube surfaces by rigid, functional conjugated polymers. *Journal of the American Chemical Society*. 2002;124(31):9034-9035.
- [67] Mitchell C. A., Bahr J. L., Arepalli S., Tour J. M., Krishnamoorti R. Dispersion of functionalized carbon nanotubes in polystyrene. *Macromolecules*. 2002;35(23):8825-8830.
- [68] O'Connell M. J., Boul P., Ericson L. M., Huffman C., Wang Y. H., Haroz E., et al. Reversible water-solubilization of single-walled carbon nanotubes by polymer wrapping. *Chemical Physics Letters*. 2001;342(3-4):265-271.
- [69] Star A., Liu Y., Grant K., Ridvan L., Stoddart J. F., Steuerman D. W., et al. Noncovalent side-wall functionalization of single-walled carbon nanotubes. *Macromolecules*. 2003;36(3):553-560.
- [70] Star A., Stoddart J. F., Steuerman D., Diehl M., Boukai A., Wong E. W., et al. Preparation and properties of polymer-wrapped single-walled carbon nanotubes. *Angewandte Chemie-International Edition*. 2001;40(9):1721-1725.
- [71] Islam M. F., Rojas E., Bergey D. M., Johnson A. T., Yodh A. G. High weight fraction surfactant solubilization of single-wall carbon nanotubes in water. *Nano Letters*. 2003;3(2):269-273.
- [72] Park S. J., Cho M. S., Lim S. T., Choi H. J., Jhon M. S. Electrorheology of multiwalled carbon nanotube/poly(methyl methacrylate) nanocomposites. *Macromolecular Rapid Communications*. 2005;26(19):1563-1566.
- [73] Mazinani S., Aji A., Dubois C. Morphology, structure and properties of conductive P<sub>s</sub>/CNT nanocomposite electrospun mat. *Polymer*. 2009;50(14):3329-3342.

- [74] Ozden E., Menciloglu Y., Papila M. Electrospun polymer/MWCNTs nanofiber reinforced composites “Improvement of interfacial bonding by surface modified nanofibers”. *MRS Proceedings*. 2009;1224(1).
- [75] Antunes E. F., Lobo A. O., Corat E. J., Trava-Airoldi V. J., Martin A. A., Verissimo C. Comparative study of first- and second-order raman spectra of mwcnt at visible and infrared laser excitation. *Carbon*. 2006;44(11):2202-2211.
- [76] Corrias M., Serp P., Kalck P., Dechambre G., Lacout J. L., Castiglioni C., et al. High purity multiwalled carbon nanotubes under high pressure and high temperature. *Carbon*. 2003;41(12):2361-2367.
- [77] Duraia E. S. M., Burkitbaev M., Mohamedbahr H., Mansurov Z., Tokmolden S., Beall G. W. Growth of carbon nanotubes on diatomite. *Vacuum*. 2009;84(4):464-468.
- [78] Wenzel R. N. 1936;- 28(- 8):- 994.
- [79] Cassie A. B. D., Baxter S. Wettability of porous surfaces. *Transactions of the Faraday Society*. 1944;40(0):546-551.
- [80] Tsotsis T. K. Interlayer toughening of composite materials. *Polymer Composites*. 2009;30(1):70-86.
- [81] Lee S. H., Lee J. H., Cheong S. K., Noguchi H. A toughening and strengthening technique of hybrid composites with non-woven tissue. *Journal of Materials Processing Technology*. 2008;207(1-3):21-29.
- [82] Lee S. H., Noguchi H., Kim Y. B., Cheong S. K. Effect of interleaved non-woven carbon tissue on interlaminar fracture toughness of laminated composites: Part 1 - mode II. *Journal of Composite Materials*. 2002;36(18):2153-2168.
- [83] Liu L., Huang Z. M., He C. L., Han X. J. Mechanical performance of laminated composites incorporated with nanofibrous membranes. *Materials Science and Engineering A-Structural Materials Properties Microstructure and Processing*. 2006;435:309-317.
- [84] Liu L., Huang Z. M., Xu G. Y., Liang Y. M., Dong G. H. Mode ii interlaminar delamination of composite laminates incorporating with polymer ultrathin fibers. *Polymer Composites*. 2008;29(3):285-292.
- [85] Sihm S., Kim R. Y., Huh W., Lee K. H., Roy A. K. Improvement of damage resistance in laminated composites with electrospun nano-interlayers. *Composites Science and Technology*. 2008;68(3-4):673-683.
- [86] Zucchelli A., Focarete M. L., Gualandi C., Ramakrishna S. Electrospun nanofibers for enhancing structural performance of composite materials. *Polymers for Advanced Technologies*. 2011;22(3):339-349.
- [87] Bilge K. Multi-scale nature of composite materials: Three case studies Master of Science Thesis, Sabanci University, 2012.
- [88] Albertsen H., Ivens J., Peters P., Wevers M., Verpoest I. Interlaminar fracture-toughness of CFRP influenced by fiber surface-treatment: 1. Experimental results. *Composites Science and Technology*. 1995;54(2):133-145.
- [89] Seyhan A. T., Tanoglu M., Schulte K. Mode I and mode II fracture toughness of e-glass non-crimp fabric/carbon nanotube (CNT) modified polymer based composites. *Engineering Fracture Mechanics*. 2008;75(18):5151-5162.
- [90] Stevanovic D., Kalyanasundaram S., Lowe A., Jar P. Y. B. Mode i and mode ii delamination properties of glass/vinyl-ester composite toughened by particulate modified interlayers. *Composites Science and Technology*. 2003;63(13):1949-1964.
- [91] Stevens M. J. Manipulating connectivity to control fracture in network polymer adhesives. *Macromolecules*. 2001;34(5):1411-1415.

- [92] Wu C. F., Xu W. J. Atomistic molecular modelling of crosslinked epoxy resin. *Polymer*. 2006;47(16):6004-6009.
- [93] Yu S., Yang S., Cho M. Multi-scale modeling of cross-linked epoxy nanocomposites. *Polymer*. 2009;50(3):945-952.
- [94] Zhu R., Pan E., Roy A. K. Molecular dynamics study of the stress-strain behavior of carbon-nanotube reinforced EPON 862 composites. *Materials Science and Engineering A-Structural Materials Properties Microstructure and Processing*. 2007;447(1-2):51-57.
- [95] Material-Studio. Accelrys inc. San Diego 2002.
- [96] Sun H. COMPASS: An ab initio force-field optimized for condensed-phase applications - overview with details on alkane and benzene compounds. *Journal of Physical Chemistry B*. 1998;102(38):7338-7364.
- [97] Sun L., Warren G. L., O'reilly J. Y., Everett W. N., Lee S. M., Davis D., et al. Mechanical properties of surface-functionalized SWCNT/epoxy composites. *Carbon*. 2008;46(2):320-328.
- [98] Andersen H. C. Molecular-dynamics simulations at constant pressure and-or temperature. *Journal of Chemical Physics*. 1980;72(4):2384-2393.
- [99] Berendsen H. J. C., Postma J. P. M., Vangunsteren W. F., Dinola A., Haak J. R. Molecular-dynamics with coupling to an external bath. *Journal of Chemical Physics*. 1984;81(8):3684-3690.
- [100] Hildebrand J. H. *The solubility of non-electrolytes*. New York: Reinhold; 1936.
- [101] ACD/Chemsketch. Advanced chemistry development inc. Toronto, ON, Canada 2003.
- [102] Groot R. D., Warren P. B. Dissipative particle dynamics: Bridging the gap between atomistic and mesoscopic simulation. *Journal of Chemical Physics*. 1997;107(11):4423-4435.
- [103] Travis K. P., Bankhead M., Good K., Owens S. L. New parametrization method for dissipative particle dynamics. *Journal of Chemical Physics*. 2007;127(1).
- [104] Doruker P., Mattice W. L. Reverse mapping of coarse-grained polyethylene chains from the second nearest neighbor diamond lattice to an atomistic model in continuous space. *Macromolecules*. 1997;30(18):5520-5526.
- [105] Ghanbari A., Boehm M. C., Mueller-Plathe F. A simple reverse mapping procedure for coarse-grained polymer models with rigid side groups. *Macromolecules*. 2011;44(13):5520-5526.
- [106] Harmandaris V. A., Adhikari N. P., Van Der Vegt N. F. A., Kremer K. Hierarchical modeling of polystyrene: From atomistic to coarse-grained simulations. *Macromolecules*. 2006;39(19):6708-6719.
- [107] Kacar G., Atilgan C., Ozen A. S. Mapping and reverse-mapping of the morphologies for a molecular understanding of the self-assembly of fluorinated block copolymers. *Journal of Physical Chemistry C*. 2010;114(1):370-382.
- [108] Peter C., Delle Site L., Kremer K. Classical simulations from the atomistic to the mesoscale and back: Coarse graining an azobenzene liquid crystal. *Soft Matter*. 2008;4(4):859-869.
- [109] Rzepiela A. J., Schafer L. V., Goga N., Risselada H. J., De Vries A. H., Marrink S. J. Software news and update reconstruction of atomistic details from coarse-grained structures. *Journal of Computational Chemistry*. 2010;31(6):1333-1343.
- [110] Santangelo G., Di Matteo A., Muller-Plathe F., Milano G. From mesoscale back to atomistic models: A fast reverse-mapping procedure for vinyl polymer chains. *Journal of Physical Chemistry B*. 2007;111(11):2765-2773.

[111] Spyriouni T., Tzoumanekas C., Theodorou D., Muller-Plathe F., Milano G. Coarse-grained and reverse-mapped united-atom simulations of long-chain atactic polystyrene melts: Structure, thermodynamic properties, chain conformation, and entanglements. *Macromolecules*. 2007;40(10):3876-3885.

[112] Fan H. B., Yuen M. M. F. Material properties of the cross-linked epoxy resin compound predicted by molecular dynamics simulation. *Polymer*. 2007;48(7):2174-2178.

## LIST OF PUBLICATIONS

- A. Ozden E.**, Menciloglu Y. Z., Papila M. Engineering chemistry of electrospun nanofibers and interfaces in nanocomposites for superior mechanical properties. *ACS Applied Materials & Interfaces*. 2010;2(7):1788-1793.
- B. Ozden-Yenigun E.**, Menciloglu Y. Z., Papila M. MWCNTs/P (St-co-GMA) composite nanofibers of engineered interface chemistry for epoxy matrix nanocomposites. *ACS Applied Materials & Interfaces*. 2012;4(2):777-784.
- C. Bilge K., Ozden-Yenigun E.**, Simsek E., Menciloglu Y. Z., Papila M. Structural composites hybridized with epoxy compatible polymer/MWCNT nanofibrous interlayers. *Composites Science and Technology*. 2012;72(14):1639-1645.
- D. Ozden-Yenigun E.**, Simsek E., Menciloglu Y. Z., Atilgan C. Molecular Basis for Solvent Dependent Morphologies Observed in Electro-Sprayed Surfaces Under review *Journal of Physical Chemistry B*, March 2013.
- E. Ozden-Yenigun E.**, Atilgan A. R., Bilge K., Menciloglu Y. Z., Atilgan C., Papila M. Designed-in Molecular Interactions Lead to Superior Thermo-mechanical Properties in Nanocomposites in *Mater. Res. Soc. Symp. Proc. Vol. 1304*, Boston, USA (2011) DOI: 10.1557/opl.2011.607.
- F. Ozden-Yenigun E.**, Atilgan C., Menciloglu Y. Z., Papila M. Tracing the superior thermo-mechanical properties in nanocomposites of crosslinked fillers at the interface: Molecular point of view. European Society of Composite Materials (ECCM15) Proceedings 2012.
- G. Bilge K., Ozden-Yenigun E.**, Simsek E., Menciloglu Y. Z., Papila M. Strength of hybrid composites reinforced with surface modified polymer/MWCNTs nanocomposite interlayers International Conference on Composite Materials (ICCM18) Proceedings 2011.
- H. Ozden E.**, Menciloglu Y.Z., Papila M., Proceeding in *Mechanical Behavior at Small Scales — Experiments and Modeling*, edited by Lou J.; Lilleodden E.; Boyce B.; Lu L.; Derlet P.M.; Weygand D.; Li J.; Uchic M.D.; Le Bourhis E.; (Mater. Res. Soc. Symp. Proc. 1224, Warrendale, PA.), 1224-FF10-23 (2010).